

12-2017

On the Fatigue of Headed Shear Studs in Steel-Concrete Composite Bridge Girders

Brianna Laurene Ovuoba
University of Arkansas, Fayetteville

Follow this and additional works at: <http://scholarworks.uark.edu/etd>

 Part of the [Civil Engineering Commons](#), and the [Transportation Engineering Commons](#)

Recommended Citation

Ovuoba, Brianna Laurene, "On the Fatigue of Headed Shear Studs in Steel-Concrete Composite Bridge Girders" (2017). *Theses and Dissertations*. 2545.
<http://scholarworks.uark.edu/etd/2545>

This Dissertation is brought to you for free and open access by ScholarWorks@UARK. It has been accepted for inclusion in Theses and Dissertations by an authorized administrator of ScholarWorks@UARK. For more information, please contact scholar@uark.edu, ccmiddle@uark.edu.

On the Fatigue of Headed Shear Studs in Steel-Concrete Composite Bridge Girders

A dissertation submitted in partial fulfillment
of the requirements for the degree of
Doctor of Philosophy in Engineering

by

Brianna Ovuoba
Brigham Young University
Bachelor of Science in Civil Engineering, 2010

December 2017
University of Arkansas

This dissertation is approved for recommendation to the Graduate Council.

Dr. Gary Prinz
Dissertation Chair

Dr. Micah Hale
Committee Member

Dr. Shengfan Zhang
Committee Member

Dr. Cahn Dang
Committee Member

ABSTRACT

Shear connectors are commonly used in steel bridges to join the concrete deck and steel superstructure, providing a mechanism for shear transfer across the steel-concrete interface. The most common shear connector is the headed shear stud. In the current AASHTO LRFD Bridge Specifications on composite design, shear stud fatigue often governs over static strength, and a large number of shear connectors often result. This dissertation investigates headed shear stud fatigue capacities and demands, and provides insight into conservancies in existing design specifications through examination of existing high-traffic bridge performance.

To investigate stud capacity, a total of six high-cycle fatigue tests are conducted on stud pushout specimens at low stress ranges and combined with existing experimental data to develop probabilistic S-N fatigue capacity curves. Results from composite push-out specimens tested at stress ranges between 4.4 and 8.7 ksi suggest a fatigue limit of 6.5 ksi, which is near the existing limit of 7 ksi. Recommendations for modification of the existing AASHTO finite-life shear stud S-N fatigue capacity curve are proposed.

In addition to experimental testing, a finite element parametric study considers the effects of stud pitch, girder depth, and girder span on shear flow demands. Results from the parametric study indicate that the shear forces within stud clusters are not captured by current AASHTO shear flow demand estimations. A new design method and updated formulation for predicting stud demands are presented.

To examine high-traffic bridge performance, residual fatigue life is investigated by further fatigue testing, as well as magnetic particle inspection and dye penetrant testing on two existing bridges. The lack of discovered fatigue cracks within the studs of the bridges investigated suggests that the shear stress range estimation in AASHTO specification is higher

than what is actually experienced. This discrepancy is likely due to shear transfer through adhesion and friction, which are not considered in AASHTO design calculations. Fatigue tests from sections of the decommissioned bridge exceeded the design life expectancy of approximately 850,000 cycles (at 11.6 ksi) by over 2,500,000 cycles. This evidence further indicates that stud fatigue is an unlikely failure mode during service loading.

ACKNOWLEDGEMENTS

This work was possible due to financial and in-kind support from W&W|AFCO Steel and was conducted in the Steel Structures Research Laboratory (SSRL) at the University of Arkansas. I am grateful for the guidance, encouragement, and mentorship of Dr. Gary Prinz and the expert advice provided throughout by committee members Dr. Micah Hale, Dr. Shengfan Zhang, and Dr. Canh Dang. Laboratory staff and graduate students instrumental in the completion of this work include: David Peachee, Ryan Hagedorn, Richard Deschenes, Bryan Casillas and Joseph Daniels. Finally, I would like to acknowledge my family for their support and my husband, Paul, for his never-ending encouragement and support, without which this would not have been possible.

TABLE OF CONTENTS

Chapter 1: Introduction	1
1.1 Background	1
1.1.1 Overview of Current Fatigue Provisions for Headed Shear Studs	2
1.2 Research Needs and Objectives	8
1.3 Organization of the Dissertation	11
Chapter 2: Experimental Investigation into the Fatigue Capacity of Headed Shear Studs	14
2.1 Background	14
2.2 Experimental Program	17
2.2.1 Test Specimen Geometry and Fabrication	17
2.2.2 Test Configurations, Instrumentation, and Loading	19
2.3 Experimental Results	21
2.3.1 Observations and Measured Fatigue Life	21
2.3.2 Stud Fatigue-Crack Investigations	23
2.4 Probabilistic Approach to Shear Stud Fatigue Capacity Evaluation	25
2.4.1 Overview of MLE	25
2.4.2 Influence of Run-Outs on CAFL	28
2.4.3 Shear Stud Fatigue Dataset and Analysis using MLE	28
2.5 Proposed Design S-N Curve for Predicting Shear Stud Fatigue Capacity	30
2.6 Summary and Conclusions	32
Chapter 3: Analysis of Shear Demands Near the Steel-Concrete Interface in Composite Bridge Girders having Varied Stud Pitch, Girder Depth, and Span Length	34
3.1 Background	34
3.3 Parametric Investigation	35
3.3.1 Prototype Bridge Designs and Stud Spacing Variations	35
3.2.3 Modelling Methods	37
3.2.3.1 <i>Materials, Elements, Boundary Conditions, and Meshing</i>	37
3.2.3.2 <i>Composite Slab Connection Modeling</i>	39
3.2.3.3 <i>Bridge Loading</i>	41
3.2 Validation of Modeling Techniques from Full-Scale Girder Tests	42
3.2.1 Description of Tests performed at TFHRC	43
3.2.2 Description of Tests performed at University of Nebraska	45
3.2.4 Model Validation using TFHRC Tests with Pocketed Studs	46
3.2.4 Model Validation using University of Nebraska Composite Beam Tests	47

3.4 Results and Discussion	48
3.4.1 Development of Demand Equations for Clustered Studs Having Pitch greater than 24”	52
3.5 Summary and Conclusions	55
Chapter 4: Determination of Residual Fatigue Life in the Shear Studs of Existing Composite Bridge Girders Following Decades of Traffic Loading	58
4.1 Background.....	58
4.2 Experimental Program	60
4.2.1 Bridge Descriptions and Traffic Loading.....	60
4.2.2 Overview of Non-Destructive Testing Methods	63
4.2.2.1 <i>Overview of Magnetic Particle Inspection</i>	64
4.2.2.2 <i>Overview of Dye Penetrant Testing</i>	65
4.2.3 Overview of Experimental Fatigue Testing	67
4.2.3.1 <i>Test Specimen Geometry and Fabrication for Fatigue Testing</i>	67
4.2.3.2 <i>Test Configuration, Instrumentation, and Loading</i>	69
4.3 Results.....	72
4.3.1 Magnetic Particle / Dye Penetrant Testing.....	72
4.3.2 Fatigue Testing	78
4.3.3 Stud Fatigue-Crack Investigations	83
4.4 Summary and Conclusions	84
Chapter 5: Summary, Conclusions, Contributions, and Areas for Future Research	86
5.1 Experimental Investigation into the Shear Capacity of Headed Shear Studs	86
5.2 Analysis of Shear Demands Near the Steel-Concrete Interface	87
5.3 Determination of Residual Fatigue Life in the Shear Studs of Existing Composite Bridge Girders.....	89
5.4 Contributions to Composite Bridge Design	89
5.5 Recommendations for Future Work.....	90
References	91
Appendix A. Shear Stud Fatigue Dataset	96
Appendix B. Concrete Cylinder Fabrication and Testing	99
Appendix C. Verification of Negligible Inertial Effects under High Frequency Loading .	101
Appendix D. Additional Slip and Separation Measurements	103
Appendix E. Turner Fairbanks Highway Research Center Test Details	104
Appendix F. Example Design Calculation for Girder	107

LIST OF FIGURES

Figure 1 (a) Shear stud mechanism for load transfer across the steel-concrete interface, and (b) shop installed shear studs on a plate girder (photo courtesy of Bill McEleney, NSBA)	1
Figure 2 Shear studs welded to surface and depiction of increasing stud pitch along the length of the girder up to mid-span.	2
Figure 3 Sample geometry, loading, and features of fatigue detail categories A, C, and E [1].....	3
Figure 4 S-N curves for fatigue detail categories	5
Figure 5 S-N curve for shear studs compared to S-N curve for fatigue detail categories	6
Figure 6 Assumed uniform shear flow vs. actual shear transfer at discrete locations	7
Figure 7 Horizontal shear force range determined for partitioned girder sections to allow for discrete pitch variation	8
Figure 8 S-N curve for headed shear studs	9
Figure 9 showing a large number of shear studs welded to the top flange of steel beams	10
Figure 10 Comparison of design S-N curves for shear stud fatigue capacity between the AASHTO and Eurocode standards	16
Figure 11 Push-out specimen geometry and slab rebar locations (all dimensions provided in mm) [15].	18
Figure 12 Casting of concrete slabs on double sided push-out specimens	19
Figure 13 (a) Experimental setup and (b) specimen instrumentation	20
Figure 14 Shear stud failure mode observations for Specimen 1 (failure observed after 12,803,000 cycles at an applied stress range per stud of 8.7ksi).....	22
Figure 15 Average slip versus number of applied cycles for Specimens 1 and 5.	23
Figure 16 Fatigue crack investigation of polished stud sections from (a) Specimen 2 and (b) Specimen 5	24
Figure 17 Fatigue-life curve representation through MLE fitting	27
Figure 18 Comparison of AASHTO S-N curve and MLE regression	30

Figure 19 (a) Comparison of proposed design S-N curve, MLE regression, fatigue data, and current AASHTO curve; (b) Comparison of proposed design S-N curve and existing AASHTO fatigue details; (c) comparison of proposed curve with fatigue data from additional stud	32
Figure 20 Details of pitch and girder depth variation	36
Figure 21 Girder views showing typical boundary conditions and support constraints.	38
Figure 22 Typical girder finite element model mesh.....	39
Figure 23 Simulated shear studs composed of multiple springs with stiffness values in the X, Y, and Z directions.....	40
Figure 24 shows slide-plane connections between the steel and concrete.....	41
Figure 25 AASHTO fatigue truck characteristics and applied loads [1]	41
Figure 26 Loads and corresponding amplitude layout.....	42
Figure 27 Schematic of cluster and pitch arrangement in TFHRC tests.....	43
Figure 28 Plan and elevation views of test TRHRC 1	44
Figure 29 Static load test setup for TFHRC 1 (plan and elevation views)	44
Figure 30 shows elevation view of beam, which is the same for UN1 and UN2, and end views of UN1 and UN2 showing the differences in deck and steel	46
Figure 31 shows load v. deflection results from TFHRC tests and finite element model tests	47
Figure 32 Load vs. deflection global results from University of Nebraska tests and finite element model predictions	48
Figure 33 Shear force range in studs for finite element models of 100ft length	49
Figure 34 Shear force range in studs for finite element models of 200ft length	50
Figure 35 Shear force concentrations in rows within a cluster as load travels across surface	50
Figure 36 Definition of terms in development of p_c spacing	52
Figure 37 Shear stress range of 100ft span FE models with proposed V_{SR} calculation.....	55
Figure 38 Shear stress range of 200ft span FE models with proposed V_{SR} calculation	55
Figure 39 Distribution of the age of steel bridges within the United States	58
Figure 40 Location of Bridge A and Bridge B in Lowell and Russellville, Arkansas	61

Figure 41 Girder elevation view and span dimensions for Bridge A	61
Figure 42 Representation of 55 foot girder removed from Bridge B for testing	62
Figure 43 ADTT Estimations of (a) fatigue cycles per year and (b) total fatigue cycles experienced during the lifetime for Bridge A and Bridge B.....	63
Figure 44 Schematic of magnetic particle inspection process	64
Figure 45 Magnetic particle testing done on shear studs of Bridge A.....	65
Figure 46 a) dye penetrant testing process b) dye penetrant testing of Bridge A.....	67
Figure 47 a) Fabrication of steel double sided specimen b) push-out specimen dimensions	68
Figure 48 Placing concrete on steel beam sections by greasing steel flange, placing rebar, and casting concrete in horizontal position.....	69
Figure 49 Experimental setup for pushout specimen fatigue testing showing: A) test set up plan view; B) specimen LVDT configuration; C) test setup B) elevation view; and D) image of test setup	71
Figure 50 showing shear stud bend to a 90 degree angle as a result of being hit with a jackhammer during concrete removal. Shear stud is still attached firmly to the steel flange	73
Figure 51 Shows penetrant applied and the developer being sprayed onto 6 shear studs	73
Figure 52 Magnetic particle testing and inspector	74
Figure 53 Report for DPI and MPI on 18 studs of Bridge A.....	74
Figure 54 Design shear stud stress range vs. actual shear stud stress range in Bridge A.....	76
Figure 55 Results of dye penetrant testing of Bridge B.....	77
Figure 56 Results of magnetic particle testing of Bridge B.....	78
Figure 57 AASHTO design curve compared to failure points of tests R1, R2, R3	79
Figure 58 a) Test specimen before testing b) Test specimen failure c) Steel flange of test specimen showing divots where stud failed along base of weld through steel flange d) Concrete deck of specimen with shear studs embedded in deck	80
Figure 59 Test R2 failure of two shear studs and near failure of third shear stud	81
Figure 60 Slip and separation results for Tests R2 and R3.....	82

Figure 61 Cracks found in shear studs of test R2 and test R3 following deck removal and metallographic preparation of sectioned stud surface..... 84

Figure 62 Suggestions for design of pitch of clustered shear studs 88

APPENDIX FIGURES:

Figure A-1. Common (type A, B, and C) fatigue fractures within shear stud connectors96

Figure B-1. Concrete testing machine and cylinder dimensions99

Figure C-1. Comparison of slab slip measurements for Specimen 5 during high frequency dynamic loading. Comparisons presented represent (a) 1Hz and 10Hz loading rates, and (b) 1Hz and 20Hz loading rates102

Figure D-1. (a) Slip and (b) separation data from external LVDT measurements103

LIST OF TABLES

Table 1 AASHTO Detail category S-N curve parameters.....	4
Table 2 Specimen Testing Matrix and Fatigue Results	21
Table 3 Proposed detail category description for shear stud fatigue capacity	31
Table 4 Analysis Matrix for Parametric Investigation.....	36
Table 5. Stud Pitch for TFHRC tests	43
Table 6 Experimental Test Matrix for tests R1, R2, and R3.....	72
Table 7 Results of Residual Shear Fatigue Life Tests	79

APPENDIX TABLES:

Table A-1: Fatigue dataset for 3/4" diameter shear studs.....	96
Table B-1: Concrete compression test data for push-out specimen slabs.....	100

NOTATION

The following terms are used in the text of this dissertation:

$(\Delta F)_n$	=	design load-induced fatigue resistance;
$(\Delta F)_{TH}$	=	the constant amplitude fatigue limit;
A	=	constant representing the intercept of the fatigue S-N curve;
$ADTT_{SL}$	=	single-lane average daily truck traffic (trucks);
BM	=	base metal;
$CAFL$	=	constant amplitude fatigue limit;
$CDF_{N_i, S_i \gamma'}$	=	cumulative density function assuming γ' ;
d	=	diameter of shear stud;
f'_c	=	concrete compressive strength;
f_{N_i}	=	probability of predicting failure at an individual data point;
$f_{N_i \gamma'}$	=	probability of having failure at each given data point;
FZ	=	weld fusion zone;
$f_{\gamma'}$	=	probability that γ' exists;
HAZ	=	weld heat affected zone;
I	=	moment of inertia of the short-term composite section;
L	=	joint probability or likelihood;
$LVDT$	=	linear variable differential transducers;
m	=	constant representing the slope of the fatigue S-N curve;
MLE	=	maximum likelihood estimation;
N	=	number of cycles;
n	=	number of shear studs across the flange width;
n	=	required number of studs for the strength limit state;
N_f	=	number of cycles to failure;
n_f	=	total number of failure points;
n_r	=	number of rows of shear studs within a cluster;
n_r	=	total number of run-out points;
p	=	pitch (or spacing) of the row of shear studs along the length of the steel beam;
P	=	total nominal shear force;

- p_c = center to center pitch of clustered shear studs;
- PDF_{N_i} = marginal probability density function;
- $PDF_{N_i, S_i | \gamma'}$ = probability density function of failure at each given point;
- PDF_{N_i, θ_i} = probability density function at fatigue test data point (N_i, θ_i) ;
- Q = first moment of the transformed short-term area of the concrete deck about the neutral axis of the short-term composite section;
- Q_r = factored shear resistance of one shear connector;
- R_{N_i} = probability of run-out;
- $R_{N_i | \gamma'}$ = probability of predicting run-out;
- S = applied stress range;
- s = spacing between rows of shear studs within a cluster;
- V_f = vertical shear force range under the applicable fatigue loads;
- V_{sr} = applied shear demand at the steel-concrete interface;
- z^* = number of standard deviations shifted from the mean;
- Z_r = fatigue shear resistance of an individual shear stud;
- γ' = assumed constant amplitude fatigue limit;
- $\Delta\sigma$ = applied stress range;
- α = maximum likelihood fatigue-life curve parameter (power law constant);
- β = maximum likelihood fatigue-life curve parameter (power law constant);

Chapter 1: INTRODUCTION

1.1 Background

Shear connectors are commonly used in steel bridges to join the concrete deck and steel superstructure, providing a mechanism for shear transfer across the steel-concrete interface. Joining the steel and concrete members is advantageous, as the composite steel-concrete section has added strength over the sum of the individual components (the steel girder and concrete deck). This allows for use of lighter steel members and improved economy. The most common type of shear connector is the headed shear stud (see Figure 1).

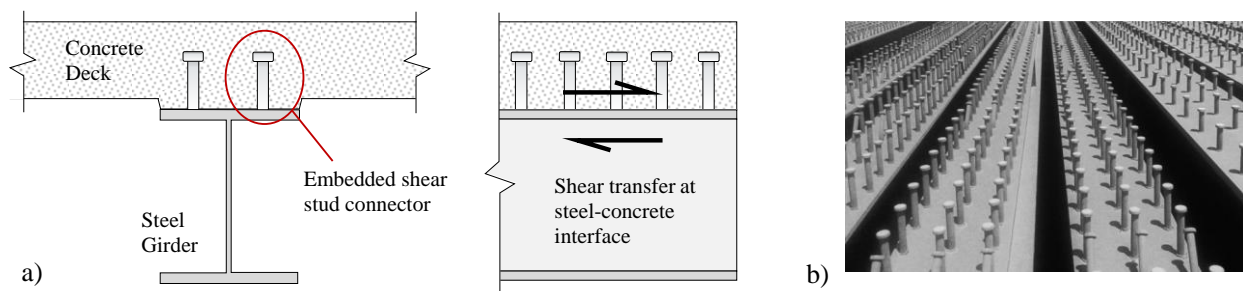


Figure 1 (a) Shear stud mechanism for load transfer across the steel-concrete interface, and (b) shop installed shear studs on a plate girder (photo courtesy of Bill McEleney, NSBA)

Headed shear studs are often welded to the girder flange at varying longitudinal spacings (called pitches) to accommodate shear demands that develop at the steel-concrete interface during traffic loading (see Figure 2). The stud pitch (p), representing the distance between rows of studs, is determined from a capacity-to-demand ratio. In this capacity-to-demand ratio, the stud demands assume a continuous longitudinal shear flow (V_{sr}) at the steel-concrete interface while the stud capacities (Z_r) are based on empirical fatigue testing and an assumed fatigue limit (see Equation 1). Both strength and fatigue limit states exist and must be checked during the

composite girder design; however, shear stud fatigue often governs over static strength, and a large number of shear connectors often result (see again Figure 1(b)).

$$p \leq \frac{nZ_r}{V_{sr}} \quad \text{(Equation 1) AASHTO [1]}$$

In Equation 1, the stud pitch (p) varies depending upon the interface shear flow (V_{sr}), the individual stud shear fatigue capacity (Z_r), and the number of studs per row across the girder flange (n) (see again Figure 2).

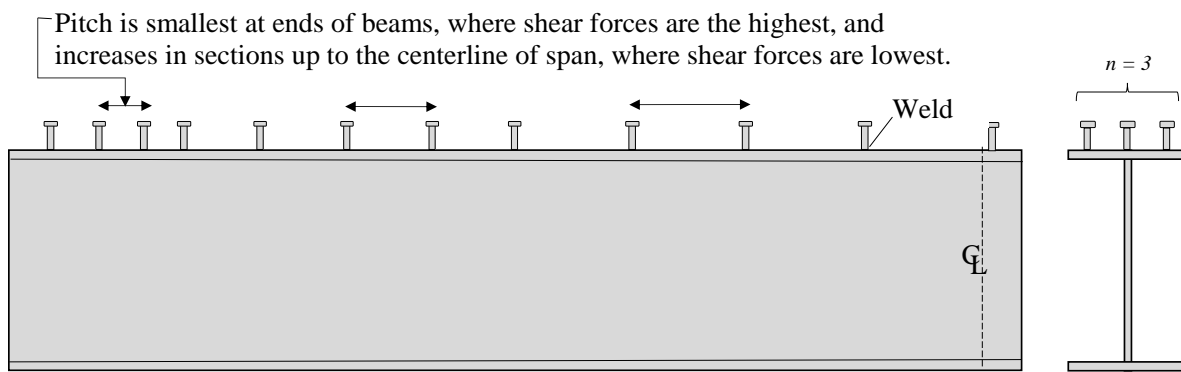


Figure 2 Shear studs welded to surface and depiction of increasing stud pitch along the length of the girder up to mid-span.

1.1.1 Overview of Current Fatigue Provisions for Headed Shear Studs

Guidance on various demand and capacity calculations for steel and concrete bridge components is provided by the American Association of State Highway Transportation Officials (AASHTO) bridge design specifications [1]. With fatigue being a primary concern for many bridge components (due to the nature of the repeated traffic loading), the AASHTO specifications provide detailed methods for addressing component fatigue in design.

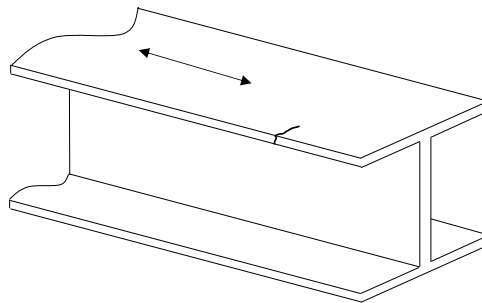
Current fatigue design specifications are based on 8 fatigue detail categories largely determined from experimental studies conducted in the 1960s and 1970s in the United States and in Great Britain [2]. These 8 fatigue detail categories are characterized by the alphabetic symbols

A, B, B', C, C', D, E, and E' with lower fatigue capacities typically corresponding to higher alphabetic characters (i.e., “*A*” details have higher fatigue capacity than “*D*” details, etc.). The derivation of the detail categories defining the component fatigue life take into account fabrication processes (welding, cutting, grinding etc.), nominal loading direction, and component geometry [2]. Figure 3 describes and depicts a few common *A*, *C*, and *E* fatigue details, including their geometry, loading, and the location and orientation of weld features.

Category A:

Base metal, except noncoated weathering steel, with rolled or cleaned surfaces. Crack initiating away from all welds or structural connections.

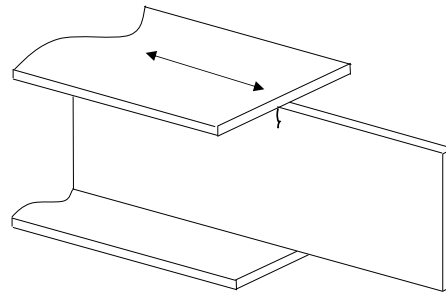
Constant $A = 250 \times 10^8 \text{ ksi}^3$
 Threshold = 24ksi



Category C:

Member with re-entrant corners at copes, cuts, or block-outs or other geometrical discontinuities, except weld access holes. Initiation in the base metal at the discontinuity.

Constant $A = 44 \times 10^8 \text{ ksi}^3$
 Threshold = 10 ksi



Category E:

Base metal at the net section of eyebar heads of pin plates. Initiation of crack in the net section originating at the side of the hold.

Constant $A = 11 \times 10^8 \text{ ksi}^3$
 Threshold = 4.5 ksi



Figure 3 Sample geometry, loading, and features of fatigue detail categories A, C, and E [1]

In order for a satisfactory component fatigue design, capacities must exceed demands. In the AASHTO specification, this relationship is defined by Equation 2 where $(\Delta F)_n$ is the nominal fatigue capacity of a given component or detail, (Δf) is the live load stress range due to the passage of the moving fatigue load, and γ is the appropriate fatigue limit-state load factor. The nominal fatigue capacity of a given component or detail is determined by either Equation 3 or Equation 4 depending on the expected design life (Fatigue I for infinite life and Fatigue II for finite life), where $(\Delta F)_{TH}$ is the constant amplitude fatigue limit (CAFL) or threshold and A is a constant specific to the detail category (see Table 1). Fatigue demands (Δf) are determined through structural analysis of the bridge components during the applied AASHTO fatigue-load truck. The fatigue limit factor (γ) is equal to 1.5 for infinite fatigue life (Fatigue I load combination) and 0.75 for finite fatigue life (the Fatigue II load combination) [1].

$$\gamma(\Delta f) \leq (\Delta F)_n \quad \text{Equation 2}$$

$$(\Delta F)_n = (\Delta F)_{TH} \quad \text{for Fatigue I} \quad \text{Equation 3}$$

$$(\Delta F)_n = \left(\frac{A}{N}\right)^{\frac{1}{3}} \quad \text{for Fatigue II} \quad \text{Equation 4}$$

Table 1 AASHTO Detail category S-N curve parameters.

Detail Category	Constant A (x10 ⁸ ksi)	Constant Amplitude Fatigue Limit (ksi)
A	250.0	24.0
B	120.0	16.0
B'	61.0	12.0
C	44.0	10.0
C'	44.0	12.0
D	22.0	7.0
E	11.0	4.5
E'	3.9	2.6

Equations 2 through 4 represent the relationship between the constant amplitude applied stress ranges and the number of cycles leading to failure, termed an S-N curve. If the component or detail applied stress range is below the CAFL, then the component is assumed to have an infinite fatigue life (applicable for Fatigue I design). For Fatigue II design, the fatigue resistance is a function of the number of cycles (N) expected in the finite lifetime of 75 years as shown in Equation 4, in which:

$$N = (365)(75) n (ADTT_{SL}) , \quad \text{Equation 5}$$

where $ADTT_{SL}$ represents the average daily truck traffic for a single lane. Plots of the S-N curves for each detail category are shown in Figure 4, along with a few examples of components corresponding to the detail categories. Note in Figure 4 that each of the 8 detail categories are represented by a log-log regression [1].

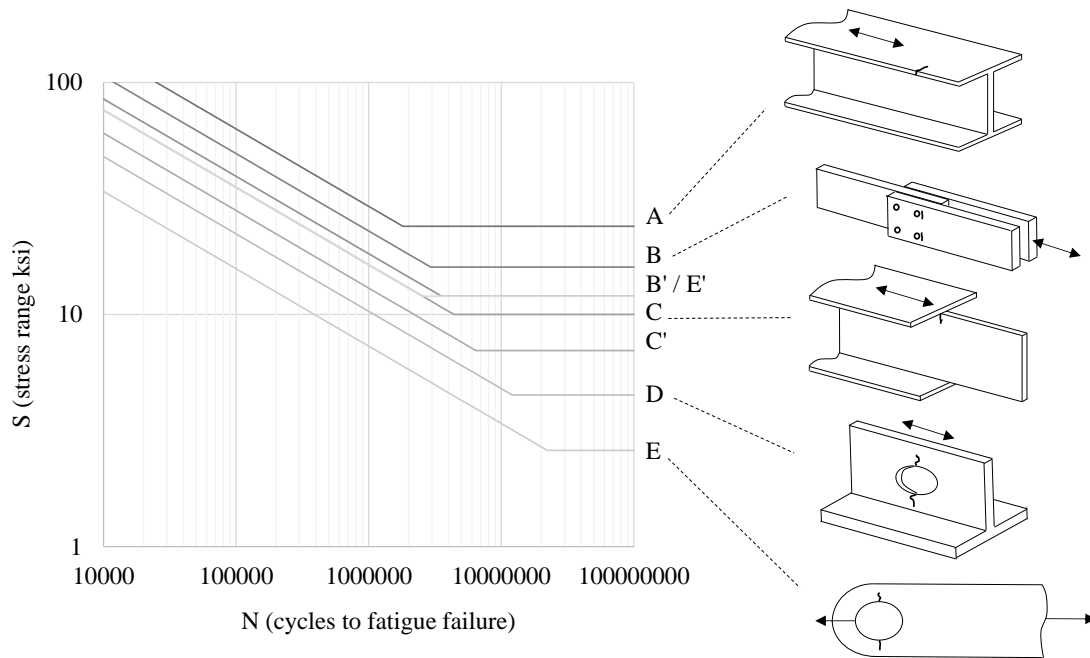


Figure 4 S-N curves for fatigue detail categories

One exception to the log-log regression fatigue detail categories is the shear stud fatigue S-N curve, shown in Figure 5, which assumes a linear-log regression within the finite life fatigue

range. The fatigue capacity of headed shear studs is governed by Equation 6, where $\Delta\sigma$ is the applied stress range and N is the number of cycles to fatigue failure. More discussion on the development of this equation is provided in Chapter 2.

$$\log(N) = 8.061 - 0.1834 \Delta\sigma$$

Equation 6 AASHTO [1]

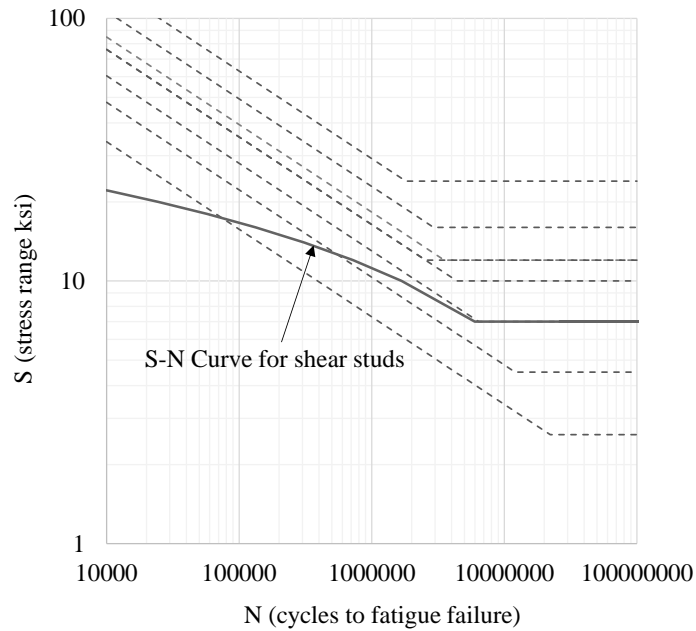


Figure 5 S-N curve for shear studs compared to S-N curve for fatigue detail categories

The stud fatigue capacity (Z_r) shown in Figure 5 is determined by either Equation 7 or Equation 9 depending on finite or infinite life, where d is the diameter of the shear stud and N is the number of cycles expected during the service life of the girder. More discussion is given to the shear stud fatigue capacity in Chapter 2.

$$Z_r = 5.5d^2 \quad (\text{For infinite life – Fatigue I}) \quad \text{Equation 7}$$

$$Z_r = \alpha d^2 \quad (\text{For finite life – Fatigue II}) \quad \text{Equation 8}$$

$$\text{Where: } \alpha = 34.5 - 4.28 \log N \quad \text{Equation 9}$$

Fatigue demands on shear studs are determined assuming uniform shear flow at the concrete-steel interface. The horizontal fatigue shear range (V_{sr}) is assumed to be continuous across the section being analyzed even though the actual shear transfer occurs at discrete stud locations (see Figure 6). A horizontal fatigue shear range (V_{sr}) is calculated using influence line analysis which allows determination of the maximum live-load shear demand throughout the girder length. To improve design-economy and simplify construction, it is common to partition girder spans and calculate V_{sr} (see Equation 10) at discrete locations along the girder span. This simplifies girder fabrication and allows for conservancy in the composite load transfer by preventing a continuously varying stud pitch (see Figure 7).

$$V_{sr} = \frac{vQ}{I} \quad \text{Equation 10}$$

In Equation 10, V is the vertical shear force range under the applicable load combinations; Q is the first moment of the transformed short-term area of the concrete deck about the neutral axis of the short term composite section; and I is the moment of inertia of the short term composite section. Note that if the girder is curved throughout the span, an additional radial fatigue shear range must be used; however, only straight girders are considered in the scope of this study, and the radial fatigue shear range is neglected.

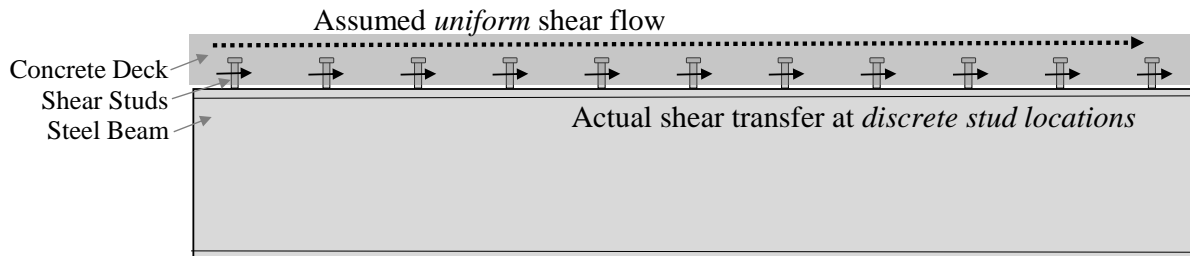


Figure 6 Assumed uniform shear flow vs. actual shear transfer at discrete locations

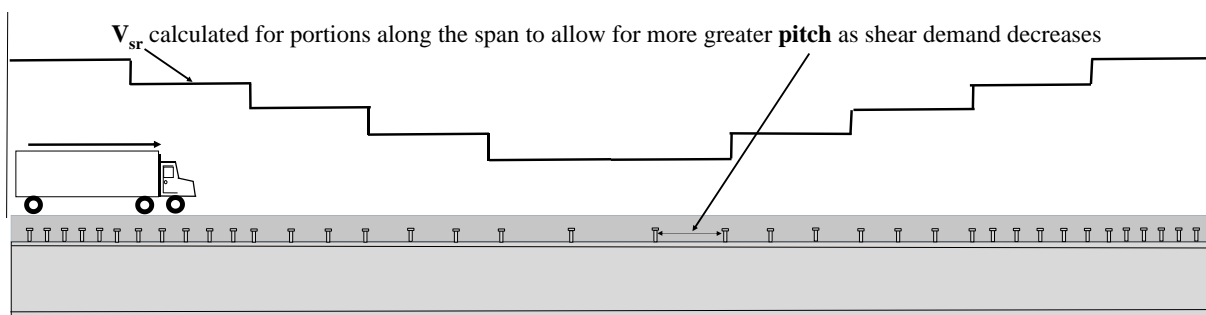


Figure 7 Horizontal shear force range determined for partitioned girder sections to allow for discrete pitch variation

1.2 Research Needs and Objectives

In the current version of the AASHTO standard [1], the headed shear stud fatigue capacity equation (Equation 6) is largely based on a limited sample of composite fatigue tests performed in the 1960s [3-5], with limited fatigue test data at lower stress ranges leading to a somewhat arbitrary constant amplitude fatigue limit (CAFL). Figure 8 shows the resulting AASHTO fatigue-life stress versus number of cycles to failure (S-N) curve used for headed shear studs. In Figure 8, the horizontal CAFL of the AASHTO curve is arbitrarily set at 7 ksi (48.3 MPa) (due to a lack of experimental data) and reduced by half to 3.5ksi (24.1 MPa) to account for variable amplitude effects. This somewhat arbitrary CAFL often governs the composite design of most bridges with moderate-to-high traffic demands and results in nearly twice as many studs than would be required for static strength. Research is needed to investigate the validity of the CAFL as there is a lack of supporting experimental data for this limit.

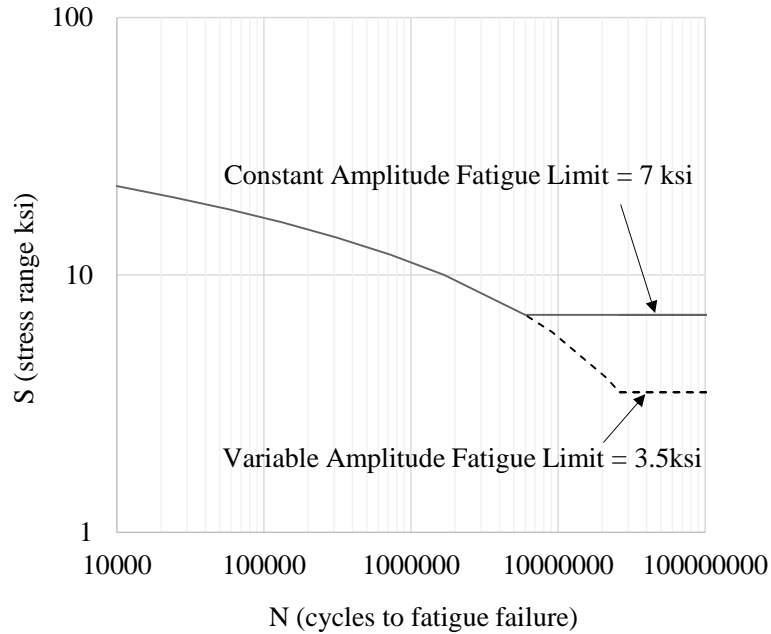


Figure 8 S-N curve for headed shear studs

Figure 9 shows a typical bridge girder fabricated with a large number of shear studs welded to a girder flange resulting from the abovementioned AASHTO provisions. In addition to economic consequences that result from many required shear studs, the close stud pitch shown in Figure 9 can also lead to safety issues, as workers must often traverse the girder top flange during erection [6]. According to Iron Workers International [7], tripping accidents resulting from these pre-installed studs are a “*primary causation factor in many fatalities.*” Increasing the allowable stud pitch and allowing grouped stud configurations would help alleviate these tripping issues while also accommodating the use of precast concrete decks for accelerated bridge construction.

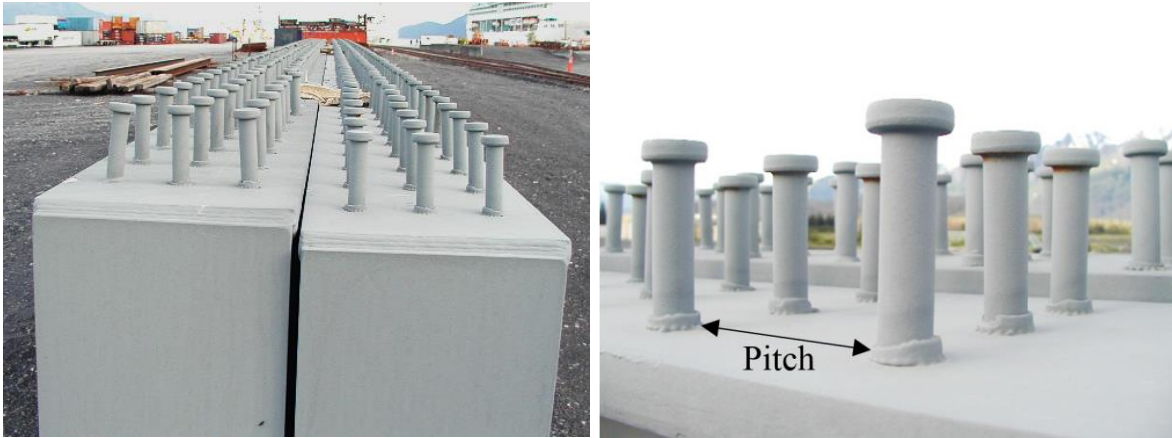


Figure 9 showing a large number of shear studs welded to the top flange of steel beams

Currently, the maximum allowable stud pitch (capped at 24 inches in the current AASHTO specification) limits the use of many accelerated bridge construction (ABC) technologies, such as pre-cast concrete decks. Many researchers have proposed expanding this limit [8, 9] and in fact the new version of the AASHTO specification will somewhat relax this limit to allow stud spacing at a maximum of the girder depth up to 48 inches. This expansion is based on limited research at the Federal Highway Turner Fairbanks Highway Research Center (TFHRC) which involved a limited number of shallow-depth composite beam fatigue tests [10]. In the work performed at the TFHRC, 4 large-scale static shear tests and 7 large-scale fatigue tests were completed. The results indicate that extended shear stud spacing has little effect on concrete deck uplift or relative slip between the deck and the steel girder [10]. It is important to note however, that all composite specimens tested in the TFHRC study were W27x84 girder sections having a shallow girder depth of 26.7 inches.

While researchers have sought to expand the allowable stud spacing [8-10], limited research has been done to investigate the effects of this increase on the resulting shear demands. As mentioned earlier, existing equations assume a constant shear flow of demand at the steel-

concrete interface (see again Equation 1); however, load is always assumed to transfer through studs which have discrete flange attachment locations. Note that concrete-to-steel adhesion and friction at the interface are ignored in the load transfer process. Research on the maximum allowable stud spacing and the resulting shear demands at the concrete interface is needed to provide guidance on this issue.

The abovementioned issues related to the development of the fatigue capacity equations and maximum stud spacing, combined with the lack of empirical evidence suggesting any fatigue issues within existing composite girder studs, initiated this study to investigate fatigue capacities and demands for headed shear studs in traditionally fabricated composite bridge girders.

This study aims to:

- 1) Re-evaluate the existing (arbitrary) CAFL for headed shear studs through statistical analysis of fatigue push-out tests. A novel probabilistic approach will be used to capture fatigue data uncertainty and allow the creation of characteristic capacity curves of similar form to other fatigue detail categories in AASHTO.
- 2) Determine the validity of the existing shear flow demand equation at larger stud spacings and propose alternative stud demand equations based on parametric analytical investigations.
- 3) Investigate residual fatigue life in existing highway bridge studs, following decades of in-service loading. Both non-destructive and destructive crack investigations will allow insight into actual composite girder stud performance.

1.3 Organization of the Dissertation

The dissertation covers three main research parts related to the needs and objectives mentioned above. These research parts involve: (1) an experimental investigation into the

fatigue capacity of headed shear studs designed to re-evaluate the existing AASHTO CAFL; (2) an analytical investigation into headed shear stud demands, considering effects of girder depth, span length, and shear stud spacing (pitch) during traffic loading; and (3) a destructive and non-destructive investigation of residual fatigue capacity for headed shear studs taken from existing bridge girders subjected to decades of service. The following paragraphs describe the outline of the dissertation chapters.

The following chapter (Chapter 2) focuses on the re-evaluation of the existing AASHTO CAFL for headed shear studs. In this chapter, new experimental high-cycle fatigue tests, existing fatigue data from the literature, and advanced statistical techniques are all used to develop probability-based fatigue-life curves for headed shear studs. Modifications to the current AASHTO finite-life fatigue capacity curve are proposed based on the probabilistic analyses.

Chapter 3 investigates shear demands at the steel-concrete interface during traffic loading. This chapter investigates the effects of stud spacing (using grouped studs at various maximum allowable spacings), girder depth, and girder span on resulting shear distributions at the steel-concrete interface. Modifications to the AASHTO shear flow equation are proposed for grouped stud configurations having larger than 24 inch center-to-center pitch.

Chapter 4 focusses on residual stud fatigue capacities and stud damage in existing bridge girders, following decades of high traffic loading. The chapter includes discussion from non-destructive magnetic-particle and dye-penetrant crack investigations on the studs of existing bridge girders. In addition, destructive fatigue push-out tests fabricated from the flanges of existing high-traffic bridge girders are presented to help understand stud residual fatigue capacity. Historic traffic count data are combined with these destructive and non-destructive

tests to provide insights into accumulated bridge damage during many years of traffic loading, and to provide anecdotal evidence for potential conservancies in the current AASHTO stud design provisions.

Chapter 5 summarizes the research findings from the three research parts, presents conclusions related to the fatigue behavior of headed shear studs in composite bridge girders, and discusses areas for future research and further study.

Chapter 2: EXPERIMENTAL INVESTIGATION INTO THE FATIGUE CAPACITY OF HEADED SHEAR STUDS

This chapter presents results from an experimental study into the fatigue behavior of headed shear studs, to address the lack of existing experimental data near the assumed CAFL, and to better characterize the effects of fatigue uncertainty on predicted response. Results from composite push-out specimens tested at low stress ranges between 4.4ksi (30Mpa) and 8.7ksi (60 MPa) suggest a fatigue limit of 6.5ksi (44.8MPa) which is near the existing limit of 7ksi (48MPa). Recommendations for modification to the existing AASHTO shear stud finite life S-N fatigue capacity curve are proposed.

2.1 Background

As mentioned in Chapter 1, in the current AASHTO LRFD bridge specifications on composite design, shear studs must satisfy both strength and fatigue requirements[1]. To satisfy strength requirements, the shear connection between the concrete and steel elements must be capable of developing the full plastic capacity of the steel cross-section (create full composite action). To satisfy fatigue requirements, demands at the steel-concrete interface must be lower than the shear stud fatigue capacity as determined from an empirical fatigue capacity curve (called an S-N curve) and anticipated traffic cycles. Fatigue often governs, and a large number of shear connectors often result. Because traffic cycles are typically fixed from average daily truck traffic extrapolated over a 75-year design life, the S-N curve ultimately determines the required number of shear studs when the design is governed by fatigue.

While many studies have investigated shear stud fatigue [11, 4, 5, 12-15], the stud fatigue requirements in the AASHTO standard are largely based on single-sided push-out tests on 19mm (3/4 in) studs performed by Slutter and Fisher [4]. In the study by Slutter and Fisher, 26 samples

containing 19mm (3/4in.) diameter studs were fatigue tested under constant amplitude stress cycles ranging in value from 8ksi (55MPa) to 20ksi (138MPa). To relate the applied stress range to the expected number of cycles for stud fatigue failure (S-N curve equations), a least-squares regression approach was used. Equation 11 presents the stud capacity equation based on the 26 data points from Slutter and Fisher [4], which shows similarity with the current stud fatigue capacity presented in the AASHTO standard [1] (see Equation 12). Note that the least-squares approach for regression analysis fails to account for any uncertainty distribution in the fatigue response, and therefore prevents the creation of characteristic capacity curves having known confidence levels.

$$\log(N) = 8.072 - 0.1753 \Delta\sigma \quad \text{(Equation 11) Slutter and Fisher [4]}$$

$$\log(N) = 8.061 - 0.1834 \Delta\sigma \quad \text{(Equation 12) AASHTO [1]}$$

The current AASHTO fatigue requirements assume a lower shear stud fatigue capacity than comparable specifications throughout the world. Figure 10 shows again the current AASHTO shear stud design S-N curve along with a comparable curve from the European (Eurocode) standard [16]. Other shear stud S-N curves from the Japanese and British standards are similar in form to the Eurocode curve [17]. The AASHTO specification results in a lower estimation of stud fatigue capacity for all traffic demands, and considers a linear-log regression while the Eurocode, Japanese, and British standards consider log-log fatigue behavior. Note that the 3.5ksi (24MPa) fatigue limit shown in Figure 10 represents an effective "design" fatigue limit considering effects from variable amplitude loading (with the Fatigue I load factor of 2 incorporated [1]). This indicates a constant amplitude fatigue limit (CAFL) of 7ksi (48MPa) [1].

Limited fatigue test data exist at lower stress ranges to justify this CAFL location, which often governs the stud fatigue design for bridges with moderate-to-high traffic demands (ADTT

greater than approximately 960 vehicles). Comparing the required number of studs in a rural short span steel bridge design (having a span of 17.3m (57ft)) at various levels of truck traffic, Lee et al. [6] found that bridges designed to the US requirements needed nearly twice as many shear studs than the corresponding European, British, and Japanese designs. In [17], stud capacities for the US designs were always governed by fatigue requirements.

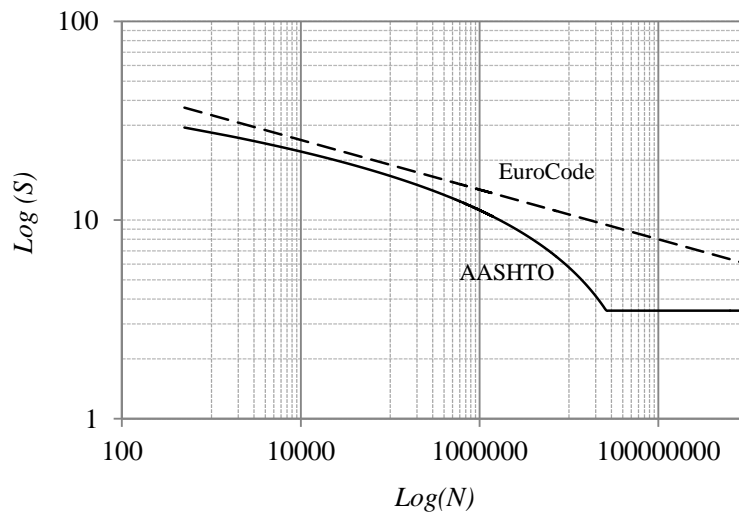


Figure 10 Comparison of design S-N curves for shear stud fatigue capacity between the AASHTO and Eurocode standards

This chapter presents an experimental and numerical study into the behavior of headed shear studs, to address the lack of existing experimental data near the assumed CAFL, and to better characterize the effects of fatigue uncertainty on predicted response. In this study, composite push-out specimens are fatigue tested at stress ranges near the existing AASHTO CAFL and a probabilistic approach is applied to both new and existing fatigue data to capture uncertainty and variation in the fatigue response.

The chapter begins by describing the experimental study, including the specimen geometry, test setup, instrumentation, and loading. Following, the experimental fatigue results are presented and a probabilistic method for fatigue data evaluation is described. Findings from

the experimental study are combined with existing data from previous studies to provide a comprehensive data set for re-evaluation of shear stud fatigue capacity. A characteristic S-N curve for estimating shear stud fatigue capacity is proposed and applied to five prototype bridge designs to provide comparison.

2.2 Experimental Program

The primary objectives of the experimental program are to 1) characterize stud fatigue capacity at low applied stress ranges, 2) re-evaluate the existing CAFL considering both run-out and failure test results, and 3) investigate stud crack formation during low-stress high-cycle fatigue loading.

2.2.1 Test Specimen Geometry and Fabrication

Figure 11 shows the experimental push-out specimen geometry, consisting of a rolled W10×54 wide-flange section having 4 headed shear studs and a 6 in. cast-in-place concrete slab on each flange. The chosen geometry for the specimens (called herein double-sided push-out specimens) is based on guidelines for shear-stud testing prescribed in the Eurocode [18]. Double-sided push-out specimens are advantageous over single-sided push-out specimens (having a slab on only one side) as they help reduce loading eccentricities and multi-axial stress states within the stud (combined tension and shear). An applied multi-axial stress state in the stud can provide an overly-conservative estimation of fatigue capacity [15, 19, 17]. In this study, a total of 6 double-sided push-out fatigue tests are performed at four different applied stress levels ranging in value from 4.4 ksi to 7 ksi (30MPa to 60MPa). Due to the significant time associated with high-cycle fatigue testing, only two replicate stress-ranges are considered in the test matrix (replicates at 5.8ksi and 8.7ksi).

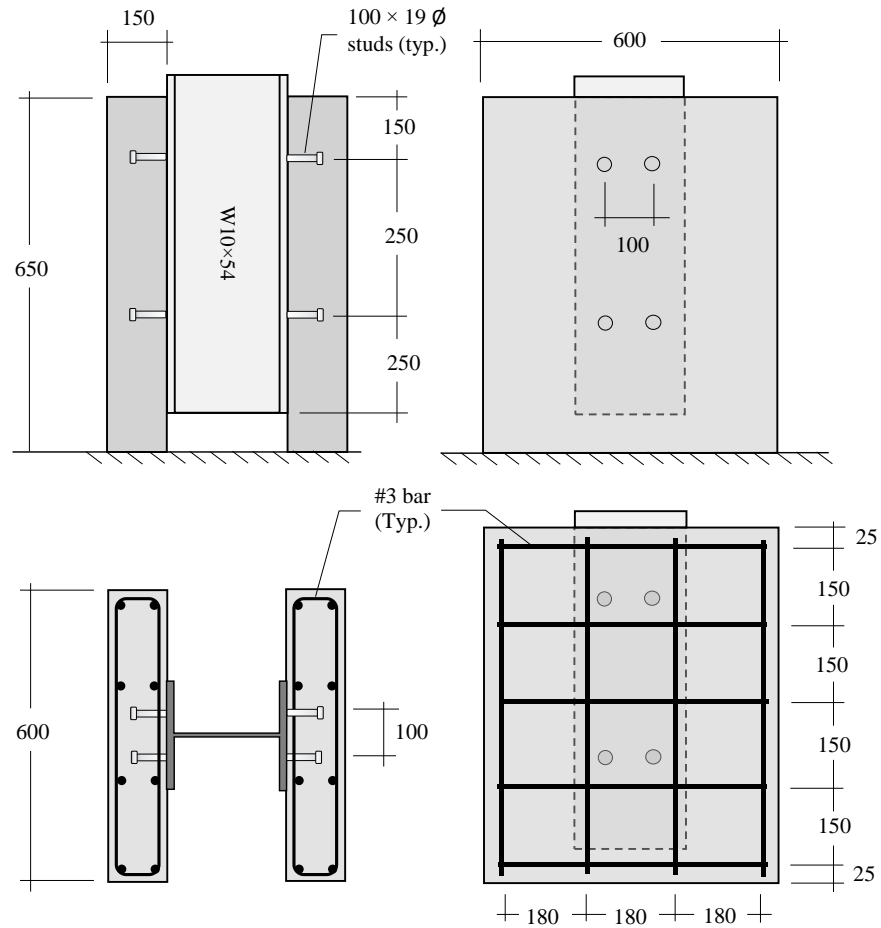


Figure 11 Push-out specimen geometry and slab rebar locations (all dimensions provided in mm) [15].

Concrete slabs of the test specimen are designed to represent typical composite bridge conditions. All concrete sections consider normal weight concrete from a standard highway bridge deck mix design [20], and each concrete section is cast with the beam in a horizontal position (see Figure 12). To ensure material consistency across the four different stress levels tested, four push-out specimens are simultaneously cast from the same concrete batch. Prior to each fatigue test, adequate concrete compressive strength (at least 80% f'_c) is checked from concrete cylinders formed during casting. Concrete strength data for each specimen are presented in Appendix B. To prevent adhesion between the concrete and steel, which can

contribute to load transfer across the steel-concrete interface, each steel flange was coated in grease prior to concrete casting [18].



Figure 12 Casting of concrete slabs on double sided push-out specimens

2.2.2 Test Configurations, Instrumentation, and Loading

The experimental setup, shown in Figure 13(a), is designed to apply rapid shear stress cycles to studs within the push-out specimens. As shown in Figure 13(a), the double-sided push-out specimens are loaded with the beam oriented vertically, and the axial loads applied to the end of the steel wide-flange section. All specimens are subjected to unidirectional loading (specimens are loaded in one direction and then unloaded), resulting in a non-zero mean stress and providing a conservative fatigue loading condition as compared to reversed cycle loading [4]. To prevent separation between the specimen and testing machine at unloading, a pre-load of 1kN is maintained (somewhat shifting the applied mean stress). To ensure uniform contact between the concrete slabs and testing machine base, each specimen was leveled using a gypsum grout mixture.

Linear variable differential transducers (LVDTs) and unidirectional strain gauges are used to provide local measurements during testing. A total of eight LVDTs oriented parallel and

perpendicular to the beam axis are included on each test specimen, to measure relative slip and separation between the concrete and steel sections. Unidirectional strain gauges are applied on two specimens to measure shear stresses transferred through the studs. Figure 13(b) shows the specimen instrumentation, including LVDT placement and strain gauge configurations.

Table 2 presents the experimental test matrix, including the specimen concrete strength, applied stress range, loading rate, and the resulting fatigue capacity. In Table 2, the applied stress ranges vary between 4.4ksi and 8.7ksi (30MPa and 60MPa) with specimen loading rates applied at between 10Hz and 20Hz. These high frequency loading rates are possible due to the high stiffness of the loading frame and test specimens. Note that measurements from several pseudo-static loading cycles applied at 1 Hz were used to verify negligible inertial effects at the higher frequency loading (see Appendix C for this verification). Fatigue results provided in Table 2 will be discussed in the following Results section.

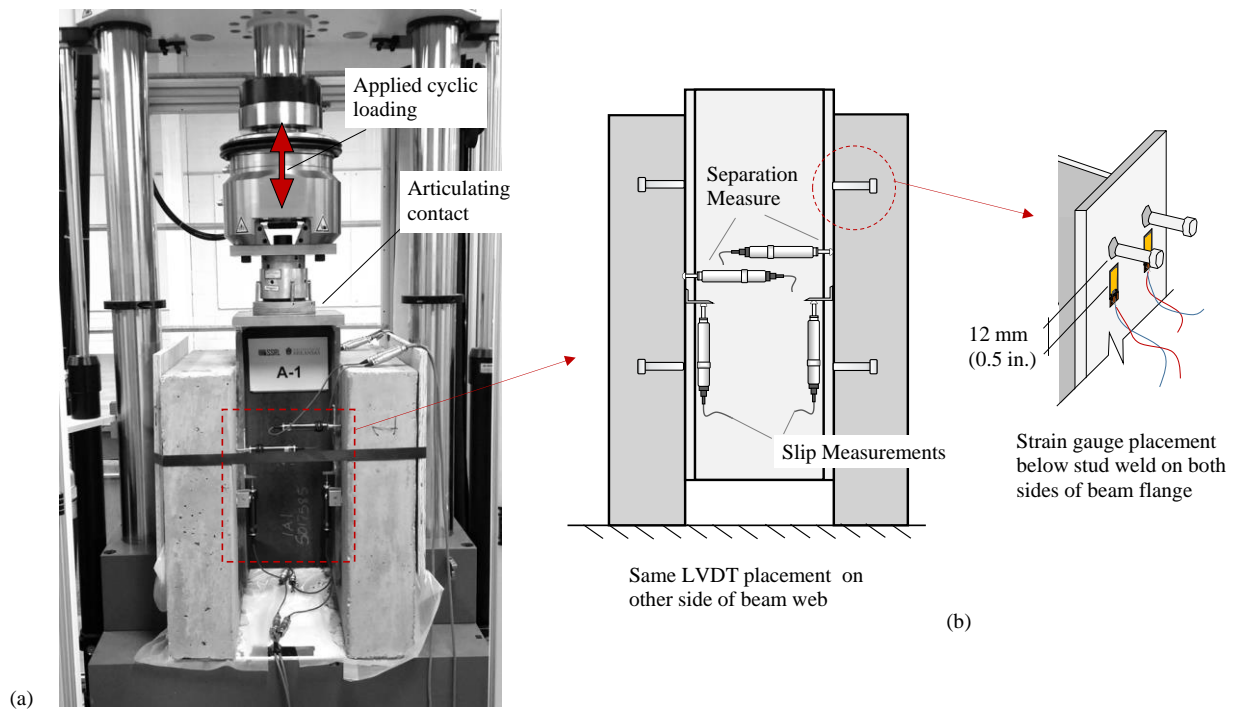


Figure 13 (a) Experimental setup and (b) specimen instrumentation

Table 2 Specimen Testing Matrix and Fatigue Results

Specimen Number	Average Concrete Compressive Strength [ksi]	Applied Stress Range [ksi]	Loading Rate [Hz]	Number of Cycles	Failure (F) or Runout (R)
1	5.9	8.7	10-20	12,803,000	F
2	7.0	4.4	10-20	30,053,000	R
3	6.4	5.8	10-20	12,251,908	R
4	8.2	5.8	10-20	20,000,000	R
5	6.4	7.25	10-20	31,401,000	R
6	8.4	8.7	10-20	30,001,000	R

2.3 Experimental Results

2.3.1 Observations and Measured Fatigue Life

All fatigue failures occurred at stress ranges above the existing AASHTO CAFL of 7ksi (48.3MPa), with the only complete fatigue failures occurring in Specimen 1 having an applied stress range of 8.7ksi (60MPa). Failure in Specimen 1, evidenced by a complete fracture of the four embedded studs, occurred after 12.8 million cycles. In Specimen 1, fractures originated at the base of the stud weld (see Figure 14(c)) and propagated into the beam flange leaving crater-like indentations in the flange as shown in Figure 14(a). This failure mode is similar to those observed in other push-out tests [4, 21, 22] and resulted in little-to-no damage to the concrete surrounding the stud. Specimen 2 (loaded at a stress range of 4.4ksi (30 MPa) and Specimen 5 (loaded at a stress range of 7.25ksi (50 MPa)) survived more than 30 million cycles prior to being declared runouts. Specimens 3 and 4 loaded at 5.8ksi (40 MPa) were also declared runouts after 12.25 million and 20 million cycles respectively. The resulting fatigue capacities for all six double-sided push-out specimens are provided in Table 2.

Slip between the concrete slab and steel beam was observed for all test specimens; however, for specimens loaded at stress ranges at or below 7.25ksi this slip was minor over then

entire cycle history. Figure 15 shows the average slip for each slab of specimens 5 and 1 (loaded at 7.25ksi and 8.7ksi respectively). Slip measurements for other specimens having lower applied stress ranges were similar to Specimen 5, and are presented in the Appendix. The slip values presented in Figure 15 are computed by averaging the two LVDTs on each beam flange, providing a single slip value for each slab. In Figure 15 a noticeable slip in slab 1 of Specimen 1 occurs near 3 million cycles, followed by an increase in the slip-per-cycle rate up to failure of the studs at 12.8 million cycles. Slip between the concrete slab and steel beam is an indication of stiffness loss and possible stud damage. Specimen 5, subjected to a lower applied stress range, experienced minimal slip (suggesting little stud damage) over the entire 30 million cycle loading. While slip measurements are helpful in estimating damage within the embedded studs over time, more detailed investigations are required to determine whether fatigue cracks actually exist.

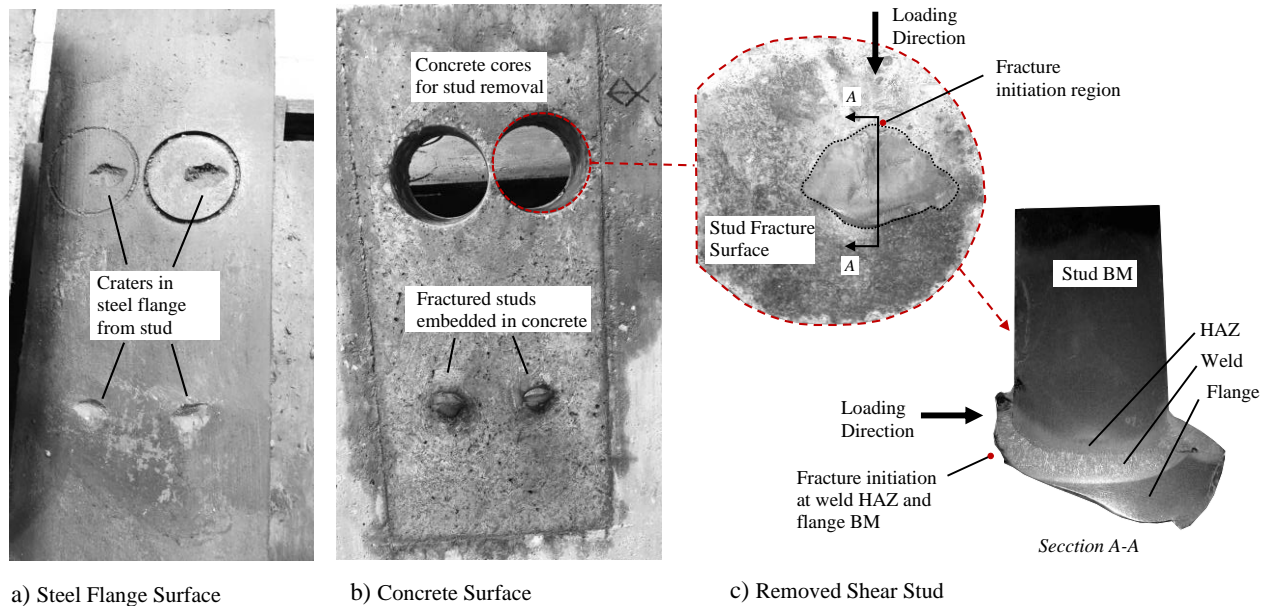


Figure 14 Shear stud failure mode observations for Specimen 1 (failure observed after 12,803,000 cycles at an applied stress range per stud of 8.7ksi)

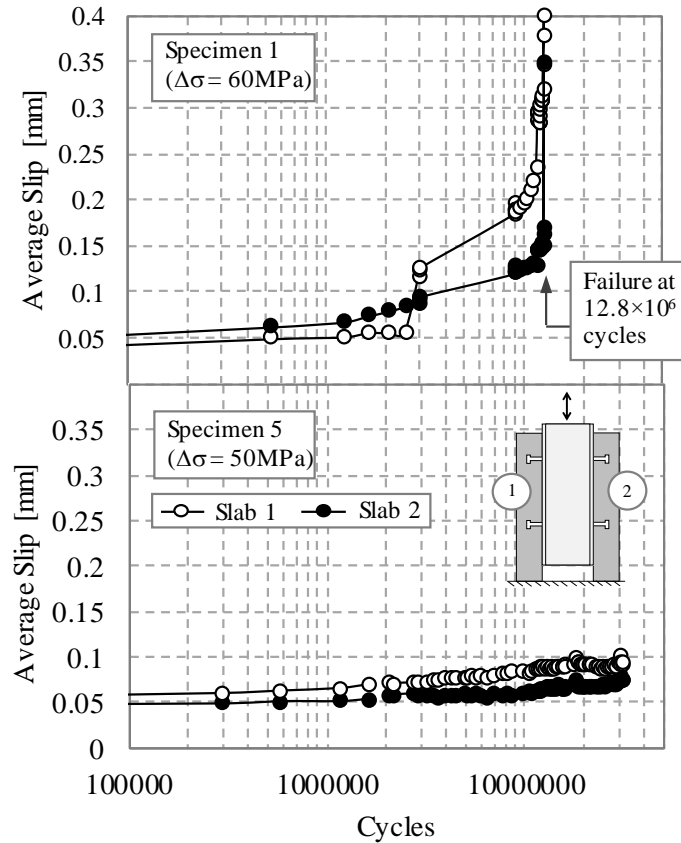


Figure 15 Average slip versus number of applied cycles for Specimens 1 and 5.

2.3.2 Stud Fatigue-Crack Investigations

Metallographic investigation and micro-hardness testing of stud cross-sections cored from completed tests indicate fatigue crack initiations within runout specimens and a critical fracture location near the stud-to-flange weld heat affected zone (HAZ). Stud samples cored from runout Specimens 2 and 5, were sectioned, polished with abrasive paper and diamond powder of increasing fineness (mirror polished to a surface roughness of $1\mu\text{m}$), and then surface etched with a Nitol solution (5ml HNO_3 per 100ml of ethanol). Figure 16 shows the polished stud cross-sections taken from the specimens with the various weld features highlighted, including the weld HAZ, base metals (BM), and fusion zone (FZ). Vickers micro-hardness

measurements (shown as contours in Figure 16) highlight material property changes (potential changes in material toughness) within the welded stud-to-flange zone and confirm the location of the HAZ, FZ, and BM. Stud sections taken from Specimen 2 (declared a runout after more than 30 million cycles at 4.4ksi (30.3 MPa)) show no indication of fatigue crack initiation (see Figure 16(a)); however, samples taken from Specimen 5 (declared a runout after more than 30 million cycles at 7.3ksi (50.3 MPa)) indicate fatigue cracks initiating near the weld HAZ at the stud-to-flange interface (see Figure 16(b)). The initiated fracture observed in Specimen 5 closely resembles the fracture path shown in Figure 14(c) for failure Specimen 1. These initiated fatigue cracks were present in all studs cored from Specimen 5.

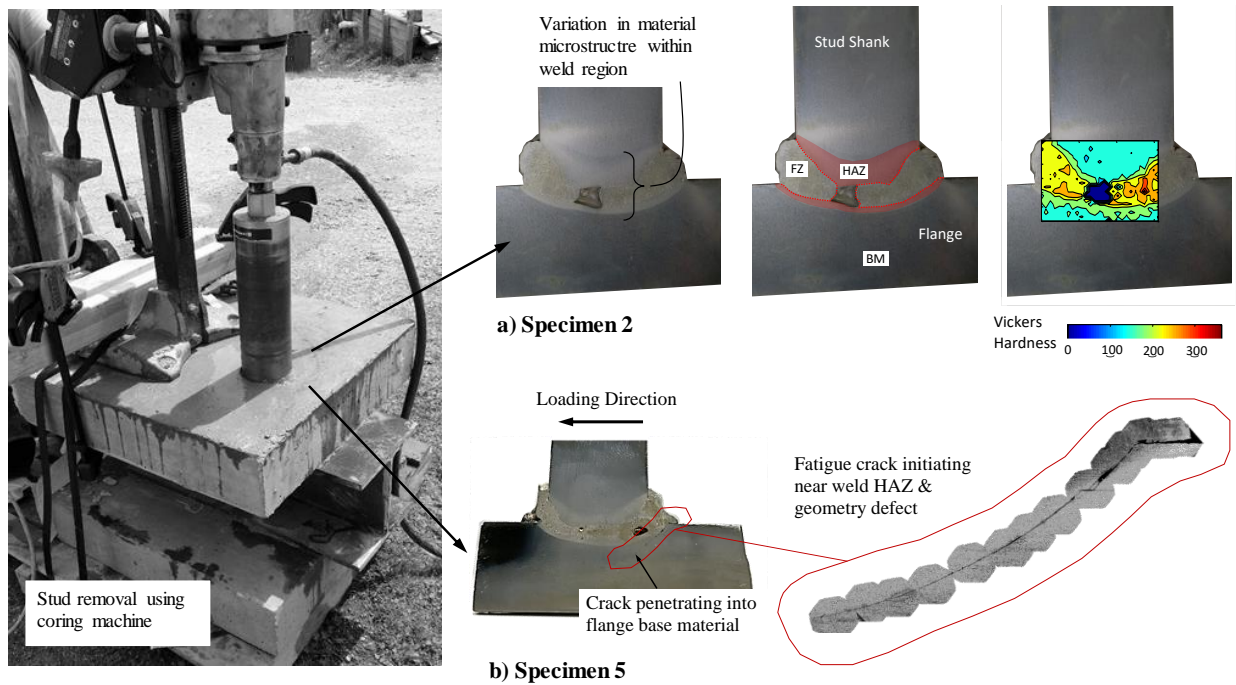


Figure 16 Fatigue crack investigation of polished stud sections from (a) Specimen 2 and (b) Specimen 5

2.4 Probabilistic Approach to Shear Stud Fatigue Capacity Evaluation

Scatter in fatigue test results is inevitable, and can provide uncertainty when predicting fatigue performance. When creating S-N curves for fatigue prediction, quantifying this uncertainty and maximizing the likelihood of predicting an experimental outcome is desired. In the regression analysis by Slutter and Fisher [4] (on which the current AASHTO stud capacity limits are based), S-N curves for shear stud fatigue capacity were created using a simplified least-squares fitting procedure incapable of quantifying the uncertainty in the experimental scatter. In this section, an alternative curve creation approach is proposed, wherein an advanced statistical method called maximum likelihood estimation (MLE) is used to create S-N curves that maximize the joint probability of predicting the observed experimental result. Several studies have successfully used MLE to define curve regressions for large data sets [23-26]. The following paragraphs describe a random fatigue limit model proposed by Pascual et al. [27] using the MLE method. The newly generated shear stud fatigue data is combined with existing data from the previous studies and analyzed using the random fatigue limit model. A new characteristic shear stud S-N curve considering data uncertainty and having a known confidence level is proposed.

2.4.1 Overview of MLE

The goal of the MLE approach is to identify a population (probability distribution) at each stress level that is most likely to have generated the experimental data. To achieve this, parameters for the population are chosen that maximize the joint probability of predicting failure at all points (or in other words, to maximize the likelihood of predicting failure at all points). This joint failure probability (or likelihood, L) is simply the product of every data-point failure probability, written as:

$$L = \prod_{i=1}^{nf} f_{N_i} \cdot \prod_{i=1}^{nr} R_{N_i} \quad (\text{Equation 13})$$

where f_{N_i} , R_{N_i} , n_f and n_r are the probability of predicting failure at an individual data point (i), the probability of predicting run-out at an individual data point (i), the total number of failure data-points, and the total number of run-out points respectively.

In this study, a nonlinear generalized reduced gradient optimization algorithm is used to maximize the likelihood given by the variable parameters in the regression model. In determining the individual failure probabilities required in Equation 13, a power-law relationship is assumed to appropriately represent the fatigue data [28, 29]. This power-law relationship is given in Equation 14,

$$\log_e N = \alpha + \beta \log_e (S - \gamma'), \quad (\text{Equation 14})$$

where N is the number of cycles to failure at a given applied stress range, S . Parameters α and β in Equation 14 are unknown parameters to be determined through MLE and γ' is the assumed CAFL, also to be determined through MLE. Note that for a confidence level of 50%, γ' in Equation 14 will be equal to the mean, μ_γ , of the CAFL distribution. For other curve confidence levels, γ' is taken as $\mu_\gamma - z^* \sigma_\gamma$ (shifting the CAFL location z^* standard deviations to the left of the mean). Equation 15 presents the regression relationship that can be used for confidence levels other than the mean, and Figure 17 depicts the MLE based model assuming the above power-law relationship and considering normally distributed data at each stress-range level.

$$\log_e N = \alpha + \beta \log_e (S - (\mu_\gamma - z^* \sigma_\gamma)) - z^* \sigma \quad (\text{Equation 15})$$

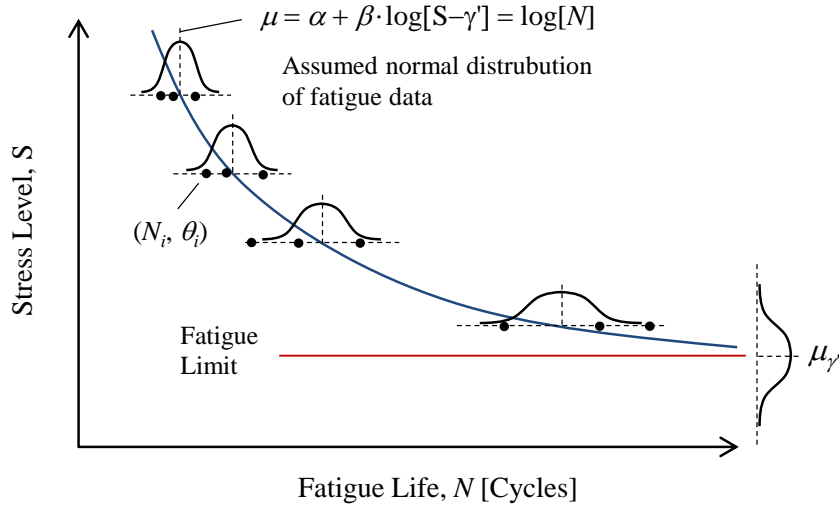


Figure 17 Fatigue-life curve representation through MLE fitting

The probability of having failure at each data point (N_i, S_i) in Figure 17, given a specific CAFL value (γ') and assuming the data at each stress-range level as normally distributed, is given by the conditional probability density function shown in Equation 16.

$$f_{N_i|\gamma'} = PDF_{N_i, S_i|\gamma'} = \left(\frac{1}{\sqrt{2\pi} \cdot \sigma} \right) \exp\left(\frac{-1}{2\sigma^2} \cdot [N_i - \alpha - \beta \log(S_i - \gamma')]^2 \right) \quad (\text{Equation 16})$$

Because $f_{N_i|\gamma'}$ assumes a given γ' , the probability that γ' exists ($f_{\gamma'}$) must also be determined (see Equation 17). The resulting probability of predicting failure at N_i is the marginal probability density function representing the joint probability between $f_{N_i|\gamma'}$ and $f_{\gamma'}$ as given in Equation 18.

$$f_{\gamma'} = \left(\frac{1}{\sqrt{2\pi} \cdot \sigma_{\gamma'}} \right) \exp\left(\frac{-1}{2\sigma_{\gamma'}^2} \cdot [\gamma' - \mu_{\gamma}]^2 \right) \quad (\text{Equation 17})$$

$$f_{N_i} = PDF_{N_i} = \int_0^{S_i} f_{N_i|\gamma'} \cdot f_{\gamma'} \cdot d\gamma' \quad (\text{Equation 18})$$

2.4.2 Influence of Run-Outs on CAFL

Many S-N curves often only consider failure test results in identifying regression parameters, neglecting run-out test results and their potential influence on curve features such as the CAFL. At certain low stress levels, such as those considered in this study, the possibility exists for run-out test results to occur. MLE allows these run-out test results to influence the S-N curve through the population cumulative distribution function, since run-out simply indicates the absence of failure. In the case of run-outs, the probability of predicting run-out given an assumed CAFL (γ') is given by:

$$R_{N_i|\gamma'} = 1 - CDF_{N_i, S_i|\gamma'} \quad (\text{Equation 19})$$

where $CDF_{N_i, S_i|\gamma'}$ is the cumulative density function assuming γ' . The resulting probability of run-out, R_{N_i} , is the marginal probability density function between Equation 19 and Equation 17, given by Equation 20.

$$R_{N_i} = \int_0^{S_i} (1 - CDF_{N_i, S_i|\gamma'}) \cdot f_{\gamma'} d\gamma' \quad (\text{Equation 20})$$

2.4.3 Shear Stud Fatigue Dataset and Analysis using MLE

The complete fatigue data set considered in this study is presented in Table A- 1 of Appendix A, and consists of the six fatigue results described earlier and 100 fatigue results from existing comparable testing found in the literature. The 100 fatigue results taken from the literature were from a total of seven shear stud fatigue studies conducted between 1959 and 1988 [3, 11, 4, 5, 21, 12, 13]. All existing fatigue data presented in Table A- 1 were selected based on four criteria, including: 1) a stud shank diameter of 19mm (3/4 in.); 2) constant amplitude

loading; 3) unidirectional loading (no reversed cycles), and 4) failure occurring in the stud shank or weld (i.e. no concrete crushing failures). For conservancy, test results from reversed cycle loading were not included, as they typically result in higher fatigue capacities due to the reduced applied mean stress [4]. Fatigue results from both single-sided and double-sided push-out tests were considered. Additional test data for 7/8” studs from more recent studies (conducted between 2000 and 2014) are used in comparisons (see Table A- 2 in Appendix A) [4, 30, 19, 22, 31, 10].

Analysis of the fatigue dataset suggests that the existing AASHTO CAFL is reasonable, but indicates higher fatigue capacity within the finite-life region for stress-ranges over 17ksi (117MPa). Equation 21 presents the stud fatigue capacity equation resulting from the MLE analysis, with the optimized parameters of α , β , μ_γ , σ , and σ_γ being 17.26, -2.09, 6.5ksi, 1.45, and 1.21ksi respectively. Note that the stress range parameter in Equation 21 is based on units of ksi. The resulting distribution for the CAFL is characterized by a standard deviation of 1.21ksi. In Equation 21, the mean CAFL value of 6.5ksi (44.8MPa) is near the existing value of 7ksi (48MPa) for constant amplitude fatigue. Analysis of the data considered uniformly distributed data at each stress-range level, and a mean confidence level (50%) based on the inherent conservancies in fatigue data resulting from push-out specimens [4, 17, 10].

$$\log_e N = 17.26 - 2.09 \log_e (S - 6.5) \quad (\text{Equation 21})$$

Figure 18 shows the resulting regression from the MLE analysis. For comparison, the current AASHTO shear stud S-N curve is also plotted along with the considered fatigue data-set.

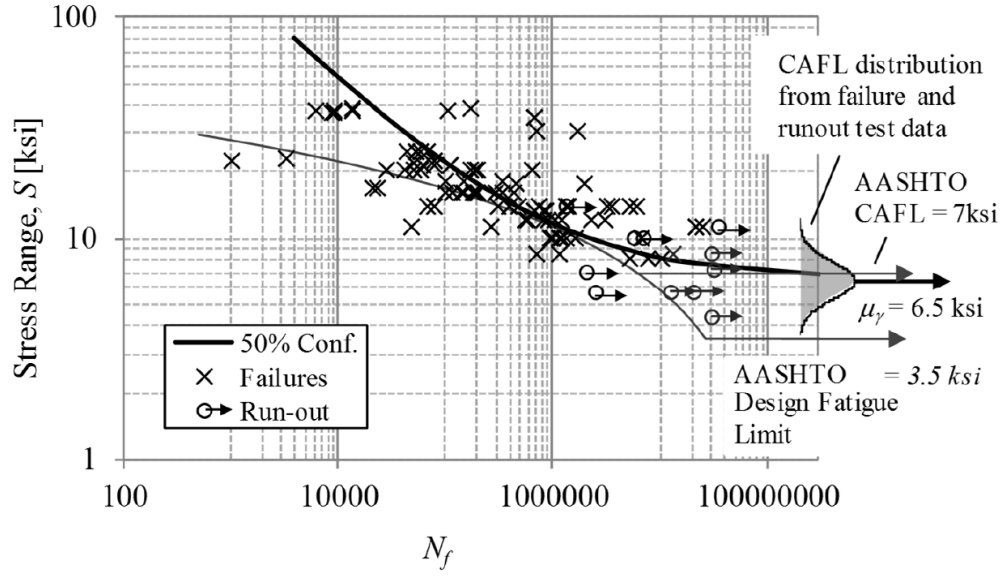


Figure 18 Comparison of AASHTO S-N curve and MLE regression

2.5 Proposed Design S-N Curve for Predicting Shear Stud Fatigue Capacity

Given similarities in form between the MLE S-N curve and the S-N curves for various steel bridge fatigue details provided in AASHTO, a simplification of Equation 21 is proposed to provide consistency in design. In AASHTO [1], the design load-induced fatigue resistance for bridge details (excepting fatigue of the stud) takes the form:

$$(\Delta F)_n = \left(\frac{A}{N} \right)^{\frac{1}{m}} \geq (\Delta F)_{TH} \quad (\text{Equation 22})$$

where m and A are constants representing the slope and intercept of the fatigue S-N curve. In Equation 22, $(\Delta F)_{TH}$ is the CAFL, and $(\Delta F)_n$ is the allowable stress range. To adapt Equation 21 to the form provided in Equation 22, a bi-linear design S-N curve is fit to the power-law relationship determined through MLE using the CAFL asymptote and approximate tangent at 15ksi (103MPa). This simplification provides an avenue for consistency between shear stud fatigue capacities and standard fatigue detail capacity forms. Table 3 presents the proposed detail category description, including the proposed S-N curve constant (A), slope (m), threshold

value ($CAFL$ or $(\Delta F)_{TH}$), description of the potential crack initiation point, and an illustrative example of potential damage.

Table 3 Proposed detail category description for shear stud fatigue capacity

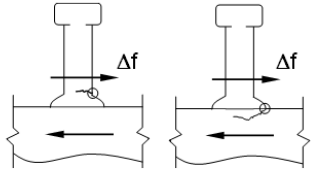
Description	Category	Constant A (ksi ⁴)	Threshold $(\Delta F)_{TH}$ ksi	Potential Crack Initiation Point	Illustrative Examples
9.2 Connection weld or shank of stud-type shear connector attached by fillet or automatic stud welding subjected to shear loading	D' [m = 4]	150×10^8	6.5	Toe of stud-to-flange welds, propagating through the stud shank or into the flange base metal	

Figure 19(a) plots the proposed design S-N curve along with the MLE regression and fatigue data, and Figure 19(b) compares the proposed bi-linear design S-N curve with the current AASHTO fatigue detail categories. Note in Figure 19(b), that the proposed stud fatigue design S-N curve indicates a lower fatigue capacity than the curve for fracture in the base metal outside the stud weld, but a higher capacity than the current AASHTO stud fatigue limit. While the proposed design S-N curve is derived from the MLE analysis on 3/4" stud fatigue tests, data from other fatigue tests on 1/2", 7/8", and 1-1/4" studs fits the general trend of the curve and fall within the scatter of the 3/4" results. For comparison, Figure 19(c) is provided to show the proposed design S-N curve with data from 3/4", 1/2", 7/8", and 1-1/4" stud fatigue tests (see again Appendix A for the stud fatigue values considered).

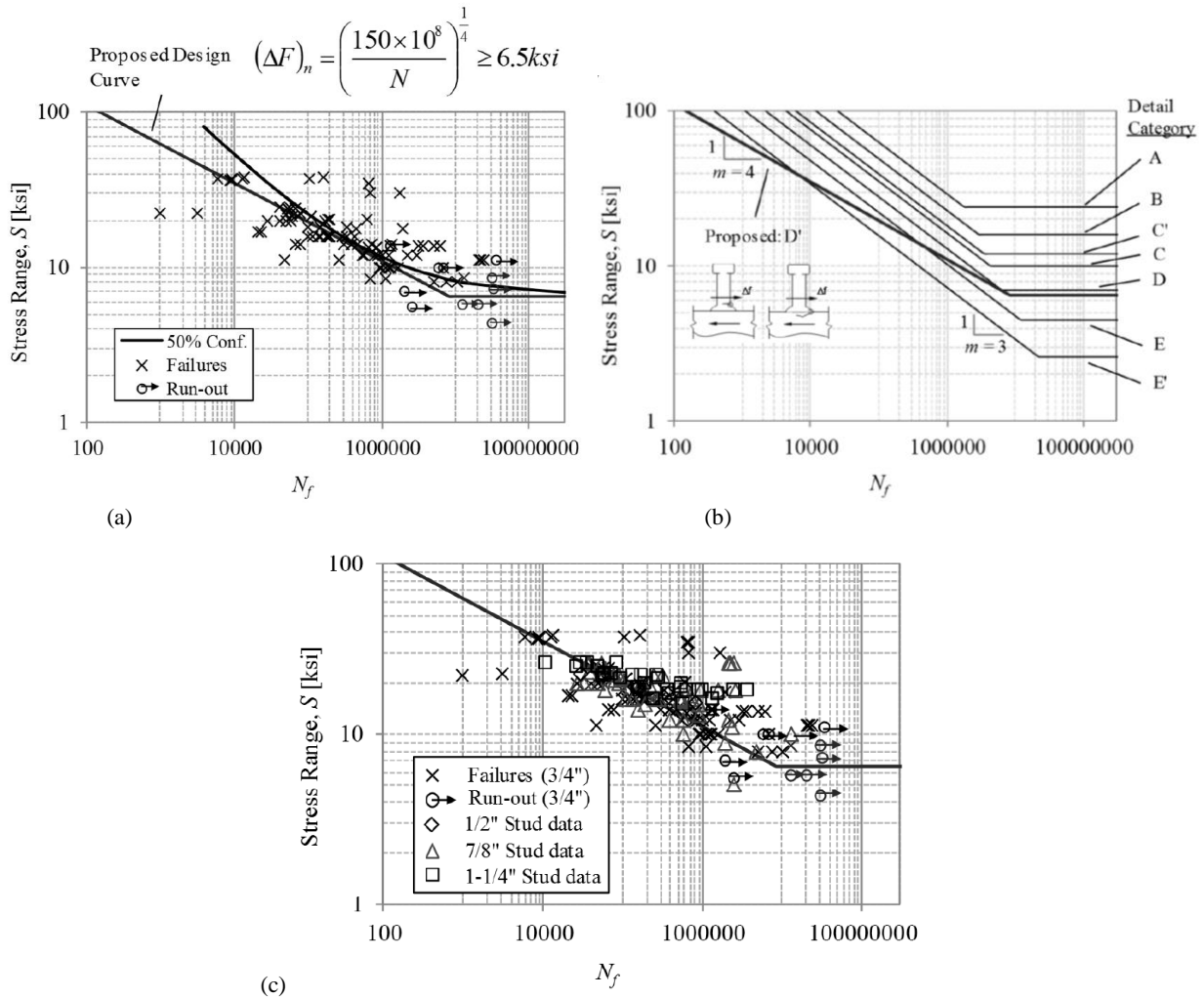


Figure 19 (a) Comparison of proposed design S-N curve, MLE regression, fatigue data, and current AASHTO curve; (b) Comparison of proposed design S-N curve and existing AASHTO fatigue details; (c) comparison of proposed curve with fatigue data from additional stud

2.6 Summary and Conclusions

In this chapter, six composite push-out specimens were fatigue tested under repeated cyclic loads at stress ranges varying between 4.4ksi and 8.7ksi (30MPa and 60MPa). These composite push-out specimens represent a conservative estimation of stud fatigue damage as the adhesion and friction at the steel-concrete interface were inhibited by greasing of the steel flanges prior to concrete casting. Measured fatigue life from the six specimens were combined with existing

shear stud fatigue data sets in the literature, and analyzed using a probabilistic method called maximum likelihood estimation. Results from the six fatigue tests and analysis of the new and existing fatigue data provide the following conclusions:

- 1) The current AASHTO CAFL for headed shear studs provides a reasonable estimation of fatigue capacity. Analysis of existing data along with the additional high-cycle fatigue test results suggests a CAFL of 6.5ksi (44.8MPa) which is near the assumed value of 7ksi (48 MPa).
- 2) The current AASHTO S-N curve for finite life of the shear stud underestimates fatigue capacity and is not representative of the larger considered fatigue dataset. An alternative design S-N curve of similar form to the existing AASHTO detail categories (log-log form)

is proposed. The proposed curve of the form $(\Delta F)_n = \left(\frac{A}{N}\right)^{\frac{1}{m}} \geq (\Delta F)_{TH}$ has an $m=4$ and $A=150 \times 10^8$ and provides a known level of confidence in the estimated fatigue capacity (based on the MLE analysis with a confidence level of 50%) while providing a unification in the fatigue design procedure. Note that stress range capacities provided in the proposed equation were derived using imperial units of ksi.

Chapter 3: ANALYSIS OF SHEAR DEMANDS NEAR THE STEEL-CONCRETE INTERFACE IN COMPOSITE BRIDGE GIRDERS HAVING VARIED STUD PITCH, GIRDER DEPTH, AND SPAN LENGTH

3.1 Background

The center-to-center spacing, or pitch, between headed sheer studs in the AASHTO specification is currently limited to 24 inches [1]. This 24-inch spacing limit first appeared in the 4th edition of AASHTO specification in 1944, without commentary or citation; however, research suggests the 24-inch limit is largely based on composite beam investigations conducted in the 1940s and 1950s expressing concerns over deck separation at larger stud spacings [32, 33, 8]. Research since the 1950s has shown little evidence of deck separation regardless of the shear stud spacing.

Non-welded shear connectors in concrete girders are allowed to be spaced up to 48 inches, and additional steel girder research into welded shear studs at larger spacings indicates that an increase in the pitch limit from 24 to 48 inches is justified [8, 9]. In one study by [8], experiments showed little-to-no effect of increased stud spacing on stud fatigue resistance while maintaining full composite action. In [8], shear stud clusters were spaced up to 48 inches. Another study by [34] tested an increase in stud spacing by cluster spacing studs on one side of a half-scale beam at 24 inches and cluster spacing the other half of the beam at 48 inches. Test results in [34] showed that full composite action could be achieved under full service load with no indication of stiffness reduction after 2,000,000 fatigue cycles.

While these studies suggest that increases in the maximum stud spacing can maintain full composite action under service loads, the fatigue investigations (number of cycles applied) are fairly limited and neglect additional factors such as effects of alternative span lengths, girder depths, and the effect of stud of clustering on individual stud demands.

Groups of clustered studs may experience shear demands that are different from those assumed in the current AASHTO shear flow equation. A 2003 study by Issa et. al. [35] investigated the spacing effects on clustered pockets of studs as well as the number of studs per pocket and found that the increase in load capacity per stud was not proportional to the number of studs in the shear pocket. This testing involved static loading rather than fatigue loading and indicated that the shear distribution across stud clusters is not linear. More investigation is needed to understand the effects of stud clustering on shear distribution through the studs at the steel-concrete interface if larger stud spacings are to be considered.

This chapter expands upon the previous research of the Turner Fairbanks Highway Research Center [10] through a parametric analytical investigation of shear demands near the steel-concrete interface in composite bridge girders. In the parametric investigation, the effects of varied stud pitch, girder depth, and girder span on resulting stud demands are considered. The following section describes the analytical parametric investigation.

3.3 Parametric Investigation

3.3.1 Prototype Bridge Designs and Stud Spacing Variations

A total of 24 detailed finite element analyses, representing 2 different girder spans, 3 different girder depths, and 4 different shear stud spacings are performed. The considered span lengths are 100 and 200 feet representing short and medium-to-long span bridges. The three different girder depths are considered as a ratio of the span length (L) and are $L/30$ for shallow girder depths, $L/25$ for standard girder depths, and $L/20$ for deep girder depths (see Figure 20). The 4 different stud pitch values considered are 12, 24, 36, and 48 inches from center-line to center-line of stud clusters as shown in Figure 20. In order to keep the overall shear resistance constant between girders of similar span and depth, the number of shear studs per length was

chosen to remain the same. This was accomplished by grouping studs at larger spacing values (i.e. having a single row of studs at 12 inches, two rows at 24 inches, 3 rows at 36 inches, and 4 rows at 48 inches). Table 4 shows the analysis matrix of the 36 simulations performed. For all analysis configurations, the girder and deck were designed in accordance with AASHTO specifications [1], excepting the use of load distribution factors which were kept constant through all designs for simplicity. A sample composite girder design following the AASHTO specification is provided in Appendix F.

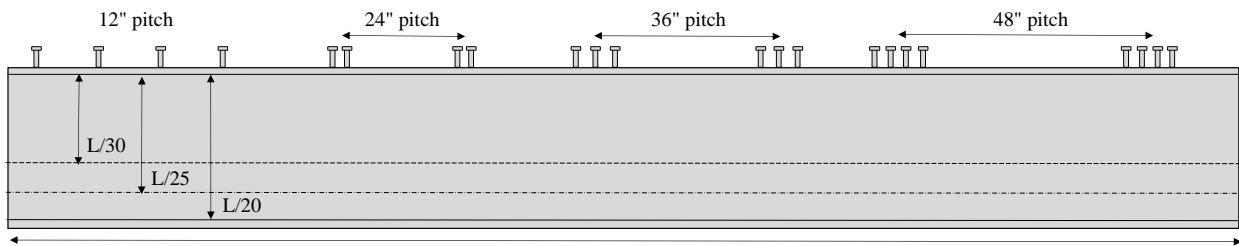


Figure 20 Details of pitch and girder depth variation

Table 4 Analysis Matrix for Parametric Investigation

Girder	Span (ft)	Depth (in)	Pitch (in)	Compression Flange Width (in)	Compression Flange Thickness (in)	Tension Flange Width (in)	Tension Flange Thickness (in)	Web Thickness (in)	Deck Thickness (in)	Deck Width (ft)
1A	100	40	12	16	1.5	16	1.5	0.63	10	9
1B	100	40	24	16	1.5	16	1.5	0.63	10	9
1C	100	40	36	16	1.5	16	1.5	0.63	10	9
1D	100	40	48	16	1.5	16	1.5	1.63	10	9
2A	100	48	12	16	1.5	16	1.5	0.63	10	9
2B	100	48	24	16	1.5	16	1.5	2.63	10	9
2C	100	48	36	16	1.5	16	1.5	0.63	10	9
2D	100	48	48	16	1.5	16	1.5	3.63	10	9
3A	100	60	12	16	1.5	16	1.5	0.63	10	9
3B	100	60	24	16	1.5	16	1.5	4.63	10	9
3C	100	60	36	16	1.5	16	1.5	0.63	10	9
3D	100	60	48	16	1.5	16	1.5	5.63	10	9
4A	200	80	12	20	1.75	20	1.75	1.00	10	9
4B	200	80	24	20	1.75	20	1.75	1.00	10	9
4C	200	80	36	20	1.75	20	1.75	1.00	10	9
4D	200	80	48	20	1.75	20	1.75	1.00	10	9
5A	200	96	12	20	1.75	20	1.75	1.00	10	9
5B	200	96	24	20	1.75	20	1.75	1.00	10	9
5C	200	96	36	20	1.75	20	1.75	1.00	10	9
5D	200	96	48	20	1.75	20	1.75	1.00	10	9
6A	200	120	12	20	1.75	20	1.75	1.00	10	9
6B	200	120	24	20	1.75	20	1.75	1.00	10	9
6C	200	120	36	20	1.75	20	1.75	1.00	10	9
6D	200	120	48	20	1.75	20	1.75	1.00	10	9

3.2.3 Modelling Methods

The following sections describe the materials, elements, boundary conditions, mesh, beam-to-slab connection, and loading. Note that all modeling techniques described herein are similar to other validated techniques used by [36] for simulating composite beam behavior.

3.2.3.1 Materials, Elements, Boundary Conditions, and Meshing

Simplified elastic-plastic steel and concrete properties were used in all simulations within the parametric study. Simplified material properties were used because anticipated service loadings, which drive fatigue damage, are often well within the elastic range of both the steel and concrete material behaviors. Concrete was modelled assuming a Young's modulus of 5,330ksi, corresponding to a compressive strength of 8.75ksi, and a Poisson's ratio of 0.15. The chosen concrete values correspond to measured material strengths from composite beams used in full scale testing for model validation. All steel is assumed as A709-Gr 50 steel having a Young's modulus of 29,000ksi, yield strength of 60ksi, and Poisson's ratio of 0.3.

All geometry for the composite girders (the concrete deck, steel girder, and stiffeners) are modeled using four-node linear shell elements. Shell elements were chosen for this study to allow detailed localized stress and strain data to be gathered near the stud-to-flange connections while maintaining reasonable computational cost.

Simply-supported boundary conditions creating positive moments throughout the entire girder length are assumed for all beam designs modeled in the parametric study. Figure 21 shows a representative composite girder with the applied boundary conditions. In Figure 21, boundary constraints create a simply-supported condition as well as provide lateral support from transverse cross-frames which are typically present in bridge construction. To prevent localized

stress concentrations near support locations, all bearing portions of the girder are rigidly constrained to a single node where the boundary conditions are applied (see Figure 21).

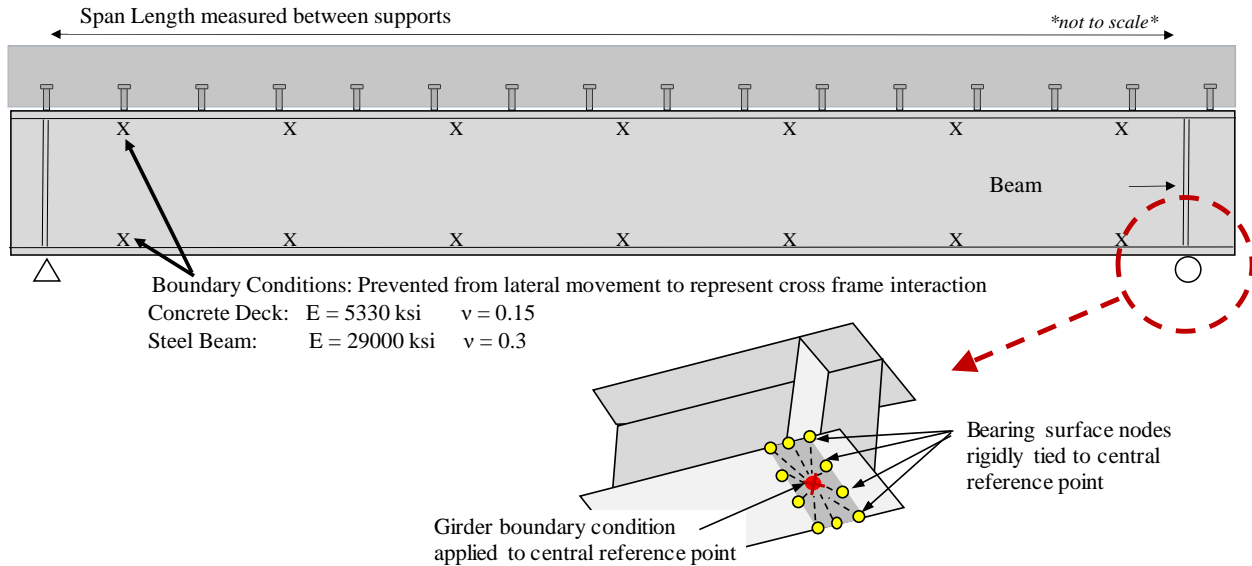


Figure 21 Girder views showing typical boundary conditions and support constraints.

In finite element analysis, computational requirements and accuracy are both affected by the chosen mesh size. To maintain reasonable accuracy while limiting computational cost for the large girders analyzed, mesh sizes considered were between 4 and 5 inches for the beam web and bottom flange as shown in Figure 22. Note that the circular partitions representing shear stud cross sections shown in Figure 22 required a more refined mesh size of approximately 0.5 inches. The refined mesh near the shear stud location provides a higher density of elements for capturing stress gradient variations within the regions where the shear forces are evaluated.

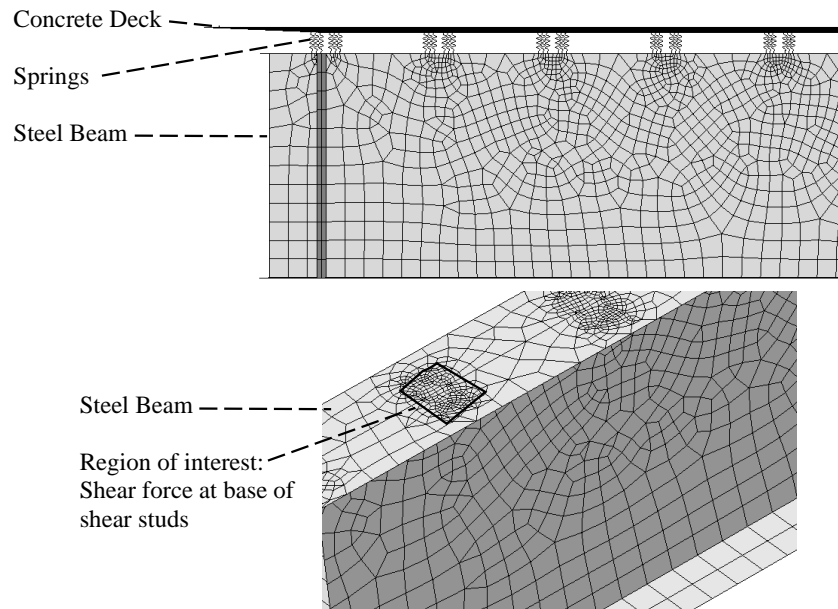


Figure 22 Typical girder finite element model mesh

3.2.3.2 Composite Slab Connection Modeling

Similar to methods used by Barth and Wu [36], the shear studs connecting the steel flange to the concrete deck are modeled with three spring connections for each shear stud as shown in Figure 23. These three springs provide a representative stud stiffness for simulating axial and shear behavior in the X, Y, and Z local directions. For each discrete steel-concrete connection, the top and bottom of the springs are connected to the center of a circular region that simulates the shear stud cross-sectional area as shown in Figure 23. The circular partition is rigidly tied to each of the stud springs to eliminate localized nodal stress concentrations and simulate the distribution of shear force over the stud cross-sectional area, which typically occurs when a shear stud is embedded in concrete. Given that the test results from Chapter 2 showed no crushing of concrete during fatigue loading (meaning limited stud flexural deformation), and given the shell-element slab offset from the girder flange, the lateral stiffness of each shear stud is set at a value of 1×10^6 ksi. This increased stud stiffness value helps capture behavior of the

localized region of stud deformation within the model (as the studs are only allowed to deform over a small distance at the steel-concrete interface).

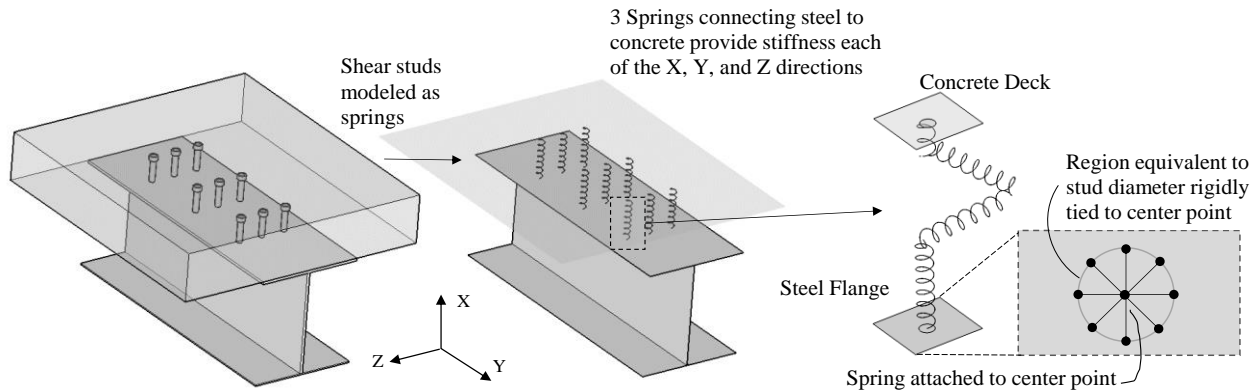


Figure 23 Simulated shear studs composed of multiple springs with stiffness values in the X, Y, and Z directions.

In addition to the shear stud connection between the steel flange and concrete deck, composite beams often experience friction between the concrete slab and the steel girder which is difficult to quantify. This friction at the steel-concrete interface was not simulated in the parametric study, making the resulting stud demand analyses somewhat conservative. Note that neglecting friction and adhesion between the steel and concrete is standard practice for composite beam fatigue experiments and simulations.

To simulate slab contact and prevent the shell element slab from moving relative to the girder flange, additional multi-point constraints were added to each girder end where studs were not present. Figure 24 shows the multi-point constraints added to the girder ends to prevent relative vertical movement (simulating slab contact) between the concrete slab and girder top flange.

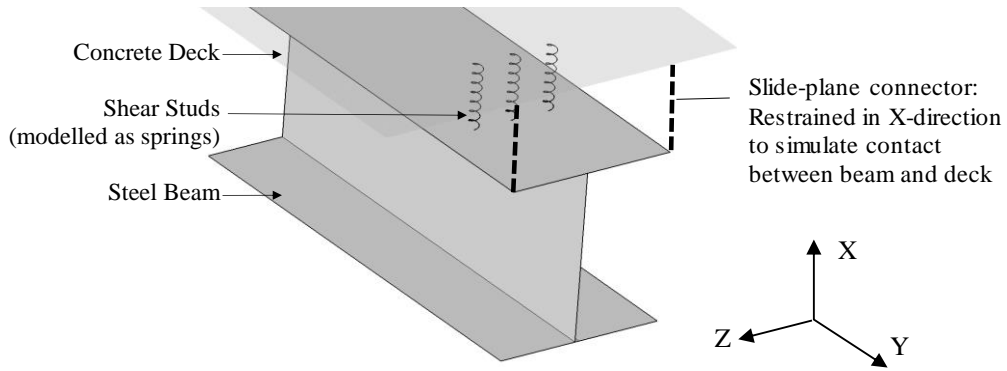


Figure 24 shows slide-plane connections between the steel and concrete

3.2.3.3. Bridge Loading

All girders were loaded by the AASHTO fatigue truck axle weights “driving” the length of the girder span. These moving axle loads were simulated using discrete concentrated forces applied in sequential patterns. The AASHTO fatigue truck consists of a front-axle load of 8 kips, followed by two axles each having a load of 32 kips (see Figure 25) [1]. In bridge design, an impact factor and a fatigue load factor are typically applied to the traffic load shown in Figure 25 to account for specific design conditions; however, for the purposes of this study, all loads remained un-factored for simplicity of comparison with codified procedures. Because each simulation involves only one girder, one side (half of each axle) was used to represent the load of one set of tires being distributed to the beam (assuming load distribution to adjacent girders). The same moving load from the AASHTO fatigue truck were applied to each of the 36 models in this study.

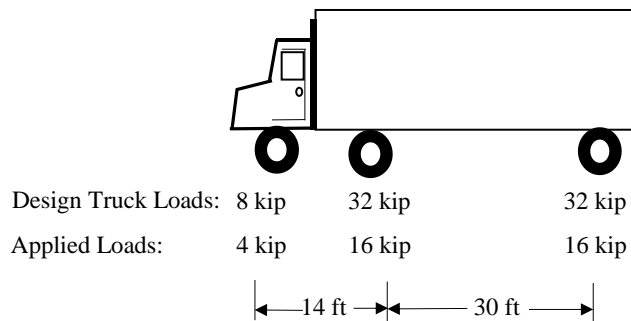


Figure 25 AASHTO fatigue truck characteristics and applied loads [1]

The simulation of a moving load across the girder slab was created by using a series of concentrated forces with associated amplitudes evenly distributed along the span of the beam. Discrete concentrated loads were placed at 6 inch increments along the girder slab centerline and activated/deactivated in sequence. An amplitude was created for each discrete load location such that ramping up of the $i+1$ th load coincides with the ramping down of the i th load, thus “moving” the load across the beam as shown in Figure 26.

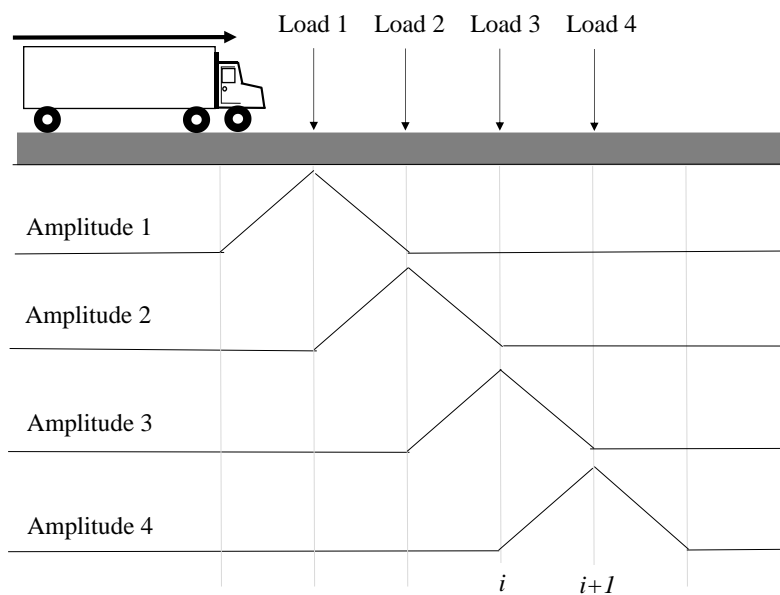


Figure 26 Loads and corresponding amplitude layout

3.2 Validation of Modeling Techniques from Full-Scale Girder Tests

Techniques used to model all girders in the parametric study were first verified using results from three full-scale composite girder tests performed at the Turner Fairbanks Highway Research Center (TFHRC) and two full-scale composite girder tests performed at the University of Nebraska. Global composite behavior from the experiments and simulations are compared to gain confidence in the simulation techniques. The following sections describe the experimental tests used for verification as well as the finite element techniques used to simulate composite

behavior. Note that the truck fatigue loading used in the parametric investigation is well within the elastic range of the composite girders and therefore only the elastic behavior of the composite girder test results is used to validate modelling techniques.

3.2.1 Description of Tests performed at TFHRC

Researchers at the TFHRC performed three large scale composite beam tests and provided detailed global behavior information for the purpose of validating the finite element modelling techniques in this study. These tests involved static loading of three individual simply supported composite beams (named TFHRC 1, TFHRC 2, and TFHRC 3 as shown in Table 5). Each beam consisted of a 30 foot rolled W27×84 A992 Gr50 steel beam with a 48” wide by 8” deep reinforced concrete deck. In the TFHRC testing, each concrete deck was pre-cast with pockets to allow for later grouting of the shear studs (investigating accelerated bridge construction techniques). All shear studs were 7/8” in diameter with each test having a different pitch as shown in Figure 27. Table 5 shows the shear stud pitch and quantity information provided by the TFHRC researchers. Figure 28 shows plan and elevation views of test TFHRC 1 with additional detailed test drawings provided in Appendix E.

Table 5. Stud Pitch for TFHRC tests

Test	Studs Per Cluster	Pitch of Cluster (in)
TFHRC 1	1	12
TFHRC 2	2	24
TFHRC 3	3	36

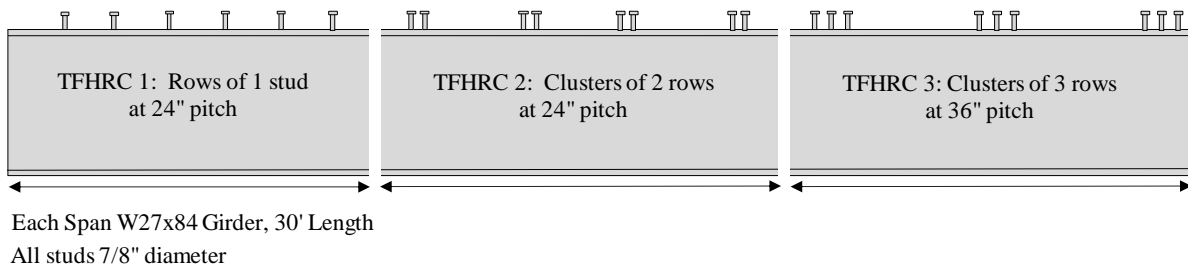


Figure 27 Schematic of cluster and pitch arrangement in TFHRC tests

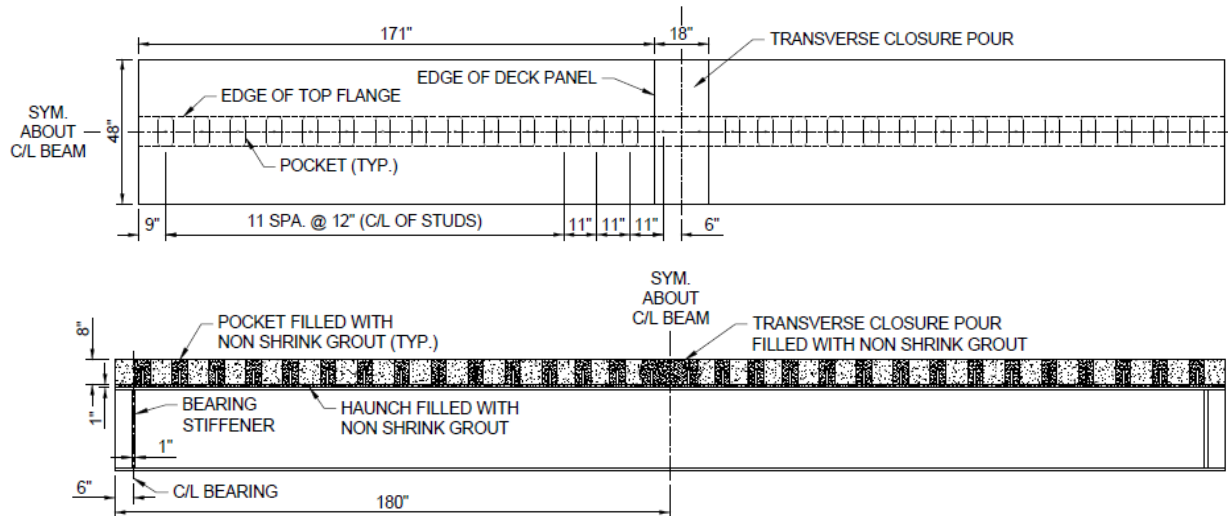


Figure 28 Plan and elevation views of test TRHRC 1

The deck of each TFHRC girder test was loaded with two hydraulic actuators (having 17 in² bearing plates to avoid local slab crushing) located 3 feet from the girder center line in each direction. All loads were applied through spherical bearings to maintain vertical loading during girder deflections. The experimental set up showing load locations and boundary conditions for test TFHRC 1 is shown in Figure 29. Note that the same test setup was used for tests TFHRC 2 and TFHRC 3.

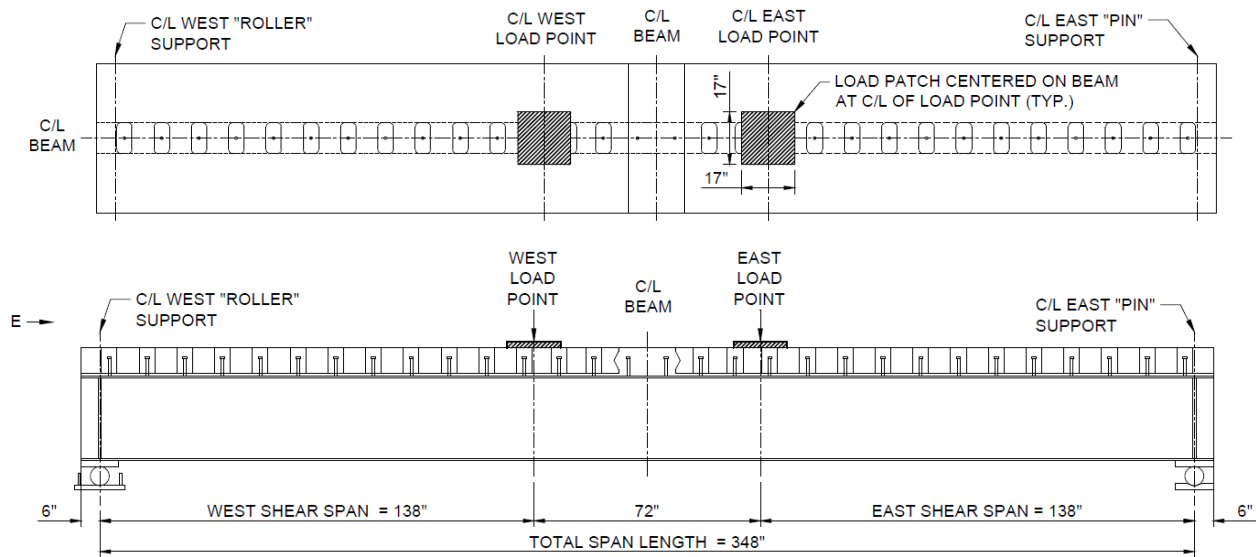


Figure 29 Static load test setup for TFHRC 1 (plan and elevation views)

3.2.2 Description of Tests performed at University of Nebraska

In addition to the three composite beam tests at the TFHRC, results from two composite steel plate girders fabricated from A709 Gr70 steel tested at the University of Nebraska were used for model validation [37]. Results from the additional two composite beam tests were used to validate finite element modelling techniques to conventionally poured concrete decks as used in the parametric study. Figure 30 shows the elevation view, including dimensions, of the Nebraska specimens. As shown in Figure 30, each Nebraska specimen consists of a 42 foot simply supported girder having bearing stiffeners and intermediate stiffeners with lateral bracing for stability. Differences between the two Nebraska tests include the considered stud configurations and deck geometry. University of Nebraska Test 1 (named UN1) contained 80 pairs of $\frac{3}{4}$ " diameter shear studs at a pitch of 6" while test 2 (UN2) contained 60 pairs of $\frac{3}{4}$ " diameter shear studs at a pitch of 7". According to design documents [37], test UN1 and UN2 have deck widths of 60 inches and 86 inches respectively, with both concrete decks reinforced and cast horizontally in place over the studs. The Nebraska tests were both loaded vertically by a hydraulic actuator reacting against a single spreader beam located at the centerline of the concrete deck.

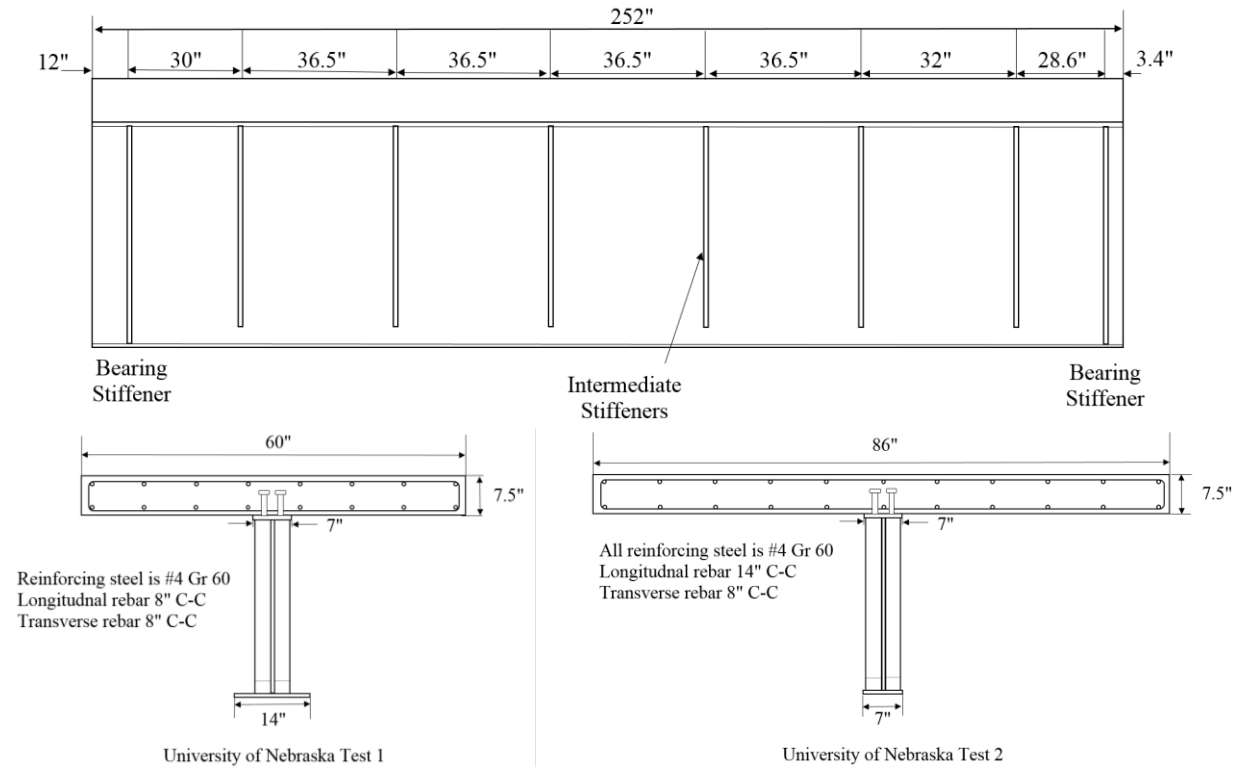


Figure 30 shows elevation view of beam, which is the same for UN1 and UN2, and end views of UN1 and UN2 showing the differences in deck and steel

3.2.4 Model Validation using TFHRC Tests with Pocketed Studs

Comparison between the TFHRC global test results and model simulations are shown in Figure 31. From Figure 31, a slight deviation is noticed between the analyses and experimental measurements, suggesting that the modeling techniques failed to accurately capture the composite girder stiffness. Discrepancies between the measured elastic deflections and those anticipated through analysis may be due to the use of grout and pocketed pre-cast deck materials having different strengths than assumed in the analyses. Note that in the TFHRC testing, high-density higher strength grout was used to seal the precast deck shear pockets and “seat” the deck on the girder flange. Additionally, it should be noted that the resulting measured force-deflection curves shown in Figure 31 do not match the typical elastic/plastic composite beam behavior from

other studies [REF] potentially due to the pre-cast deck composite construction. Additional validation testing from the cast-in-place Nebraska specimens may provide more insight into the accuracy of the modeling techniques for conventionally fabricated composite girders.

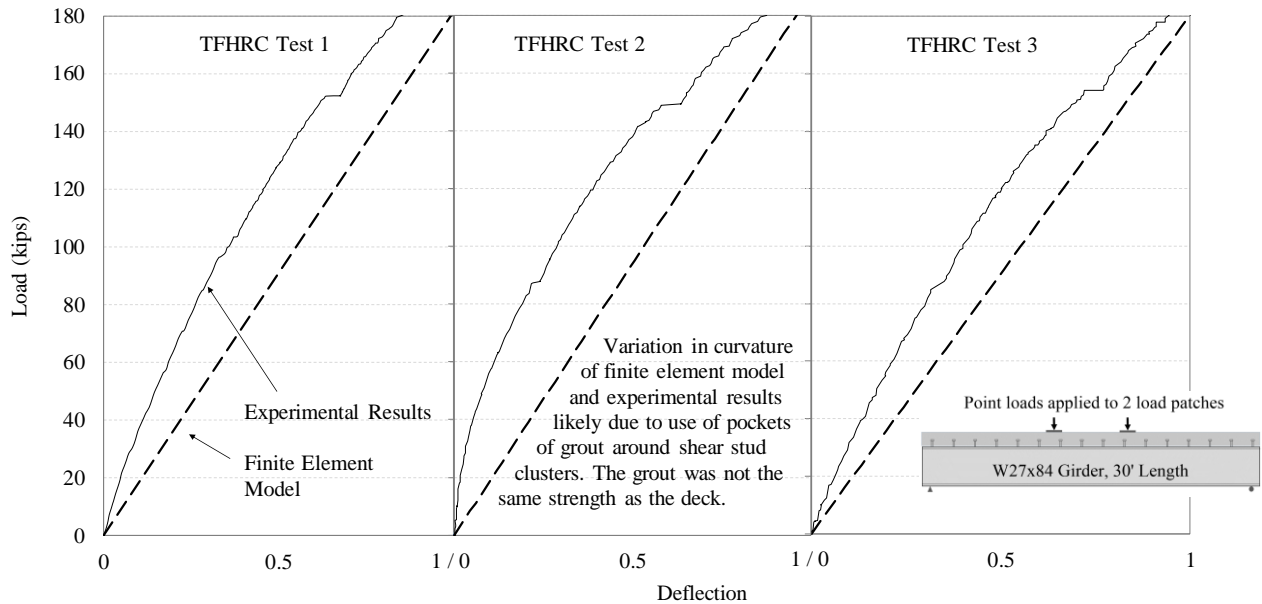


Figure 31 shows load v. deflection results from TFHRC tests and finite element model tests

3.2.4 Model Validation using University of Nebraska Composite Beam Tests

Figure 32 compares the University of Nebraska composite girder test results and simulated response. From Figure 32, the modeling techniques described were able to reasonably capture the global load-deflection behavior measured from the two full-scale experiments. Note that in test UN1 and UN2, the concrete slab was cast-in-place around the welded shear studs similar to conventional construction of composite beams. The difference between the maximum deflection of the finite element models and the experimental model were similar (0.18 inches and 0.25 inches for tests UN1 and UN2 respectively). The similarities in global response between the experiment and simulations indicate that the modelling techniques, including: materials, boundary conditions, element types, and spring stiffnesses, are adequate for capturing the

composite girder behavior within the elastic range considered for the fatigue demand investigations herein.

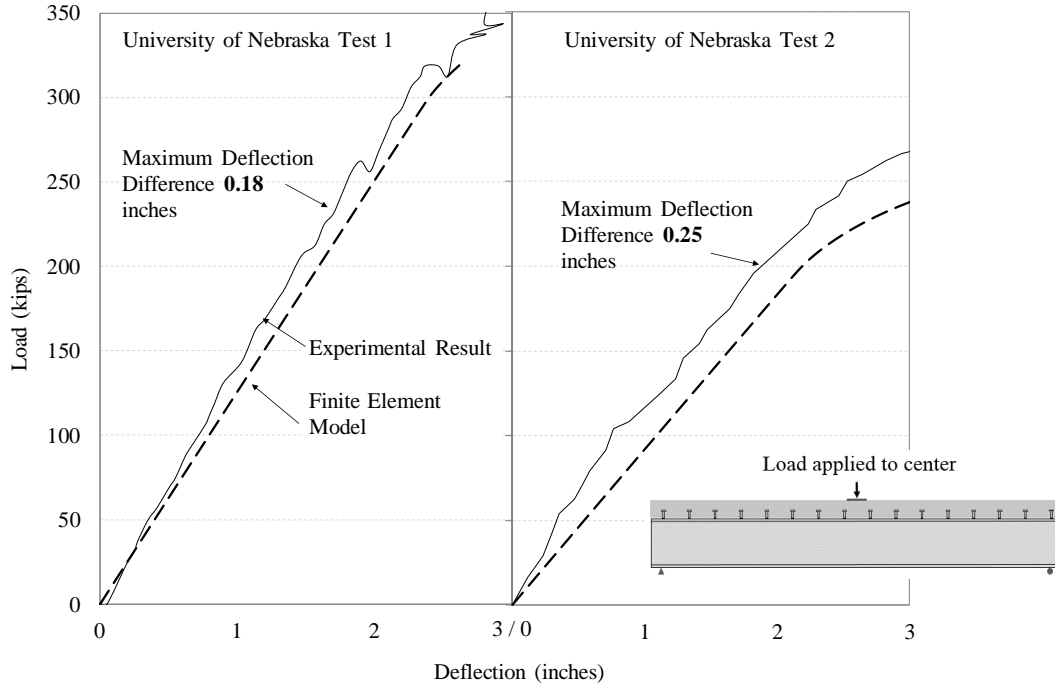


Figure 32 Load vs. deflection global results from University of Nebraska tests and finite element model predictions

3.4 Results and Discussion

Results indicate that the assumption of a continuous shear flow through the studs at the steel-concrete interface is non-conservative for stud pitches greater than 24 inches. Figure 33 and Figure 34 show resulting stud shear forces recorded at the steel-concrete interface for the 100ft span and the 200ft span finite element models respectively. The solid lines in Figure 33 and Figure 34 represent the shear flow, V_{SR} (shown again in Equation 23).

$$V_{sr} = \frac{VQ}{I} \quad (\text{Equation 23})$$

Note that the shear flow was found for discrete span sections equal to $1/20^{\text{th}}$ of the total span length. From the 100ft girder span shear demands shown in Figure 33, the current AASHTO

shear flow equation reasonably predicts stud shear demands while the stud pitch remains less than 24 inches. Note that current specification requirements limit stud pitch to 24 inches; however, a modification to 48 inches will take effect in the new version of the standard. Beyond a 24 inch stud pitch where studs are clustered in rows of 3 or more studs, shear demands predicted by the AASHTO continuous shear flow equation greatly under-predict measured demands (see again Figure 33). With larger stud spacing, the distribution of shear force within the clustered stud rows varies by more than 100%, with studs in the first and last cluster row carrying more than twice the shear force of the cluster interior rows (see Figure 35).

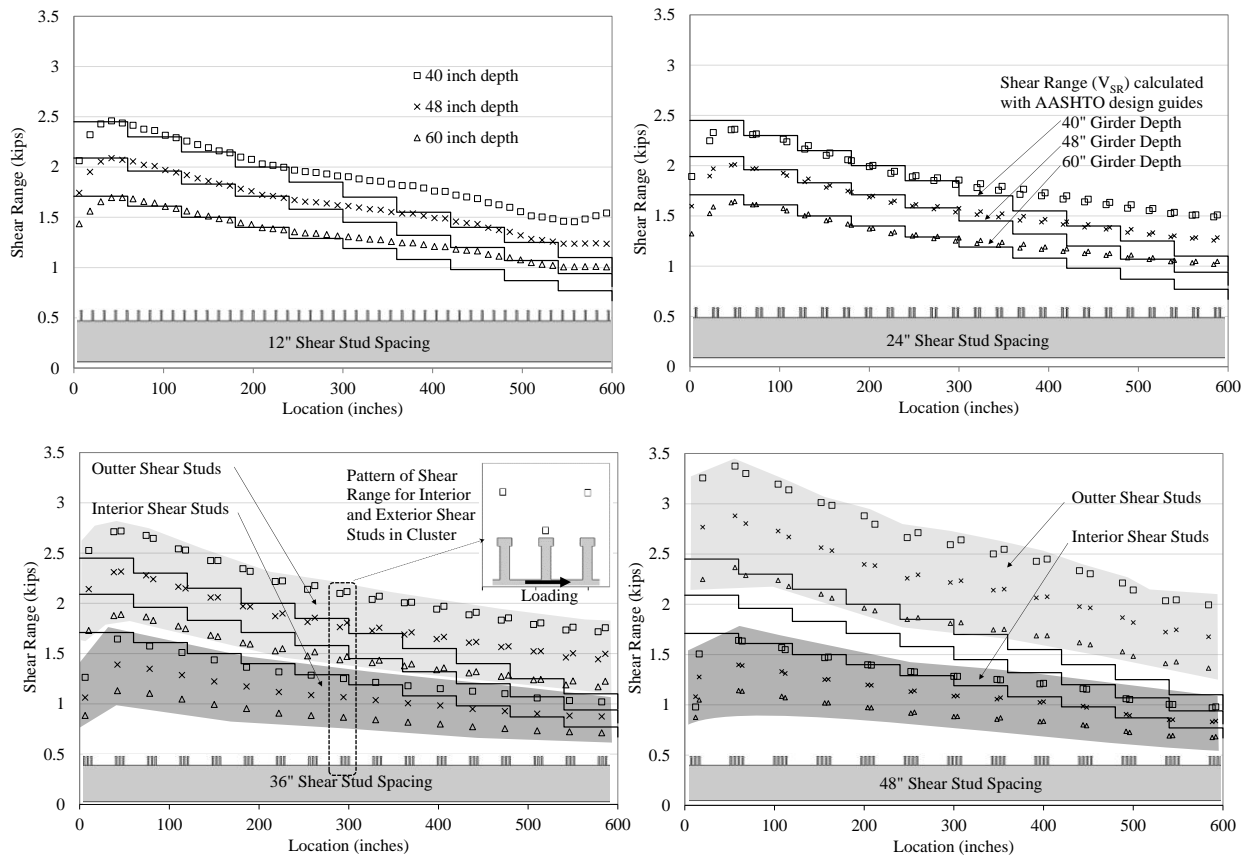


Figure 33 Shear force range in studs for finite element models of 100ft length

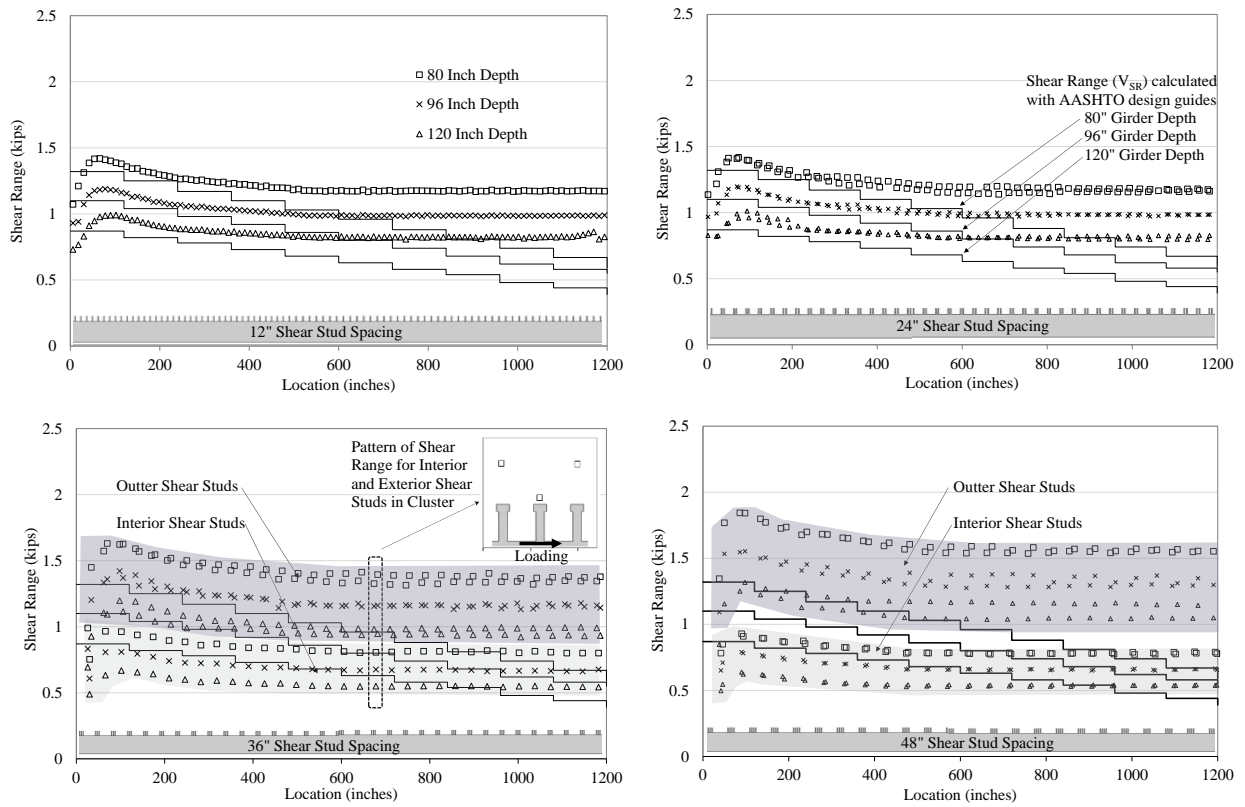


Figure 34 Shear force range in studs for finite element models of 200ft length

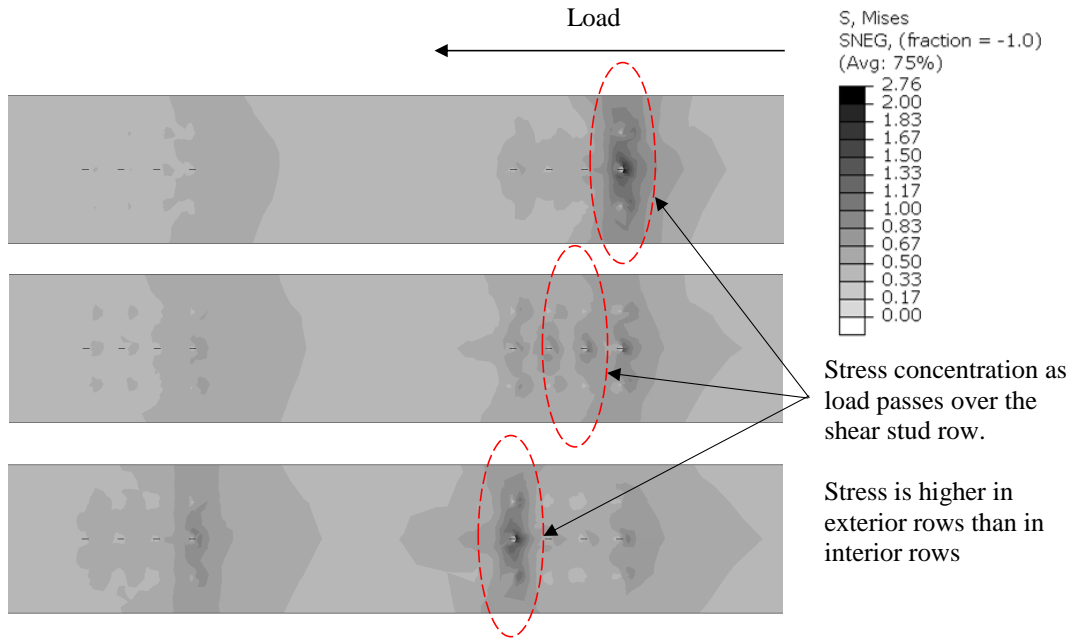


Figure 35 Shear force concentrations in rows within a cluster as load travels across surface

As girder span increases to 200ft, span effects are evident in the stud shear demands (see again Figure 34). Shear flow stud demand predictions from the AASHTO specification under-predict measured stud shear forces near mid-span of the 200ft span models for all stud pitches and all girder depths. As shown in Figure 34 stud demands tend to level off near the girder mid-span while prediction equations (which are based on the wheel-induced vertical shear forces) estimate a linear decay of stud demand as all models consider a simply supported condition.

From Figure 33 and Figure 34, girder depth has little effect on the shear force range demand at larger stud spacings, other than the expected changes resulting from modifications to the moment of inertia (I) and first moment of area (Q) which are both accurately predicted in the AASHTO calculation for shear demand (V_{SR}).

Results from measured and predicted stud demands suggest a relationship between number of clustered stud rows and center-to-center stud cluster pitch where the *tributary* stud pitch along the girder flange determines the resulting stud demands. This tributary stud pitch concept assumes the shear force follows the shortest path between the concrete deck to the steel girder throughout the span length. In the models analyzed, the interior stud rows are always spaced at 4 inches, making the assumed tributary span length only 4 inches for interior cluster rows. For exterior cluster rows the tributary span length contains half of the space between clusters (in this case clusters are 36" and 48" apart) and the space between exterior cluster rows. The two-row clusters do not vary from the predicted V_{SR} , presumably because the tributary span length attributed to each row is the same. For the 48" clusters containing two interior cluster rows and two exterior cluster rows, the highest tributary stud distance corresponds to the highest measured stud demand. The following section develops a modification to the existing AASHTO

shear flow equation for determining stud demands in clusters of studs having spacings greater than 24 inches.

3.4.1 Development of Demand Equations for Clustered Studs Having Pitch greater than 24”

Assuming that the shear stress range experienced by studs is related to the tributary stud pitch, an equation for the minimum center-to-center pitch between clusters of shear studs is developed.

The center-to-center pitch between clusters of studs (p_c) is measured from the centerline of each stud cluster. Spacing between rows within a cluster (s) is chosen by the designer, and minimum values for concrete placement are specified in the AASHTO provisions. It is recommended that the same guidelines that govern transverse spacing in AASHTO also govern the longitudinal spacing between rows of shear studs within a cluster. The number of rows of studs within a cluster (n_r) and the number of studs within a row (n) are also considered. Figure 36 shows the clustered stud pitch variable (p_c) and spacing of stud cluster rows (s).

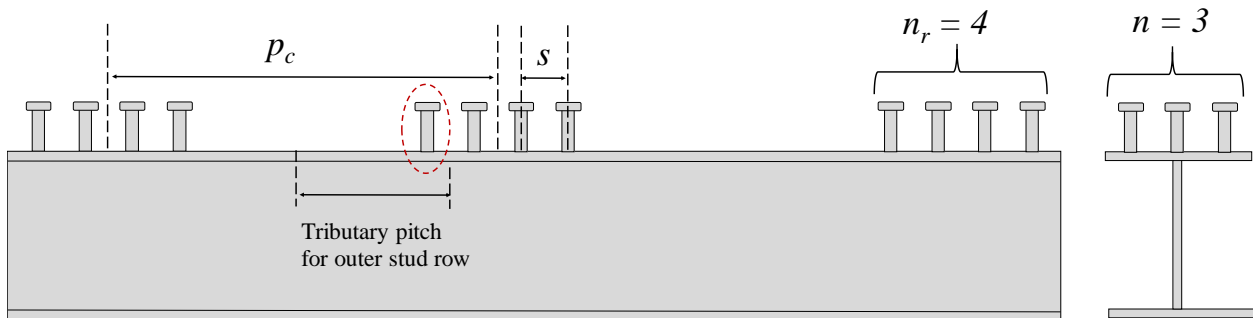


Figure 36 Definition of terms in development of p_c spacing

The resulting tributary pitch for the outer-most row of studs in a cluster is given by Equation 24.

$$\frac{p_c}{2} - \frac{(n_r - 1)s}{2}$$

Equation 24

This distance is assumed to be the flange length attributed to the outer-most row of shear studs. When this distance is multiplied by the shear flow, V_{SR} , the result is the shear force demand for the outer-most row of studs (in units of kips). Equation 25 presents the total shear force range for a shear stud in the exterior cluster row, which results from the length in Equation 24 being multiplied by the shear demand V_{SR} and the number of rows in the cluster (n_r) over the number of studs in a row (n).

$$\left(\frac{p_c}{2} - \frac{(n_r-1)s}{2}\right) \left(\frac{n_r}{n}\right) V_{SR} = \Delta F \quad \text{Equation 25}$$

For design, this stud shear demand must be less than the stud fatigue capacity.

$$\Delta F \leq Z_r \quad \text{Equation 26}$$

Equation 26 is also written as follows:

$$1 \leq \frac{Z_r}{\Delta F} \quad \text{Equation 27}$$

By substituting Equation 25 into Equation 27, the minimum required pitch between stud clusters is calculated as:

$$p_c \leq \frac{2nZ_r}{n_r V_{SR}} + s(n_r - 1) \quad \text{Equation 28}$$

Note that the horizontal shear range per unit length, V_{SR} , and the fatigue shear resistance of individual shear stud connectors, Z_r , presented in Equation 28 are each calculated in the same manner as currently outlined in AASHTO section 6.10.10 [1]. From Equation 28, a cluster geometry can now be selected by choosing the number of shear connectors in a cross-section (n), selecting the number of rows in a cluster of shear studs. The recommended steps to determine the pitch between clusters of shear studs using Equation 28 are outlined below.

1. Determine shear range per unit length (V_{SR}) as outlined in AASHTO 6.10.10.1.2 (Eq. 6.10.10.1.2-2)
2. Determine fatigue shear resistance of an individual stud shear connector (Z_r) as outlined in AASHTO 6.10.10.2 (Eq. 6.10.10.2-1 and 6.10.10.2-2)
3. Select a number of shear connectors in a cross section (n)
4. Select the number of rows in a cluster (n_r)
5. Select the shear stud spacing between rows (s). Currently no minimum pitch is outlined in AASHTO, it is recommended that the minimum spacing between rows of shear studs follow the same guidelines as those for *transverse spacing* between shear studs found in AASTHO 6.10.10.1.3.
6. Determine minimum center-to-center pitch (p_c) between clusters of shear studs:

$$p_c \leq \frac{2nZ_r}{n_r V_{SR}} + s(n_r - 1)$$

Figure 37 and Figure 38 show the stud shear force range predicted using the proposed demand equation presented in Equation 28, along with the measured stud demands from the 100ft and 200ft span finite element models respectively. In Figure 37 the proposed stud demand equation reasonably predicts the peak stud shear range measured from the finite element models throughout the entire bridge span (note than only half of the girder span is shown in the figure). For the 200ft span models shown in Figure 38, the proposed stud demand calculation is able to reasonably capture the peak stud demands near the girder abutments (the locations of highest shear) but falls short of accurately predicting the stud demands for studs beyond L/4 of the girder span. Given the near constant stud shear demands beyond L/4 of the girder span, it may be reasonable to modify Equation 28 to remain constant beyond L/4 for simply supported span lengths of 200ft or greater.

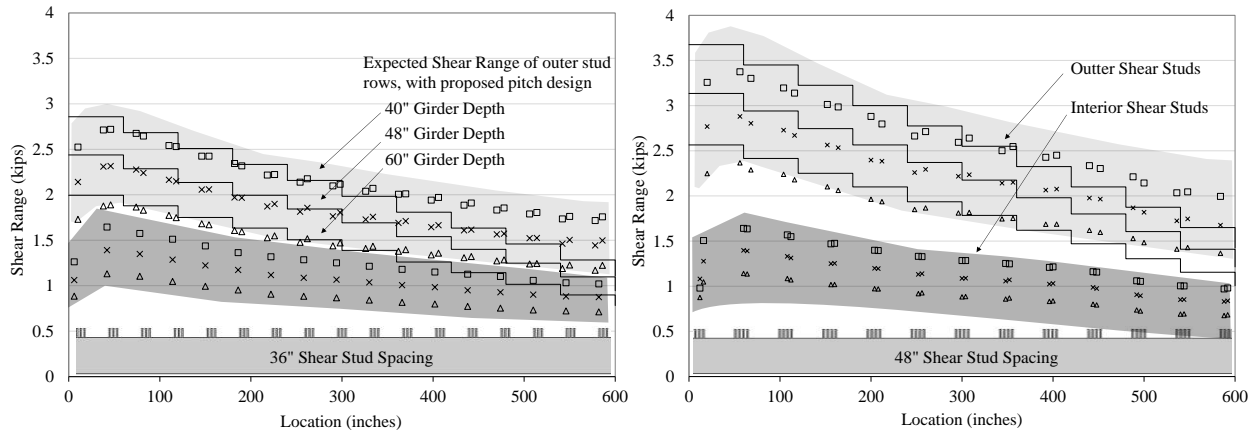


Figure 37 Shear stress range of 100ft span FE models with proposed V_{SR} calculation

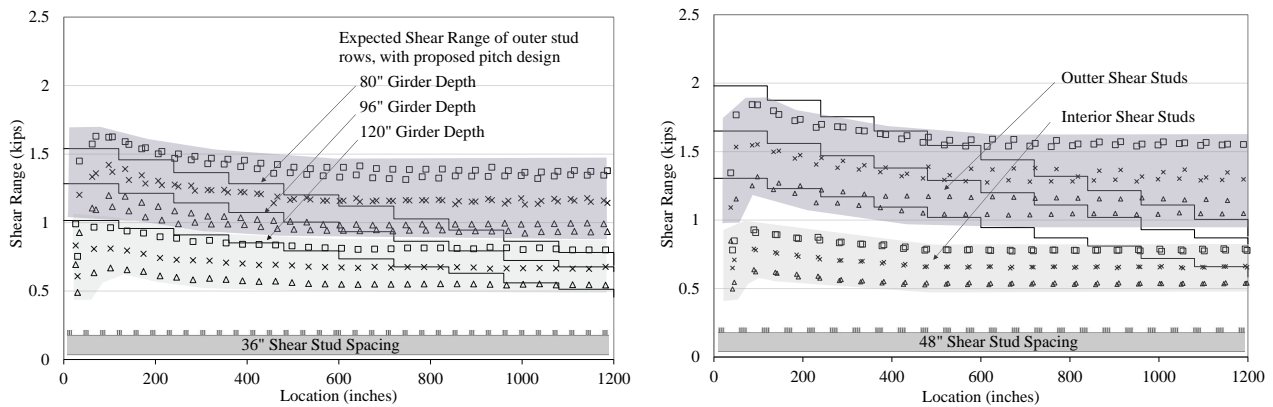


Figure 38 Shear stress range of 200ft span FE models with proposed V_{SR} calculation

3.5 Summary and Conclusions

In this chapter, a parametric finite element study was used to investigate the effect of shear stud pitch, girder depth, and girder span on the shear demand transferred through shear studs in composite bridge girders. A total of 24 detailed finite element models were analyzed using the commercial software ABAQUS and considered 4 different shear stud pitches, 3 different girder depths, and 2 different span lengths. The finite element model geometries were formed from four-node linear shell elements (S4R in ABAQUS) comprising the steel beam and the concrete deck. Composite connection between the steel girder and concrete deck was achieved using discrete springs and flange partitions at shear stud locations, similar to other

studies simulating composite girder behavior. Finite element modelling methods were validated using existing experimental results from the University of Nebraska [37] and the Turner Fairbanks Highway Research Center [10]. All composite girders in the parametric investigation were designed in accordance with AASHTO design specifications [1] and loaded using moving axle weights corresponding to the AASHTO fatigue truck.

The shear stud spacing and clustering of shear stud rows has a significant effect on stud shear force demands. Results from the finite element parametric study indicate that stud shear force demands are increased as stud cluster pitch extends beyond 24". In composite girder analyses with single rows of studs and clustered studs at 24" spacing, the shear demand predicted by AASHTO shear flow equation closely matched model stud shear forces. However, in stud clusters spaced at 36 and 48 inches, the AASHTO shear flow prediction equation drastically under predicted forces found in the outer-most rows of each stud cluster (see again Figure 33 and Figure 34). These effects of shear stud spacing and clustering on the shear demands are not currently considered in the AASHTO predicted V_{SR} shear flow equation and modification was needed to improve prediction. The effects of girder depth and the girder span were close to that predicted by the geometry parameters in the current V_{SR} equation, which accounts for girder geometry with the inclusion of the moment of inertia and the short-term area moment.

Considering shear force distribution through tributary flange length, a modified equation for shear demands in clustered stud groups was developed. The modified demand equation developed for determining acceptable clustered stud pitch, $p_c \leq \frac{2n \cdot Z_r}{n_r V_{SR}} + s(n_r - 1)$, accurately captures higher shear demands in the outer stud rows.

Chapter 4: DETERMINATION OF RESIDUAL FATIGUE LIFE IN THE SHEAR STUDS OF EXISTING COMPOSITE BRIDGE GIRDERS FOLLOWING DECADES OF TRAFFIC LOADING

4.1 Background

Aging of the nation's bridge infrastructure a significant issue that requires attention, as over half of the steel bridges within the United States have met or exceeded their initial design life. Current AASHTO specifications require bridge designs to achieve a 75 year fatigue design life [1]; however, previous versions of the specifications prior to 1998 only required design for a 50-year fatigue life. This is significant as approximately 158,600 of the estimated 181,000 steel bridges in the United States were designed and constructed prior to the 1998 code change from a 50 to 75 year design life [38]. Additionally, nearly 51% of these pre-1998 bridges are currently 50 to 75 year design life [39]. Figure 39 shows the age distribution of steel bridges in the United States as taken from the National Bridge Inventory. Note in Figure 39 that the bridges aged between 0-19 years were designed to the currently required 75-year design life. [39]

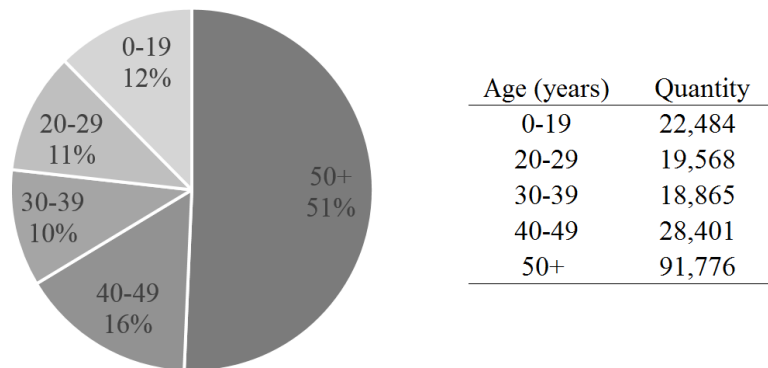


Figure 39 Distribution of the age of steel bridges within the United States

With so many bridges over or close to their design fatigue life it is important to understand what residual fatigue capacities remain within the shear studs that provide the steel-concrete composite action and required strength for service loading. Unfortunately, management

and maintenance inspections that occur over the bridge life are largely visual and therefore only show deterioration of the exposed bridge superstructure [40]. Shear stud fatigue damage cannot be examined prior to demolition of the concrete bridge deck, and it is unclear what existing fatigue damage has occurred within the studs of these bridges having more than 50 years of service. Forensic analysis of decommissioned bridges having removed concrete decks would allow determination of internal deterioration and residual fatigue life within the studs and create a better understanding of stud fatigue processes that occur during the service life of actual bridges [41].

Very limited research exists on the residual composite strength of decommissioned high-traffic bridges having more than 50 years of service, and following an extensive literature search, no studies were found to have investigated the residual fatigue capacity of shear studs within a 50-year-plus decommissioned bridge. One study has examined the residual shear strength of a decommissioned bridge with static loading tests [42]; however, as stud failure is often governed by fatigue processes [17] this study provides little insight into the residual fatigue life. The lack of research on residual shear fatigue capacity is likely due to the focus of published research on bridge collapse rather than forensic analysis of bridges removed in non-catastrophic ways [43].

Investigation into the residual fatigue capacity of shear connectors in existing highway bridges would be valuable to evaluate existing fatigue prediction models and help provide evidence for over-conservancies in existing stud demand predictions. This chapter experimentally investigates the residual fatigue life of existing high-traffic bridges using non-destructive and destructive techniques. Two bridges are chosen for the study, 1) a decommissioned bridge along Interstate 40 (I-40) in Arkansas, and 2) an airport-road interstate overpass bridge in Arkansas undergoing a scheduled lane expansion. Both bridges provide

unique opportunities for investigation as they have the concrete bridge decks carefully removed prior to decommissioning or expansion.

The chapter begins by discussing the experimental program, including detailed descriptions of the bridges investigated. Following, a historic traffic count study is presented to help estimate existing fatigue damage and an overview of the non-destructive and destructive testing methods are described. Next, an experimental fatigue test setup is discussed along with the specimen fabrication, geometry, and loading. Finally, results from the non-destructive and destructive testing are presented and conclusions are summarized.

4.2 Experimental Program

The experimental study consists of two parts: 1) non-destructive testing and 2) destructive fatigue testing. The non-destructive testing methods used in this experimental program are magnetic particle testing and dye penetrant testing. As will be described in following sections, these non-destructive methods allow identification of existing fatigue cracks within non-failed components. The destructive testing involves further fatigue testing of pushout specimens having been fabricated from portions of the decommissioned bridge along I-40.

4.2.1 Bridge Descriptions and Traffic Loading

Bridge A is located in Lowell, Arkansas on Highway 264 at the point Highway 264 crosses Interstate 49. Figure 40 shows the location of Bridge A within Northwest Arkansas. Access to shear studs on the bridge for non-destructive testing became available as the bridge was being widened. The original bridge was built in 1982 as a multi-girder continuous composite bridge spanning 266 feet with three piers along the span at the center-line and 84 feet off of the centerline to the east and the west as shown in Figure 41. Bridge A contains 8 girders spaced at 7 feet which are comprised of 5 beams connected by bolted splice plates. All beams are A572

Gr50 steel with beam sizes varying across the span. Original plans for Bridge A obtained from the Arkansas State Highway Transportation Division (AHTD) indicate a design using 4" long $\frac{3}{4}$ " diameter headed shear studs with rows containing 3 studs at 2" lateral spacing. The plans indicate a design pitch varying from approximately 8" to 17" longitudinally along the girder; however, when the shear studs were uncovered it was discovered that existing shear stud pitch ranged from 12" to 20" indicating that the shear studs were exposed to higher stresses for each in-service fatigue cycle than was accounted for in design. During the bridge widening, additional shear studs were welded to exposed girder flange to correct for the increased stud demands.

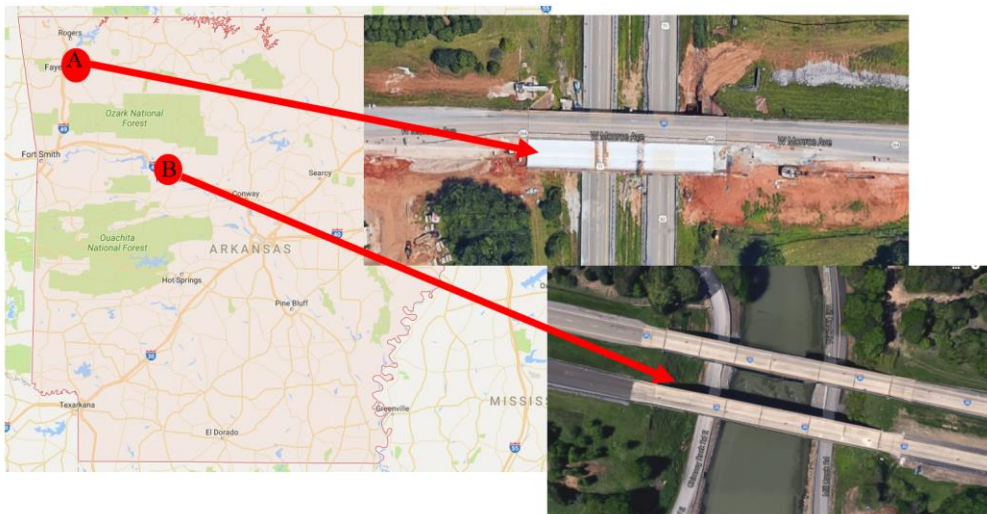


Figure 40 Location of Bridge A and Bridge B in Lowell and Russellville, Arkansas

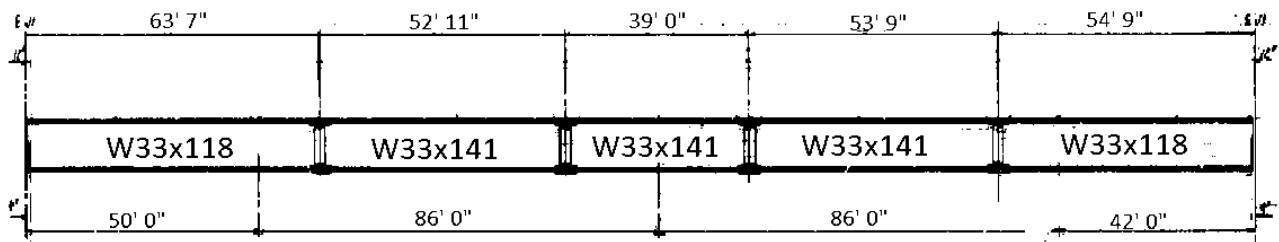


Figure 41 Girder elevation view and span dimensions for Bridge A

Bridge B was decommissioned and removed from I-40 just west of Russellville, Arkansas, one of the most heavily traveled interstate sections in the US. Figure 40 shows the location of Bridge B spanning Mill Creek Road and a portion of Lake Dardanelle, as it currently exists following replacement. The portion of Bridge B used in the experimental program were taken from the east bound bridge which contains six simply-supported spans, ranging between 55 feet to 75 feet in length. All specimens used in this study were taken from the 55 foot simply supported span. This 55 foot span contains 5 composite girders spaced at 6.5 feet on center. The removed girder used for this experiment is a W27x84 rolled section created from A36 steel. The shear connectors used are 7/8" shear studs in rows of 3 at 2" lateral spacing. The pitch of the studs at the point of investigation for this study is 10 inches (see Figure 42).

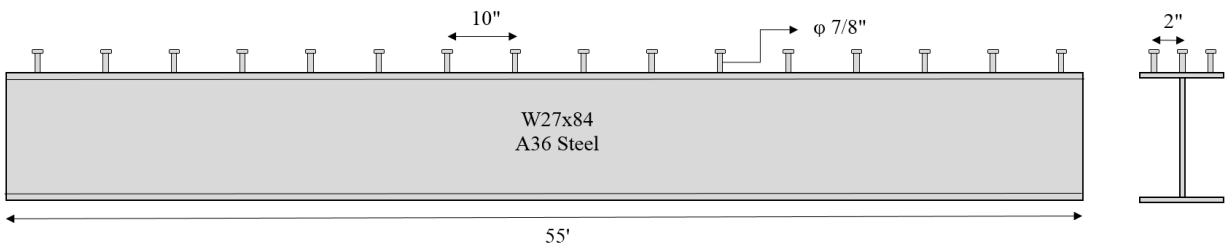


Figure 42 Representation of 55 foot girder removed from Bridge B for testing

Existing fatigue damage due to in-service loading for each bridge is estimated from average daily traffic counts from AHTD traffic counting stations. To help reduce counting errors resulting from traffic exiting or entering prior to the bridge location, counting stations nearest to each bridge location were chosen. Unfortunately, average daily traffic count data is only available between 1986 and 2015, which post-dates construction of both bridges. To estimate traffic experienced by each bridge in the years prior to 1986, two approaches are taken to bound the possible traffic counts: 1) consideration of no traffic prior to 1986 (providing a lower-bound traffic count), and 2) assumed average daily traffic equal to the first year of available data in

1986 (likely providing a conservative upper-bound traffic count). Average daily truck traffic (ADTT), used in shear connector design, was estimated as 20% of the average daily traffic per AASTHO C3.6.1.4.2. [1]. Figure 43(a) shows the resulting ADTT estimations per year for Bridge A and Bridge B and Figure 43(b) shows the cumulative ADTT fatigue cycles experienced. As shown in Figure 43(b), Bridge A experienced between 25 and 30 million ADTT fatigue cycles and Bridge B experienced between 38 and 53 million ADTT fatigue cycles during their service life. Note again that the lower and upper fatigue cycle values likely bound the actual ADTT demand, as traffic data is merely assumed prior to 1986.

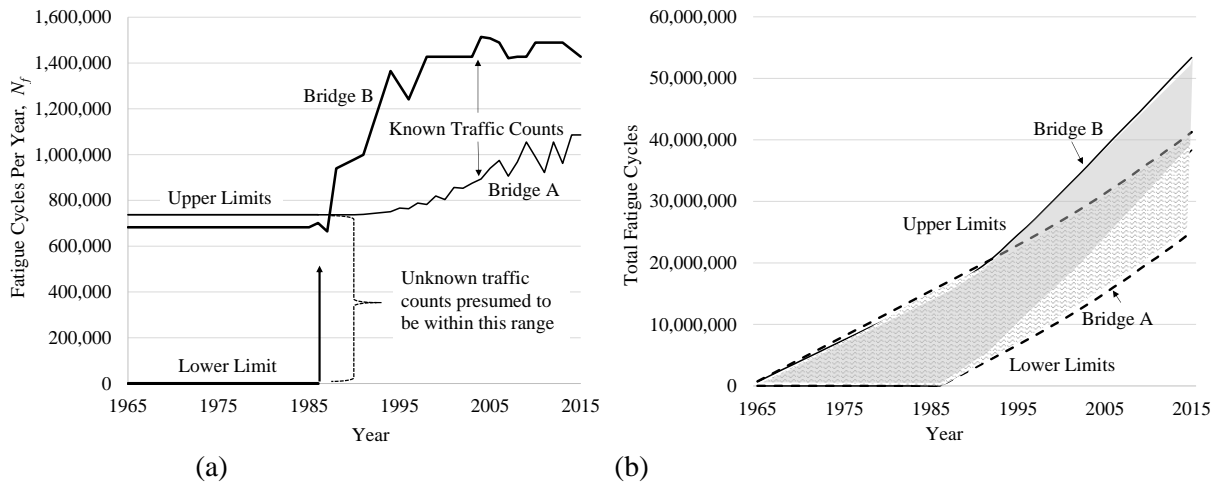


Figure 43 ADTT Estimations of (a) fatigue cycles per year and (b) total fatigue cycles experienced during the lifetime for Bridge A and Bridge B

4.2.2 Overview of Non-Destructive Testing Methods

The following paragraphs provide an overview of the non-destructive magnetic particle inspection (MPI) and dye penetrant testing (DPT) that were performed on each bridge following deck removal. Note that a certified MPI/DPT contractor was provided by W&W|AFCO Steel to ensure quality control during all crack inspection processes.

4.2.2.1 Overview of Magnetic Particle Inspection

Magnetic particle inspection (MPI) is a non-destructive testing process used on ferromagnetic materials to detect surface cracks. During the MPI process, a magnetic field is created around the area to be inspected and particles are applied to the surface which cluster around surface discontinuities. Cracks can be visually detected as these particles cluster due to the magnetic flux. Figure 44 shows the MPI processes with magnetic field lines varying across an existing flaw which attract the magnetic particles to the flaw surface. The detailed procedures for MPI testing are provided by ASTM Specification E 709-95 and summarized in the following paragraphs.

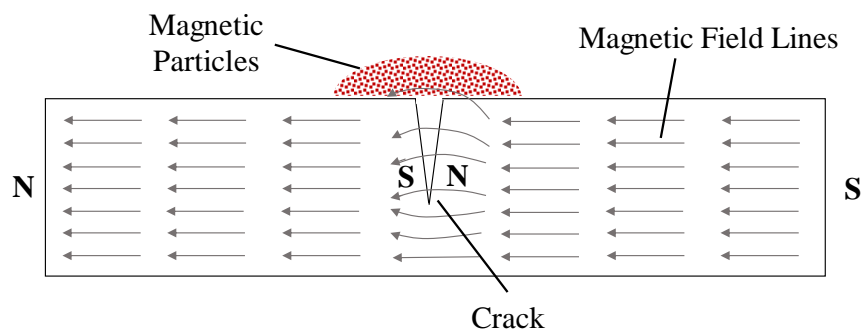


Figure 44 Schematic of magnetic particle inspection process

The technique employed in the magnetic particle testing for this study was dry continuous magnetization. Magnetization can be done with a variety of equipment as listed in ASTM E709-95 [44]. The equipment used in this study is a yoke consisting of a hand-held C-shaped electromagnet. According to ASTM E709-95, the magnetization should be done in at least two directions as cracks parallel to the normal path of the magnetic field lines are often undetectable. In this study dry magnetic powder, which can be fluorescent or non-fluorescent, was used in conjunction with the yoke. Magnetizing current was initiated using the yoke prior to the application of the dry magnetic powder (see Figure 45). The dry powder loses mobility once

it is in contact with the surface so it is important for the magnetic current to be in place prior to powder application as it will move according to the magnetization while still airborne. The powder accumulates in line with the magnetic field and disruptions in that accumulation occur at points of flux leakage (see Figure 45). These disruptions are called indications. Indications are examined and classified without disturbing the powder. [44]



Figure 45 Magnetic particle testing done on shear studs of Bridge A

A total of 18 studs, from various longitudinal locations along the girder, were investigated for fatigue cracks on Bridge A using the MPI procedure. The 18 studs were located near the girder abutments (where regions of highest shear stress are anticipated) and near the girder mid-span (where stud pitch is greatest). Results from the MPI investigations are presented in the Results section.

4.2.2.2 Overview of Dye Penetrant Testing

Dye penetrant testing (DPT), also called dye penetrant inspection, is another widely used non-destructive testing method for locating surface cracks or flaws. This method, unlike MPI, may be used on either non-ferrous or ferrous materials.

During the DPT process, the steel surface is cleaned, and a penetrant is applied and allowed time to penetrate the undetected surface cracks. Following the penetrant application, the surface is wiped clean to remove any excess penetrant that did not enter a crack. A developer solution is then applied to draw the penetrant to the surface thereby making the previously invisible surface flaws detectable by visual inspection. The DPT steps are shown in Figure 46(a) and the detailed DPT procedure is outlined in ASTM Specification E 1417[45].

Prior to application of the penetrant solution, cleaning is required and involves ensuring all surfaces are dry, free of soils, oil, grease, paint, and other coatings [45]. This cleaning can involve mechanical cleaning, solvent cleaning, and chemical cleaning. Once clean, the entire surface of the component to be inspected is covered with penetrant by spraying, dipping, brushing, or other methods that cover the surface completely. In this study, the penetrant was applied by brushing (see Figure 46(b)). The penetrant is left untouched for a minimum of 10 minutes, or a minimum of 20 minutes in colder temperatures between 40⁰F and 50⁰F but not longer than two hours to prevent drying. Following the dwell time, excess penetrant is removed.

Removal of excess penetrant can be done in a variety of ways indicated in ASTM E1417, including: spray, manual wiping, immersion, or rinsing depending on the type of surface being examined and the type of penetrant used. In this study, manual wiping was used to remove the excess penetrant (see again Figure 46(b)). If a dry developer is used the components are dried between intermediate cleaning and application of developer; if an aqueous solution or suspendable developer are used, the component is drained of excess water but not dried. Following removal of the excess penetrant, developer is applied to the surface and the surface is examined within the maximum bleed-out time (which varies by type of developer). According to

ASTM E1417, if inspection does not occur before the bleed-out time the component must be re-processed.

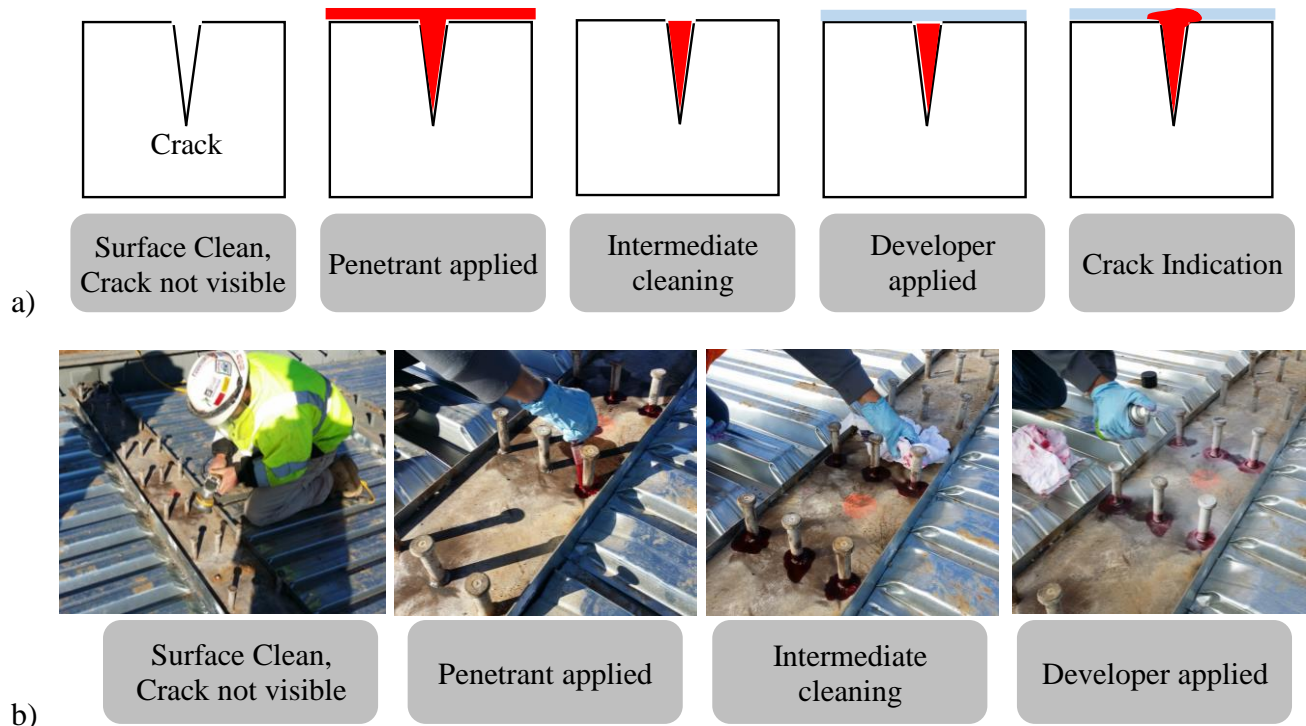


Figure 46 a) dye penetrant testing process b) dye penetrant testing of Bridge A

4.2.3 Overview of Experimental Fatigue Testing

In addition to the non-destructive DPT and MPI crack investigations designed to determine existing fatigue damage following in-service loading, destructive fatigue testing was performed on three portions of Bridge B to determine residual stud fatigue capacities. The fatigue test setup, including specimen geometry, fabrication, instrumentation, and loading used are described in the following sections.

4.2.3.1 Test Specimen Geometry and Fabrication for Fatigue Testing

Figure 47 shows the experimental push-out specimen geometry which is similar in dimension to those used in Chapter 2 for the CAFL study. Unlike the push-out specimens previously fabricated however, the specimen fabricated in this chapter are from steel removed

from Bridge B, having already been subjected to years of traffic loading. Portions of the top flange and web of the W27x84 55 foot span were removed at various locations along the girder length (creating T-sections with welded studs). Each T-section portion was 26 inches in length and approximately 5" deep into the web. Six portions were removed, each containing two rows of shear studs. Two T-section portions from similar longitudinal locations were then welded together along the web to form a double sided steel push-out specimen. Figure 47 shows the girder section removal and welding to create the push-out specimen geometry. Similar to the testing of Chapter 2, the chosen geometry for the specimens (double-sided push-out specimens) is based on guidelines for shear-stud testing prescribed in the Eurocode [16]. In this study, a total of 3 double-sided push-out specimens were fabricated from Bridge B.

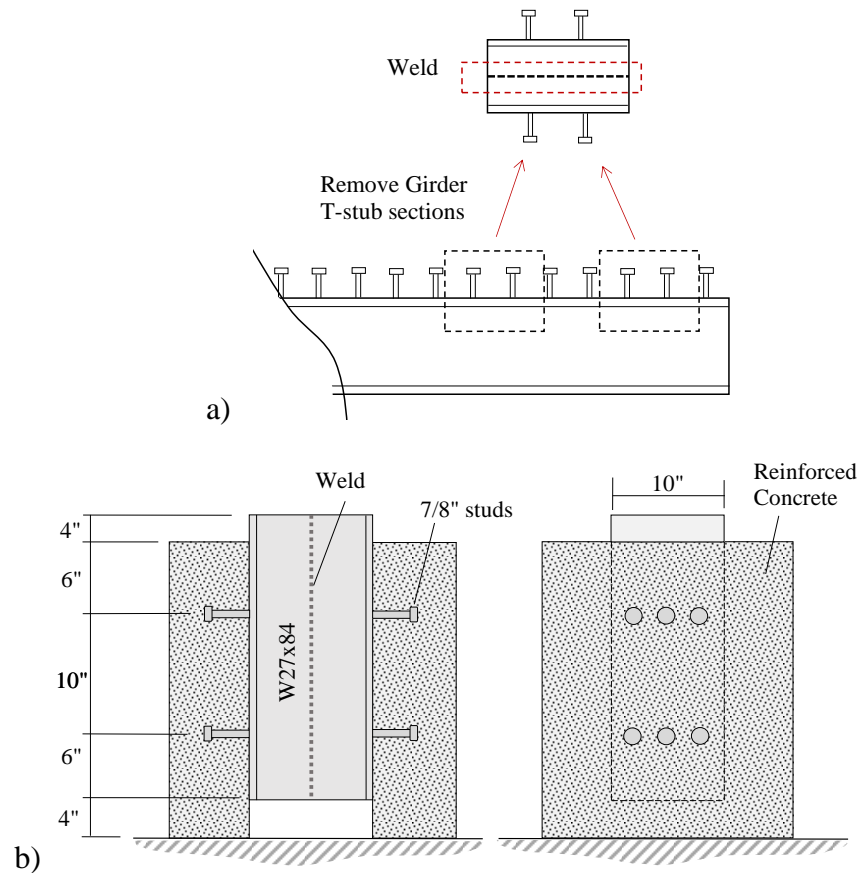


Figure 47 a) Fabrication of steel double sided specimen b) push-out specimen dimensions

Concrete slabs cast around the fabricated bridge sections are designed to represent typical composite bridge conditions. All concrete sections consider normal weight concrete from a standard highway bridge deck mix design, and each concrete section is cast with the beam in a horizontal position (see Figure 48). Compressive strength of the concrete is checked by breaking concrete cylinders at the time of fatigue testing. Concrete strength data for each of the three bridge specimens are presented in Appendix B – with specimen labels R1, R2, and R3 representing the three specimens discussed in this chapter. As in earlier push-out fatigue testing, adhesion between the steel and concrete is prevented by applying a coat of grease to the steel flange prior to concrete casting (see Figure 48).



Figure 48 Placing concrete on steel beam sections by greasing steel flange, placing rebar, and casting concrete in horizontal position

4.2.3.2 Test Configuration, Instrumentation, and Loading

The experimental setup, shown in Figure 49, is designed to apply rapid, high-shear stress cycles to studs within the push-out specimens. This setup differs from the previous fatigue push-out test setup due to the larger compressive capacity needed for the three push-out tests which each contain 6 shear studs with a diameter of 7/8” as opposed to 4 shear studs with a diameter of

3/4” from the previous testing. The increase shear stud size and quantity requires a higher force for the same stress range, which exceeds the capacity of the setup used previously in Chapter 2.

In the test setup, a steel self-reacting frame with stiffening beams is used along with a hydraulic actuator, as shown in Figure 49(a, b, and d). The double-sided push-out specimens are loaded with the beam oriented horizontally (instead of vertically as done previously); the axial load is applied evenly to the end of the steel wide-flange section using a load distribution plate. Due to the horizontal loading condition, two Teflon sheets are placed between the specimen and the floor to reduce any significant friction force transfer. Additional stiffness to the self-reacting frame is provided by threaded steel rods placed on either side of the actuator to allow for higher frequency fatigue loading.

All specimens are subjected to unidirectional loading (specimens are loaded in one direction and then unloaded), resulting in a non-zero mean stress and providing a conservative fatigue loading condition as compared to reversed cycle loading. A pre-load of 3kips is maintained to prevent separation between the specimen and testing machine at unloading.

Each specimen was placed using a gypsum grout mixture between the end of the specimen and the concrete reaction base to ensure uniform contact. The concrete reaction base was created to provide a reaction base large enough for the entire specimen to react against, rather than having the upper and lower portions of the specimen extending beyond the edges of the steel reaction frame and creating stress concentrations at the edge of the specimen slabs.

Linear variable differential transducers (LVDTs) are used to provide local displacement measurements during testing. The configuration and number of LVDTs is similar to that used in the previous fatigue testing described in Chapter 2. A total of eight LVDTs oriented parallel and perpendicular to the beam axis are included on each test specimen, to measure relative slip and

separation between the concrete and steel sections. Figure 49(c) shows the LVDT placement within the push-out specimens.

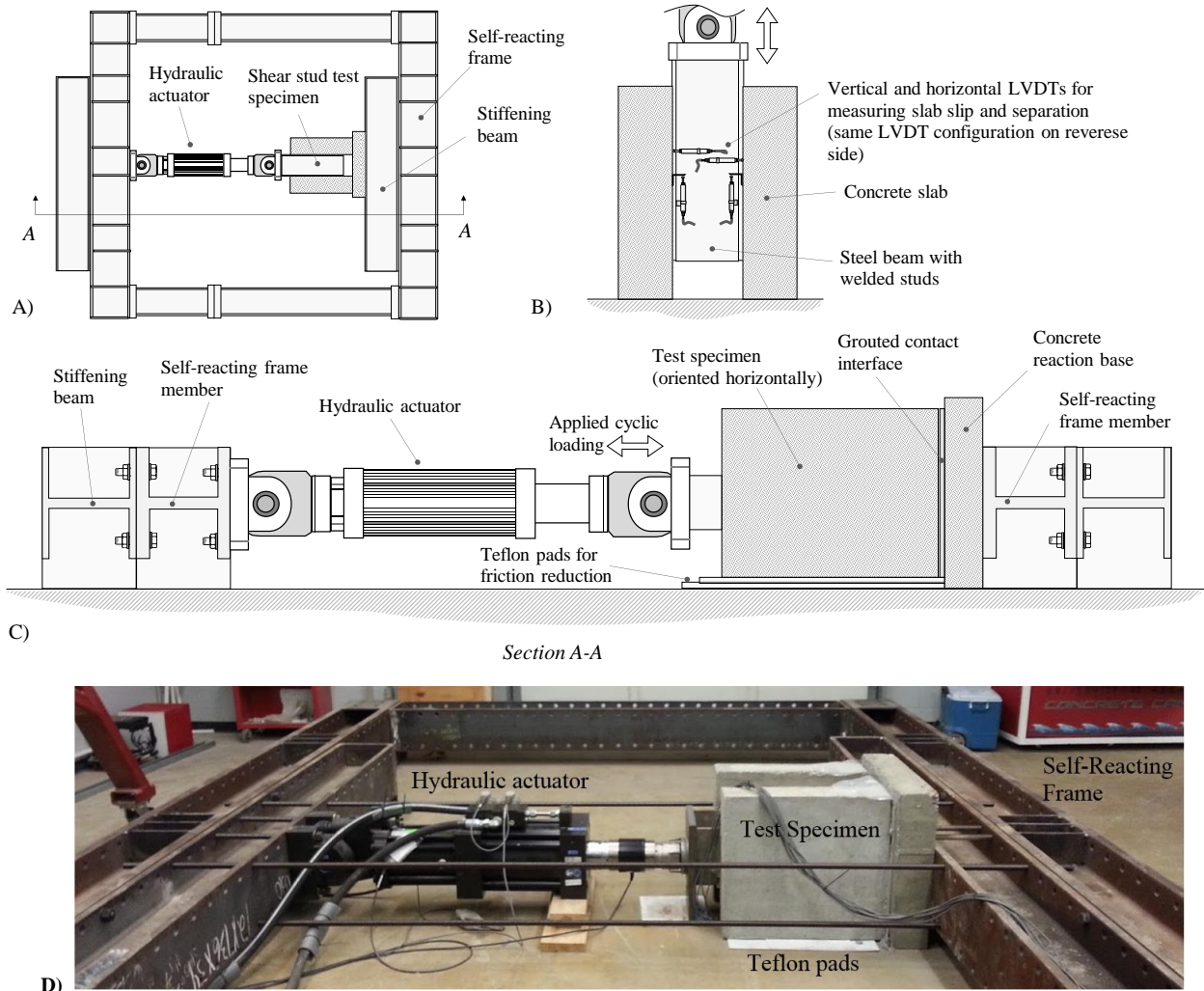


Figure 49 Experimental setup for pushout specimen fatigue testing showing: A) test set up plan view; B) specimen LVDT configuration; C) test setup elevation view; and D) image of test setup

Table 6 presents the experimental test matrix, including the specimen concrete strengths, applied stress ranges, and loading rates. In Table 6, the applied stress range is 11.6ksi (80MPa) for all specimens, with specimen loading rates applied at between 3 and 4Hz. These lower frequency loading rates are limited by the stiffness of the self-reacting frame and reinforcing

threaded rods which experienced approximately 0.5 inches of deflection during specimen loading.

Table 6 Experimental Test Matrix for tests R1, R2, and R3

Specimen Number	Average Concrete Compressive Strength (psi)	Applied Stress Range (ksi)	Loading (Hz)
R1	7624	11.6	3
R2	6842	11.6	4
R3	6884	11.6	4

4.3 Results

The following sections present the results of the non-destructive MPI and DPT investigations, as well as residual fatigue capacity results from the bridge component fatigue testing.

4.3.1 Magnetic Particle / Dye Penetrant Testing

Inspection of the shear studs on Bridge A was completed by a certified inspector and found that all 18 studs examined were acceptable with no detectable cracks. The shear studs were exposed as the bridge was undergoing widening and the concrete was removed by jackhammer. Note that some studs were hit with the jackhammer but remained welded to the steel flange (see Figure 50). Shear studs under examination were located near the abutment at the location of highest shear demand and near the mid-span at the location of greatest pitch between rows of studs.



Figure 50 showing shear stud bend to a 90 degree angle as a result of being hit with a jackhammer during concrete removal. Shear stud is still attached firmly to the steel flange

First a dye-penetrant test was performed on 6 of the studs, in the manner described previously, in accordance with ASTM 1417[45]. Figure 51 shows the penetrant being applied following cleaning, followed by spraying of the developer onto the surface. After the allotted dwell time it was determined that the geometry of the stud welds prevented conclusive determination of the existence of cracks around the base of the shear studs.

Following the dye penetrant test a magnetic particle test was performed in accordance with ASTM E709-95 [44] A magnetic field was created using an electromagnet and dry magnetic powder was applied to all 18 stud welds under inspection (see Figure 52). The results from these tests indicated that none of the studs tested were cracked. The welds on all 18 studs were found to be acceptable by the inspector. The report from the inspection is shown in Figure 53.



Figure 51 Shows penetrant applied and the developer being sprayed onto 6 shear studs



Figure 52 Magnetic particle testing and inspector

 INTERNATIONAL TESTING AND INSPECTION SERVICES, INCORPORATED 9921 Mann Road • Mabelvale, AR 72103 PH 501.455.3030 • FAX 501.455.3320 www.internationaltesting.com		TYPE OF INSPECTION Mag Particle <input checked="" type="checkbox"/> Dry <input type="checkbox"/> Wet <input type="checkbox"/> Fluorescent Current <input checked="" type="checkbox"/> AC <input type="checkbox"/> DC <input checked="" type="checkbox"/> Yoke <input type="checkbox"/> Coil <input type="checkbox"/> Prod Amperes _____		Penetrant Method <input type="checkbox"/> Dry <input checked="" type="checkbox"/> Wet <input type="checkbox"/> Fluorescent Emulsifier <input type="checkbox"/> Solvent <input type="checkbox"/> Developer <input checked="" type="checkbox"/> Dry <input type="checkbox"/> Wet		Date 10-26-15 Work Order/AFE No. _____ P.O. No. _____ Specification ALUS D1.5 Sheet 1 of 6	
MAGNETIC PARTICLE AND/OR DYE PENETRANT INSPECTION REPORT				Customer AFCO STEEL		Billing Address _____	
Location Lowell, AR Hwy 264		Project AFCO Research project		Contractor _____			
ITEM	QUANTITY	DESCRIPTION	RESULTS OF INSPECTION				
1	18	Sluar studs	Performed a dye penetrant test on 6 of the 18 studs. Penetrant results were inconclusive due to the geometry of the stud welds. A magnetic partical test was the performed on all 18 studs. The results from this test indicated that none of the tested studs were cracked. All stud welds were found to be acceptable				
TRAVEL TIME	Land 6	Departed Lab 6:30	<input checked="" type="checkbox"/> PM	Magnetic Particles			<input type="checkbox"/> Pounds <input type="checkbox"/> Gallons
	Air	Arrived Job 9:30	<input checked="" type="checkbox"/> PM	Aerosol Pressure Cans			
	Water	Departed Job 11:30	<input checked="" type="checkbox"/> PM	Remarks			
OTHER TIME	Work Time 2	Arrived Lab 2:30	<input checked="" type="checkbox"/> AM <input checked="" type="checkbox"/> PM				
	Standby Time	Mileage 420 mi	<input type="checkbox"/> One Way <input checked="" type="checkbox"/> Round Trip				
	Meal Deduction	Per Diem	Man Crew				
Total Hours 8	<input type="checkbox"/> Half Day <input type="checkbox"/> Full Day						
Technician	Shawn Shackelford						
Assistant(s)							
Client's Rep.							
<small>International Testing & Inspection Services, Inc. will exert its best efforts in performing the work requested; however, the results reported represent good faith opinions only and are not to be considered as warranties or guarantees of quality, classification, or usability of materials examined. In no event, upon the signing of this field ticket by the customer's designated field representative, shall the liability of International Testing & Inspection Services, Inc., as to any items inspected or tested (including any liability as to selection and/or results of such test), exceed the charge by International Testing & Inspection Services, Inc. for the inspection of such items.</small>							
MT/PT - 08808							

Figure 53 Report for DPI and MPI on 18 studs of Bridge A

The results of no crack indications found in Bridge A is of particular interest because the actual shear stud pitch was greater than the pitch designed. In Bridge A the shear stud pitch designed was 8 inches center to center at the ends of the continuous beam and 17 inches center to center at the mid-span of the continuous beam. When the shear studs were uncovered it was discovered that the shear studs were actually approximately 10 inches center to center at the ends of the beam and 20 inches center to center at the midspan of the beam. The original pitch was designed at the constant amplitude fatigue limit of 7ksi (48.3 MPa), with the intention of designing for infinite fatigue life. The additional distance between rows of shear studs increased the shear range to 8.6 ksi (59.3 MPa) which indicates that the shear studs, as built, fall within the finite-life region of the S-N curve for shear stud fatigue capacity as shown in Figure 54.

According to the current AASHTO design procedures, a shear stress range of 8.6 ksi corresponds to a shear stud fatigue finite life of approximately 3,079,000 cycles; however, during the in-service life of the bridge, Bridge A was subjected to between 25 and 30 million ADTT cycles. This indicates that the accumulated damage in the bridge is over 800% of the expected finite life fatigue capacity, yet no cracks were detected. Chapter 2 suggests that the capacity curve of AASHTO is reasonably accurate which suggests that the shear demands experienced by the studs are likely lower than expected based on the considered shear flow calculations. Possible explanations for this involve contributions of shear resistance from adhesion and friction between the concrete deck and steel flange during traffic loading.

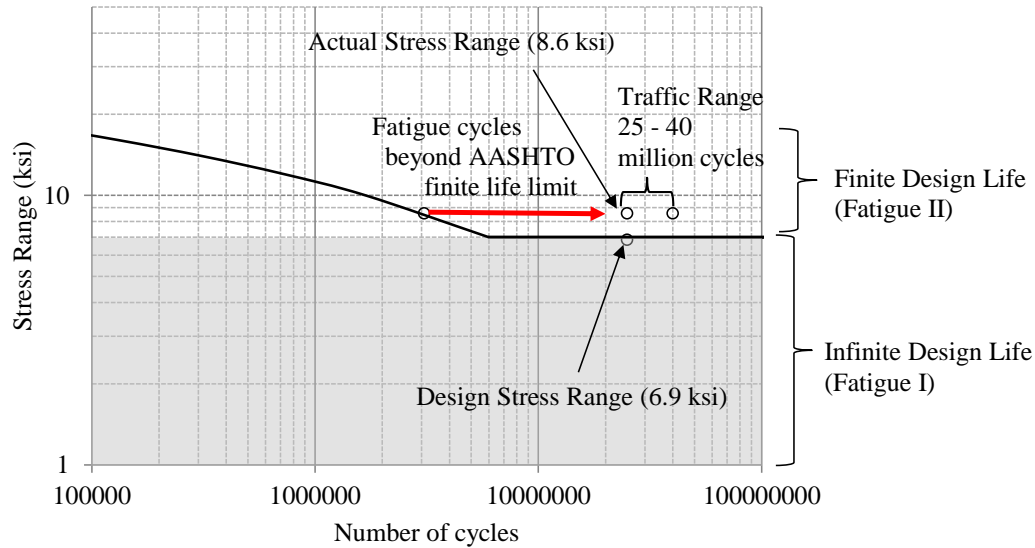


Figure 54 Design shear stud stress range vs. actual shear stud stress range in Bridge A

Another quality control inspector from W&W/AFCO Steel performed dye penetrant testing of Bridge B located near the center of the bridge span. In the dye penetrant tests a total of 36 studs were tested at 3 different sample locations (see Figure 55) and 35 of the 36 studs were found to be acceptable. The one stud not determined acceptable was rejected due to a lack of weld. The lack of weld could be due to damage done during concrete removal from the steel flange, which was done using a jackhammer, or simply lack of fusion during original construction.

In addition to the dye penetrant testing, magnetic particle inspection was also performed on Bridge B at the same location as the dye penetrant testing, near the center of the bridge span. A Parker Probe DA-400 electromagnet was used with Parker Red RP-6 magnetic powder. Results of the magnetic particle testing were similar to the dye penetrant testing in that one stud sample was rejected while the remaining shear stud welds were accepted. The DPT and MPI testing reports are shown in Figure 56 and Figure 55 respectively.

moved by hand with a crack visible before cleaning and polishing. Due to the extent of damage to the shear studs of test R2, the test was determined to be a failure rather than a run-out result. Specimen R3 was subjected to 3,519,001 cycles prior to be declared a runout. Table 7 shows the high-cycle fatigue test results, including the average concrete compressive strength, applied stress range and number of cycles to failure. Note that all three test specimens achieved more than 2.5 million cycles past the design limit of approximately 850,000 cycles at a stress level of 11.6 ksi (80 MPa). Figure 57 shows the three fatigue test results as compared to the current AASHTO stud fatigue capacity. Also, note that prior to fatigue testing, historic traffic counts estimate that Bridge B was subjected to between 38 and 53 million ADTT cycles.

Table 7 Results of Residual Shear Fatigue Life Tests

Specimen Number	Average Concrete Compressive Strength [psi]	Applied Stress Range [ksi]	Loading Rate [Hz]	Number of Cycles	Failure (F) or Runout (R)
R1	7624	11.6	3	3,590,011	F
R2	6842	11.6	4	4,415,003	F
R3	6884	11.6	4	3,519,001	R

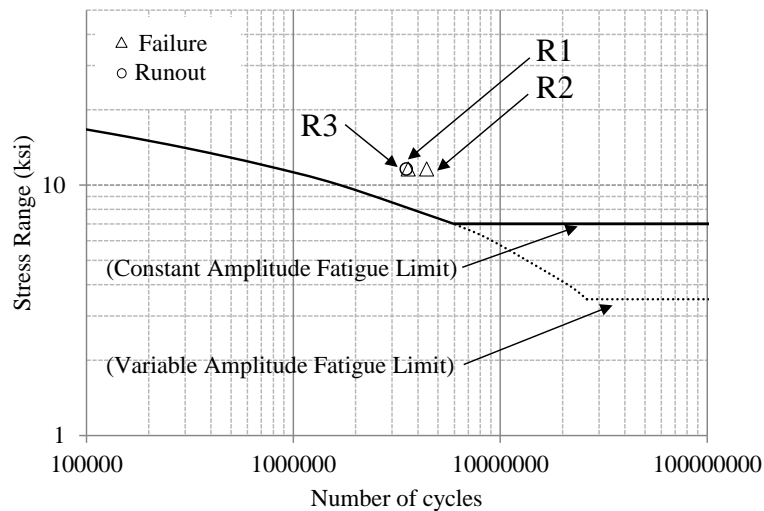


Figure 57 AASHTO design curve compared to failure points of tests R1, R2, R3

Figure 58 shows the resulting stud failure and slab separation of specimen R1. From Figure 58, failure of all 6 studs occurred near the weld-to-flange attachment, leaving pockets of material removed from the flange base metal. Additionally, little-to-no concrete damage was observed near the embedded studs, indicating limited fatigue contribution from stud flexural deformations.

The failed studs of specimen R2 (originally thought to be a run-out specimen) are shown in Figure 59. Following deck removal of specimen R2, as shown in Figure 59, two studs are completely separated from the top flange with the third stud of the row having little remaining attachment. While two of the studs failed, test R2 highlights the progressive nature of stud fatigue failure as the three remaining studs stayed intact (carrying more of the shear demands as studs progressively failed).

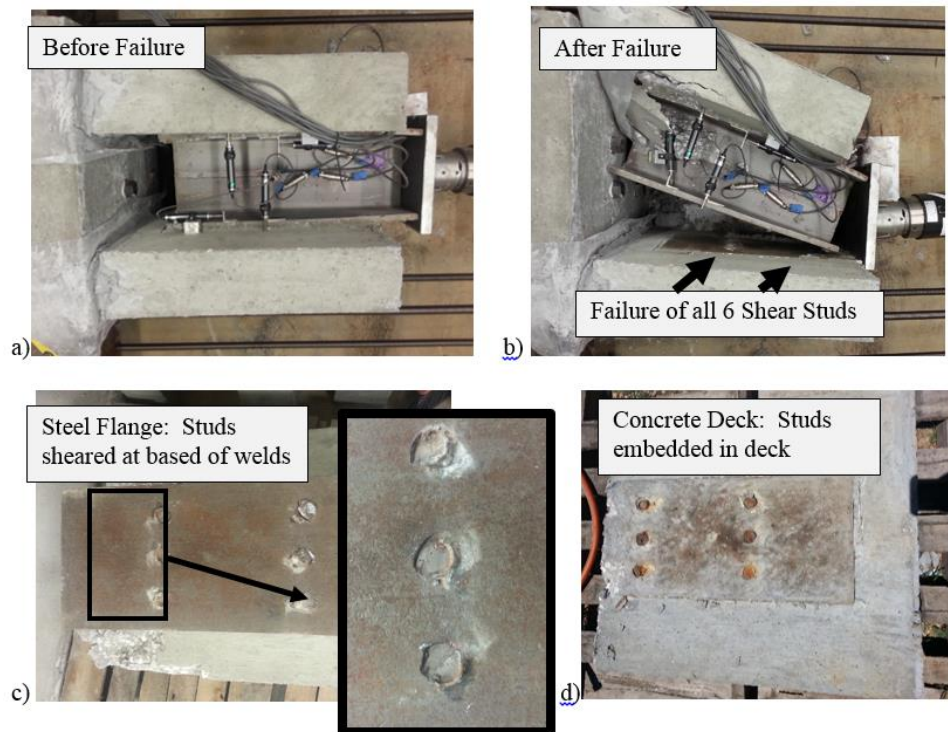


Figure 58 a) Test specimen before testing b) Test specimen failure c) Steel flange of test specimen showing divots where stud failed along base of weld through steel flange d) Concrete deck of specimen with shear studs embedded in deck

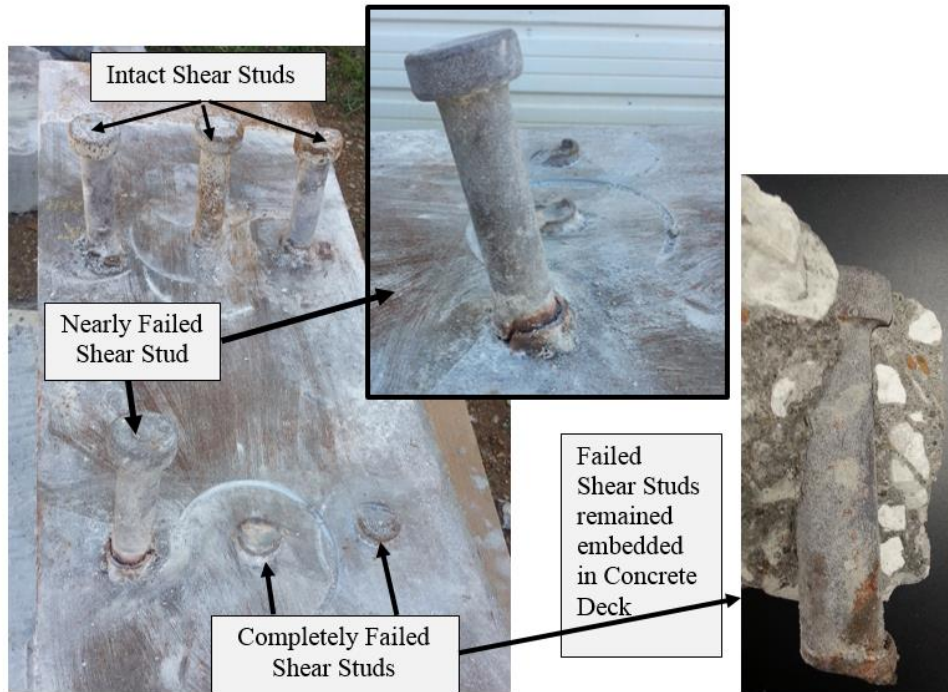


Figure 59 Test R2 failure of two shear studs and near failure of third shear stud

Test R3 did not fail and was stopped after 3,519,001 cycles, or 411% of the expected fatigue shear stud life with no external evidence of failure present. After concrete removal the studs were all still intact and more detailed stud-crack investigation was required as is discussed in the next section.

Slip and separation between the concrete slab and the steel beam were measured for test specimens R2 and R3 and are shown in Figure 60. Test R2, considered a failure specimen due to complete fracture of nearly 3 studs, showed a sharp increase in both slip and separation at approximately 2.5 million cycles. This is likely due to the shear failure of one or more of the shear studs in the first row (near the applied load). These slip and separation readings further highlight the progressive nature of shear stud failure. As shown in Figure 60, the slip and separation of specimen R2 increased at an exponential rate following the likely initial fractures

within the first stud row. Slip and separation measurements for test R3 show little change during the fatigue testing. From Figure 60, the slope of the average slip measurement for each slab in Specimen R3 remains relatively constant with only a slight upward gradient. This indicating that the shear studs had likely not separated from the flange as in test R2. While slip measurements suggest that the shear studs of Specimen R3 remained intact, a more detailed crack investigation is needed to determine whether fatigue cracks actually exist. This more detailed crack investigation is provided in the next section.

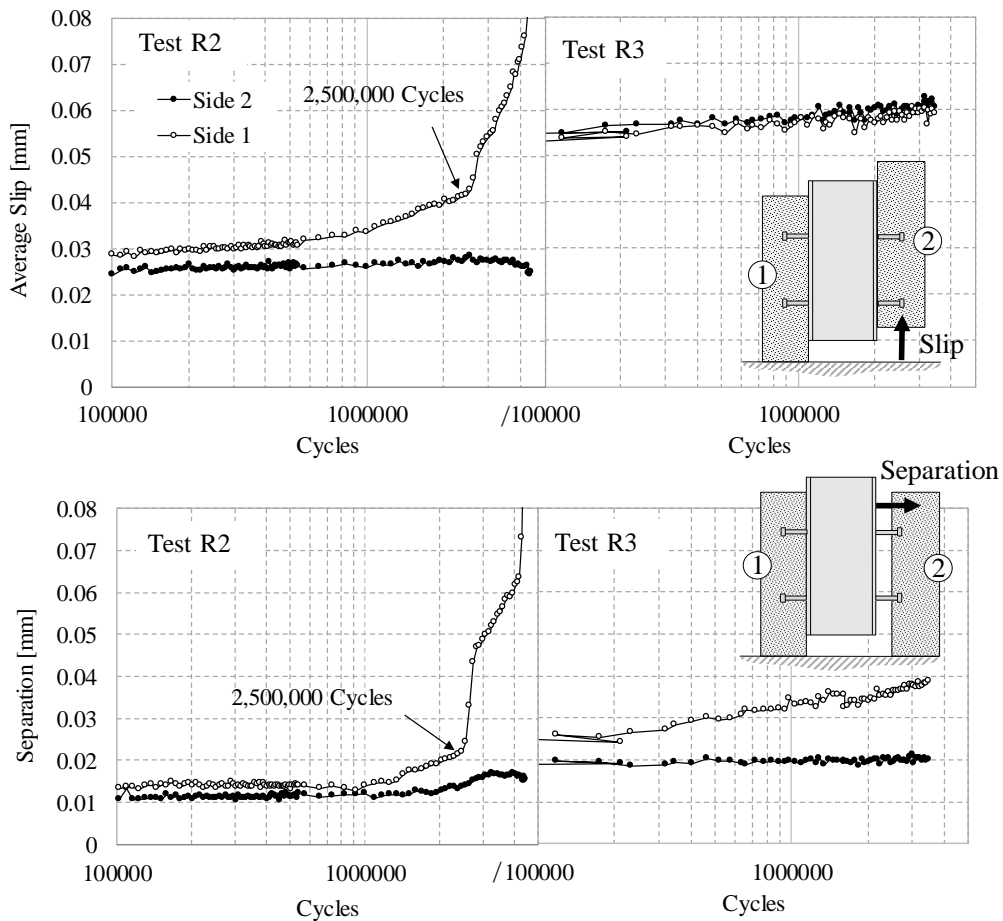


Figure 60 Slip and separation results for Tests R2 and R3

4.3.3 Stud Fatigue-Crack Investigations

Stud samples cored from test specimens R2 and R3, were sectioned, polished and surfaced etched in the same manner described previously. This process allowed for determination of whether cracks existed in the remaining shear studs of test R2 (those which were not completely failed) and in the intact shear studs of test R3. Figure 61 shows the polished stud cross-sections taken from the specimens with the cracks highlighted. Based on the Vickers micro-hardness measurements taken of previous fatigue test samples and described in Chapter 2 (shown here again as contours in Figure 61), it was determined that the fatigue cracks of tests R2 and R3 initiated near the weld HAZ at the stud-to-flange interface, just as seen in the Chapter 2. These initiated fatigue cracks were present in studs cored from Test R2 and Test R3.

Studs from test R2 contained significant cracking. There was only one of three studs in the front line that was not completely failed, that one stud, identified in Figure 61 as the front of R2, is barely attached to the base metal. The back stud of test R2 that was cleaned and polished contained cracking initiating between the weld and shear stud (between the fusion zone (FZ) and heat affected zone (HAZ)) and extending almost all the way through the cross section along the interface between the FZ and base metal (BM).

The shear studs from test R3 contained cracks initiating between the FZ and the BM. Figure 61 shows that the front stud of test R3 contained a crack that did not extend very far through the cross section, while the back stud contained a crack that extended through most of the cross section.

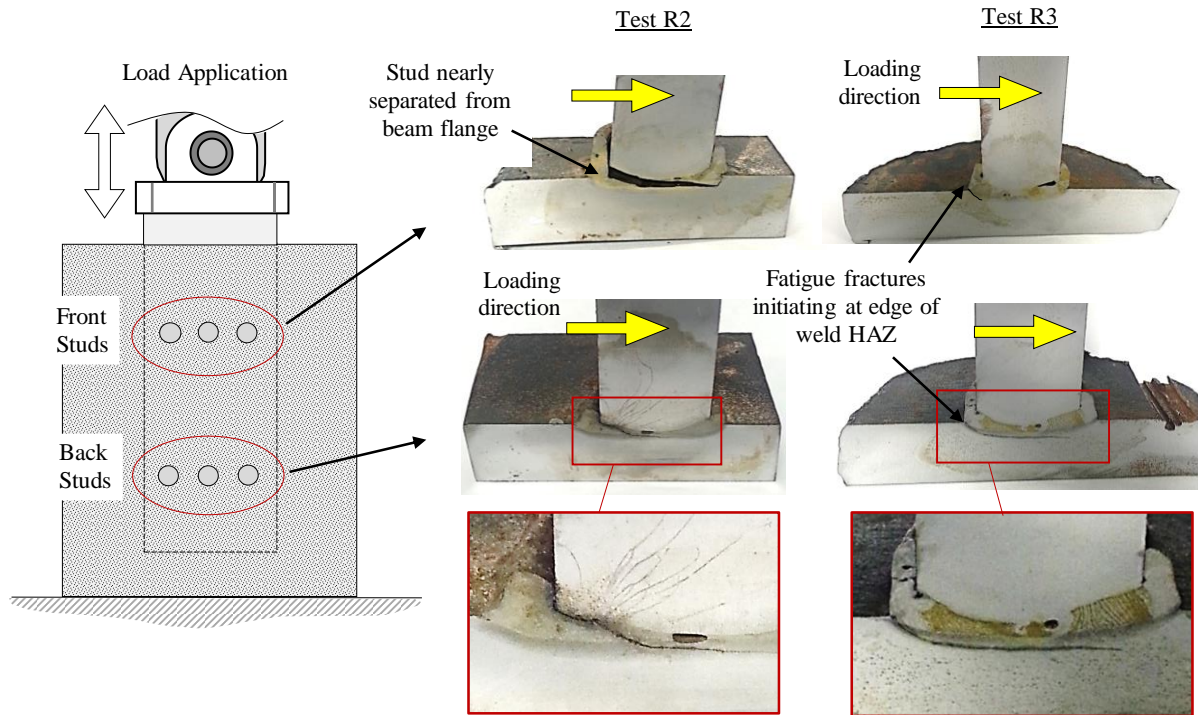


Figure 61 Cracks found in shear studs of test R2 and test R3 following deck removal and metallographic preparation of sectioned stud surface.

4.4 Summary and Conclusions

Two existing composite bridges (Bridge A and Bridge B) representing both high-traffic interstate and highway traffic demands were investigated for stud damage and residual stud fatigue capacity. Bridge A, having been in service for over 30 years, was estimated to have experienced between 25 million and 30 million ADTT cycles and Bridge B, having been in service for over 50 years was estimated to have experienced between 38 and 53 million ADTT cycles.

When the shear studs were uncovered on Bridge A (following deck removal) it was discovered that the fabricated stud pitch was actually several inches more than dictated in the design drawings. The additional distance between shear stud rows suggests that the shear stress range increased to 8.6 ksi, which is above the constant amplitude fatigue limit. The life-span of

25+ million cycles at 8.6 ksi is 800% of the expected life-span at that stress range. The lack of fatigue cracks within the studs of Bridge A (as determined from DPT and MPI testing) following a minimum of 25 million fatigue cycles at an estimated 8.6 ksi, suggests that the shear stress range estimation is higher than what is actually experienced by the shear studs. This discrepancy could be due to shear resistance contributed from adhesion or friction between the concrete deck and steel flange, which are not considered in the current AASHTO design calculations.

The shear stud fatigue design of Bridge B was for infinite life and therefore no cracks were expected in the shear studs of Bridge B. No fatigue cracks were found in either bridge. This lack of fatigue cracks is additional evidence that under low stresses, which is the case in infinite design life, shear studs do not fail, even after millions of fatigue cycles.

Sections removed from Bridge B were subjected to fatigue testing in addition to the non-destructive testing, which added another 3.5-4.5 million cycles at a higher stress of 11.6 ksi (80 MPa). All three tests exceeded the design life expectancy of approximately 850,000 cycles (for 11.6 ksi) by over 2.5 million cycles (over 400% of the expected shear stud fatigue life) even after the 38-53 million cycles experienced during the service life of the bridge. This evidence further corroborates that no existing damage existed in Bridge B at time of decommission and the shear studs were not in danger of failing, and corroborates the suggestion that the shear demand on shear studs assumed in design calculations is greater than the actual shear demand experienced by shear studs in service life.

Chapter 5: SUMMARY, CONCLUSIONS, CONTRIBUTIONS, AND AREAS FOR FUTURE RESEARCH

In the current AASHTO LRFD Bridge Design Specifications [1], fatigue capacities and demands for headed shear studs are based largely on limited studies conducted in the 1960s. As a result, the design specifications often require twice as many shear studs for fatigue than are needed to satisfy full-composite action in strength design. This study experimentally and analytically investigates shear stud capacities and demands and proposes modification to the current AASHTO LRFD specifications. The following sections summarize the individual research objectives and present relevant conclusions from the experimental and analytical stud investigations.

5.1 Experimental Investigation into the Shear Capacity of Headed Shear Studs

The first objective of this study was to re-evaluate the existing (arbitrary) CAFL for headed shear studs. This objective considered statistical analysis of fatigue push-out tests using a novel probabilistic approach, to capture fatigue data uncertainty and allow for the creation of characteristic capacity curves of similar form to other fatigue detail categories in the AASHTO provisions. The chosen probabilistic approach allowed for the inclusion of run-out test results, which had previously been neglected in analysis. The run-out tests from this study were all near the constant amplitude fatigue limit and were included in the analysis as well as run-outs in other data sets. A total of 6 push-out specimens were fatigue tested a low stress ranges between 4.4 ksi and 8.7 ksi (30MPa and 60MPa) which are close to the existing constant amplitude fatigue limit of 7 ksi. In these tests the effect of adhesion and friction between the concrete slab and the steel flange were neglected by applying grease to the steel flange before concrete placement. The

results of the six fatigue tests were combined with existing data-sets of measured fatigue life and analyzed using a probabilistic method called maximum likelihood estimation.

The analysis led to two conclusions: 1) the current AASHTO CAFL assumed for headed shear studs provides a reasonable estimation of the fatigue capacity and 2) the finite-life prediction presented in AASHTO is not representative of the large fatigue data-set considered.

The finite life portion of the S-N curve for shear stud fatigue life design was determined to be conservative and not representative of the large dataset considered in this study. Therefore, an alternative S-N curve is proposed, which takes the same form as other S-N fatigue curves in

AASHTO design of $(\Delta F)_n = \left(\frac{A}{N}\right)^{\frac{1}{m}} \geq (\Delta F)_{TH}$ where $m=4$ and $A=150 \times 10^8$. This curve unifies the fatigue details in AASHTO by following the same form as other fatigue details, which the current AASTHO S-N curve for headed shear studs does not follow. Note that stress range capacities provided in the proposed equation were derived using imperial units of ksi.

5.2 Analysis of Shear Demands Near the Steel-Concrete Interface

The second objective of this study was to determine the validity of the current shear flow demand equation considering changes in the shear stud pitch, girder depth, and girder span length. Current stud demand calculations assume a constant shear flow across the length of the girder even though shear is actually transferred at discrete stud locations along the girder length. Detailed finite element models were created to investigate the effect of stud pitch, girder depth, and girder length on the shear flow at the discrete stud locations. A total of 24 finite element models were created with 4 different pitches, 3 different girder depths, and two girder spans. The resulting stud shear force was measured at each stud-to-flange connection.

Finite element models indicate that the current AASHTO shear flow calculation is reasonable for the designs containing single rows of studs at a constant pitch and for clusters of studs in two rows at a constant pitch. For stud clusters containing three and four rows the shear forces at the discrete stud locations are significantly greater than predicted values using the AASHTO shear flow equation.

Considering tributary stud pitch, an modified stud demand equation and design approach was proposed as follows:

1. Determine shear range per unit length (V_{SR}) as outlined in AASHTO 6.10.10.1.2 (Eq. 6.10.10.1.2-2)
2. Determine fatigue shear resistance of an individual stud shear connector (Z_r) as outlined in AASHTO 6.10.10.2 (Eq. 6.10.10.2-1 and 6.10.10.2-2)
3. Select a number of shear connectors in a cross-section (n)
4. Select the number of rows in a cluster (n_r)
5. Select the shear stud spacing between rows (s). Currently no minimum pitch is outlined in AASHTO, it is recommended that the minimum spacing between rows of shear studs follow the same guidelines as those for *transverse spacing* between shear studs found in AASHTO 6.10.10.1.3.
6. Determine minimum center-to-center pitch (p_c) between clusters of shear studs:

$$p_c \leq \frac{2nZ_r}{n_r V_{SR}} + s(n_r - 1)$$

Figure 62 Suggestions for design of pitch of clustered shear studs

This design approach and modified demand equation accounts for stud cluster geometries and tributary stud pitch to provide the shear flow demand corresponding to the outer-most stud row in the clusters.

5.3 Determination of Residual Fatigue Life in the Shear Studs of Existing Composite

Bridge Girders

Two existing composite bridges which are in high traffic areas were investigated for stud damage and residual shear stud fatigue capacity. Bridge A underwent concrete deck removal as part of a bridge widening project. While the concrete deck was removed magnetic particle inspection and dye penetrant inspection were performed to check for indications of cracking at the base of the shear studs. Bridge B was decommissioned after over 50 years in service. Shear studs on Bridge B were tested for crack indications using magnetic particle inspection and dye penetrant inspection. Portions of Bridge B also underwent additional fatigue cycles to determine the residual fatigue capacity of the shear studs. Bridge A experienced between 25 and 30 million ADTT cycles in 30 years of service and Bridge B experienced between 38 and 53 million ADTT cycles over the 50-plus year service life.

A lack of fatigue cracks within Bridge A and Bridge indicates that the expected shear stress range is much higher than what is actually experienced by the shear studs. This could be due to contributions from adhesion and/or friction between the concrete deck and the steel flange, which are not considered in AASHTO design calculations.

Sections of studs from Bridge B subjected to between 3.5 and 4.5 million additional fatigue cycles beyond the 50-year traffic loading indicate adequate fatigue capacity comparable to that expected for studs in newly fabricated girders. Other force transfer mechanisms (such as concrete adhesion and friction) likely contributed to the low accumulation of stud fatigue damage during the bridge service life.

5.4 Contributions to Composite Bridge Design

The following list represents the original contributions from the dissertation work:

- 1) Experimentally measured residual fatigue capacities of existing bridge components following over 50 years of traffic loading.
- 2) Investigated existing cracking in studs of existing bridge girders following decades of traffic loading.
- 3) Developed a probabilistic approach to S-N curve generation and validated the existing AASHTO CAFL for headed shear studs.
- 4) Performed metallographic fracture investigations on studs from runout fatigue experiments.
- 5) Characterized local effects of the weld HAZ, BM, and FZ on fatigue crack initiation in welded studs.
- 6) Developed a probabilistic design equation for the finite-life fatigue capacity of headed shear studs.
- 7) Performed 24 detailed composite girder analyses and quantified shear force distributions in headed shear studs subjected to moving traffic loading.
- 8) Developed a stud shear-demand equation for grouped studs having pitches beyond the currently allowed 24-inch limit.

5.5 Recommendations for Future Work

It is recommended that additional research investigate force-transfer contributions of adhesion and friction between the concrete deck and the steel flange. Adhesion and friction are currently neglected in the experiments of this study as well as most studies into shear fatigue demands for headed shear studs. Results from the dissertation work suggest that the demands experienced by shear studs during actual traffic loading is lower than that predicted by the

AASHTO specification, likely due to contributions from adhesion and friction. A better understanding of these contributions would lead to more economic design.

It is also recommended that additional research be conducted to determine the shear demand of studs in clusters greater than 4 rows, and at spacings larger than the 48 inches considered in this research. Additionally, investigations into stud demands for girders having span lengths greater than 200ft may be warranted to further validate the proposed design equation.

To further validate the findings from the bridge investigations of Chapter 4, it would be interesting to investigate the fatigue behavior of full-scale girders having stud designs required for strength only. Such a study would further highlight fatigue mechanisms and stud demand distributions to help determine whether strength or fatigue actually govern in design.

REFERENCES

- [1] AASHTO (2012). AASHTO LRFD bridge design specifications (6th edition). American Association of State Highway and Transportation Officials. Washington, DC.
- [2] Mertz, D. (2012). "Steel Bridge Design Handbook: Design for Fatigue." *FHWA-IF-12-052*, 12.
- [3] Thurlimann, B. (1959). "Fatigue and static strength of steel shear connectors, Lehigh University, 1959 Reprint No. 144 (59-8)." Fritz Laboratory Reports. Paper 1253.
- [4] Slutter, R. G., and Fisher J. W. (1966). "Fatigue strength of shear connectors." *Highway Research Record No. 147*, Highway Research Board: 65-88.
- [5] Mainstone, R. J., and Menzies J. B. (1967). "Shear connectors in steel-concrete composite beams for bridges, Part I." *Concrete*, 1,(9). p. 291-302.
- [6] OSHA (2017). Regulations (Standards - 29 CFR). 1926.754(c)(1) Tripping Hazards., Occupational Safety and Health Administration, United States Department of Labor.
- [7] Rank, S. (Oct. 2013). "Clarification on Shear-Stud Hazards and OSHA Standard." *Local Line Newsletter, Iron Workers Union Local 387*, Iron Workers International, 25,(5). 11.
- [8] Badie, S. S., Tadros M. K., and Girgis A. F. (2006). "Full-Depth, Precast-Concrete Bridge Deck Panel Systems." *NCHRP Report 12-65*, Transportation Research Board, National Research Council.
- [9] Badie, S. S., Girgis A. F. M., Tadros M. K., and Nguyen, N. T. (2010). "Relaxing the stud spacing limit for full-depth precast concrete deck panels supported on steel girders (Phase I)." *J. Bridge Engineering, ASCE*, 15,(5). 482-492.
- [10] Provines, J., and Ocel, J. M. (2014). "Strength and fatigue resistance of shear stud connectors." *National Accelerated Bridge Construction Conference (ABC)*, December, 4-5, Miami, Florida.
- [11] Lehman, H. G., Lew, H. S., and Toprac, A. A. (1965). "Fatigue strength of 3/4 inch studs in lightweight concrete." *Research Report No. 76-1F*, Center for Highway Research, The University of Texas, Austin, Texas.

- [12] Roderick, J. W., and Ansorian, P. (1976). "Repeated loading of composite beams." *Civil Engineering Transactions*, CE18,(2). p. 109-116.
- [13] Naithani, K. C., Gupta, V. K., and Gadh, A. D. (1988). "Behavior of shear connectors under dynamic loads." *Materials and Structures*, 21.
- [14] Oehlers, D. J. (1990). "Methods of estimating the fatigue endurance of stud shear connections." *LABSE Proceedings P-145/90*: p. 65-84.
- [15] Johnson, R. P. (2000). "Resistance of stud shear connectors to fatigue." *J. Constructional Steel Research*, 56 (2000): 101-116.
- [16] Eurocode_4 (1994). "Design of composite steel and concrete structures Part 2: General rules and rules for bridges." *ENV 1994-2*, European Committee for Standardization. Belgium, Brussels.
- [17] Lee, K. C., Abbas, H. H., and Ramey, G. E. (2010). "Review of current AASHTO fatigue design specifications for stud shear connectors." *ASCE Structures Congress Proceedings*: p. 310-321.
- [18] Eurocode_4 (1994). "Design of composite steel and concrete structures Part 1-1: General rules and rules for buildings." *ENV 1994-1-1*, European Committee for Standardization, Brussels, Belgium.
- [19] Badie, S. S., Tadros, M. K., Kakish, H. F., Splittgerber, D. L., and Baishya, M. C. (2002). "Large shear studs for composite action in steel bridges." *J. Bridge Engineering*, ASCE, 7,(3). p. 1995-1203.
- [20] AHTD (2014). "Division 800, Section 802: Concrete for structures." *The Arkansas Standard Specification for Highway Construction*.
- [21] Hallam, M. W. (1976). "The behaviour of stud shear connectors under repeated loading." *Research Report No, R281*, University of Sydney, School of Civil Engineering, Sydney Australia.
- [22] Feldmann, M. H., O., Hegger, J., and Rauscher, S. (2011). "Fatigue behavior of shear connectors in high performance concrete." *Composite Construction in Steel and Concrete VI*: p. 39-51, doi: 10.1061/41142(41396)41144.

- [23] Ling, J., and Pan, J., (1997). "A maximum likelihood method for estimating P-S-N curves." *International J. of Fatigue*, 19,(5). p. 415-419.
- [24] Myers, A. T., Kanvinde, A.M., and Ibarra, L. (2012). "Maximum likelihood based parameter estimation of constitutive models for earthquake engineering." *15th World Conference on Earthquake Engineering*, Lisbon, Portugal.
- [25] D'Angelo, L., Rocha, M., Nussbaumer, A., and Bruhwiler, E. (2014). "Creation of S-N-P curves for reinforcing steel bars using a maximum likelihood approach." *Proc. Eurosteel*, Naples, Italy.
- [26] Prinz, G. S., and Nussbaumer, A., (2014). "Effect of radial base-plate welds on ULCF capacity of inanchored tank connections." *J. Constructional Steel Research*, 103,(2014). p. 131-139.
- [27] Pascual, F. G., and Meeker, W. Q. (1999). "Estimating fatigue curves with the random fatigue-limit model: 1 Introduction." *Technometrics*, 1999.
- [28] Coffin, L. F. (1954). "A study of the effects of cyclic thermal stresses in ductile metals." *ASME*, 76: p. 931-950.
- [29] Manson, S. S. (1954). "Behavior of materials under conditions of thermal stress." *National Advisory Committee for Aeronautics*, Technical note 2933. Tennessee,(USA).
- [30] Faust, T., Leffer, A., and Mesinger, M. (2000). "Fatigue of headed studs embedded in LWAC." *Second International Symposium on Structural Lightweight Aggregate Concrete*, 2,(2000). p. 212-220.
- [31] Mundie, D. L. (2011). "Fatigue testing and design of large diameter shear studs used in highway bridges." *Masters Thesis*, Auburn University, Auburn, AL.
- [32] Viest, I. M., and Siess, C. P. (1953). "Composite Construction for I-beam bridges." *Proc. Highway Research Board*, 32, FHWA, Washington, D. C.
- [33] Viest, I. m., and Siess, C. P. (1954). "Design of channell shear connectors for composite I-beam bridges." *Public Roads*, 28,(1).

- [34] Markowski, S. M. e. a. (2005). "Full-depth, precast, prestressed bridge panel system for bridge construction in Wisconsin." *Proc., PCI/National Bridge Conference*, Precast/Prestressed Concrete Institute, Palm Springs, CA.
- [35] Issa, M. A., Patton, T. A., Abdalla, H. A., Youssif, A. A. (2003). "Composite Behavior of Shear Connections in Full-Depth Precast Concrete Bridge Deck Panels on Steel Stringers." *Precast/Prestressed Concrete Institute (PCI) Journal*, 48,(5). 76-89.
- [36] Barth, K., Wu, H. (2006). "Efficient nonlinear finite element modeling of slab on steel stringer bridges." *Finite Elements in Analysis and Design*, 42: 1304-1313.
- [37] Mans, P. H. (2001). "Full scale testing of composite plate girder constructed using 70-ksi high performance steel." M.S. Thesis, University of Nebraska, Lincoln, USA.
- [38] Pough, K. (2015). "Development of Pre-stressed CFRP Fatigue Retrofits for Common Steel Bridge Connections." *Theses and Dissertations*, University of Arkansas.
- [39] F.H.W.A. (2013). "National Bridge Inventory." *U.S. Department of Transportation*.
- [40] AASHTO (2012). Manual for Bridge Element Inspection, 1st Edition. American Association of State Highway and Transportation Officials. Washington, DC.
- [41] Chase, S. B. (2014). "The Need for Conducting Forensic Analysis of Decommissioned Bridges." *UVA-2012-05*, University of Virginia.
- [42] Brackus, T. R., Barr, P. J., Cook, W. (2013). "Live-Load and Shear Connection Testing of Full-Scale Precast Bridge Panels." *J. Bridge Engineering, ASCE*, 18,(3). 210-219.
- [43] TRB (2016). "Characteristics of Decommissioned Bridges." from [HTTPS://RNS.TRB.ORG/DPROJECT.ASP?N=40831](https://rns.trb.org/dproject.asp?N=40831).
- [44] ASTM (2001). "E709-95 Standard Guide for Magnetic Particle Examination." ASTM International, West Conshohocken, PA.

[45] ASTM (2013). "E1417 Standard Practice for Liquid Penetrant Testing." ASTM International, West Conshohocken, PA.

APPENDIX A. SHEAR STUD FATIGUE DATASET

Table A-1 provides the $\frac{3}{4}$ " stud fatigue data set values used in determining the proposed design S-N curve in Chapter 2. Table A-2 provides the $\frac{7}{8}$ " stud fatigue values used in comparison. Failure modes described in Tables A-1 and A-2 refer to type A, B, or C fractures shown in Figure A-1.

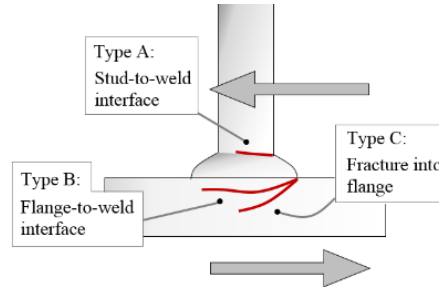


Figure A- 1. Common (type A, B, and C) fatigue fractures within shear stud connectors.

Table A- 1. Fatigue dataset for $\frac{3}{4}$ " diameter shear studs

Reference	Test Number	Specimen Name	No. of Slabs in Test	Studs/Side	Failure Mode	Stress Range (ksi)	N _f (cycles)
Hallam ¹	1	PS4	2	2	Type A	24.19	52,801
Hallam	2	PS42	2	2	Type A	24.19	52,836
Hallam	3	PS5	2	2	Type A	24.19	58,630
Hallam	4	PS52	2	2	Type A	24.19	67,877
Hallam	5	PS10	2	2	Type A	21.39	61,700
Hallam	6	PS102	2	2	Type A	21.39	75,500
Hallam	7	PS11	2	2	Type A	21.39	110,000
Hallam	8	PS112	2	2	Type A	21.39	110,000
Hallam	9	PS12	2	2	Type A	15.99	148,700
Hallam	10	PS122	2	2	Type A	15.99	174,800
Hallam	11	PS13	2	2	Type A	15.99	182,600
Hallam	12	PS132	2	2	Type A	15.99	182,600
Hallam	13	PS12	2	2	Run-Out	13.89	1,303,669
Hallam	14	PS1	2	2	Type A	13.89	1,303,669
Hallam	15	PS3	2	2	Type A	13.30	652,300
Hallam	16	PS32	2	2	Type A	13.30	652,300
Hallam	17	PS2	2	2	Type A	13.30	823,970
Hallam	18	PS22	2	2	Type A	13.30	845,000
Hallam	19	PS6	2	2	Type C	13.70	3,170,000
Hallam	20	PS62	2	2	Type C	13.70	3,554,000
Hallam	21	PS7	2	2	Type C	13.70	5,140,000
Hallam	22	PS72	2	2	Type C	13.70	6,096,000
Hallam	23	PS82	2	2	Type C	11.10	20,965,000
Hallam	24	PS8	2	2	Type C	11.10	21,391,000
Hallam	25	PS9	2	2	Type C	11.10	24,305,000

↓ Continued ↓

Table A-1: Continued...

Reference	Test Number	Specimen Name	No. of Slabs in Test	Studs/Side	Failure Mode	Stress Range (ksi)	N _f (cycles)
Hallam	26	PS92	2	2	Run-Out	11.10	35,000,000
Lehman/Lew ²	1	212	2	4	Run-Out	10.00	6,730,000
Lehman/Lew	2	616	2	4	Run-Out	10.00	5,810,000
Lehman/Lew	3	1020	2	4	Type B/C	10.00	6,711,000
Lehman/Lew	4	214	2	4	Type B/C	12.00	2,960,000
Lehman/Lew	5	618	2	4	Type B/C	12.00	2,223,000
Lehman/Lew	6	216	2	4	Type B/C	14.00	305,000
Lehman/Lew	7	620	2	4	Type B/C	14.00	1,345,000
Lehman/Lew	8	1024	2	4	Type B/C	14.00	390,000
Lehman/Lew	9	620B	2	4	Type B/C	14.00	726,000
Lehman/Lew	10	218	2	4	Type B/C	16.00	292,000
Lehman/Lew	11	622	2	4	Type A	16.00	435,720
Lehman/Lew	12	220	2	4	Type B/C	18.00	100,000
Lehman/Lew	13	624	2	4	Type B/C	18.00	142,680
Lehman/Lew	14	1028	2	4	Type B/C	18.00	340,300
Mainstone ³	1	S1	2	2	Type B/C	22.18	76,000
Mainstone	2	S10	2	2	Type B/C	28.07	1,700,000
Mainstone	3	S12	2	2	Type B/C	31.69	679,000
Mainstone	4	S2	2	2	Type B/C	17.66	439,000
Mainstone	5	S20	2	2	Type B/C	35.08	669,000
Mainstone	6	S23	2	2	Stud ⁹	35.08	657,000
Mainstone	7	S24	2	2	Yield	36.22	9,200
Mainstone	8	S25	2	2	Stud	38.48	13,300
Mainstone	9	S27	2	2	Stud	37.35	8,970
Mainstone	10	S28	2	2	Stud	37.35	6,000
Mainstone	11	S30	2	2	Yield	37.35	13,100
Mainstone	12	S31	2	2	Stud	36.22	8,600
Mainstone	13	S32	2	2	Stud	38.48	165,000
Mainstone	14	S33	2	2	Stud	37.35	106,000
Mainstone	15	S7	2	2	Stud	17.66	1,940,000
Mainstone	16	S9	2	2	Type B/C	24.45	42,000
Nathani ⁴	2	F2	1	1	Stud	22.64	3,200
Nathani	3	F1	1	1	Stud	22.36	1,000
Nathani	4	F3	1	1	Stud	16.77	23,000
Nathani	5	F4	1	1	Stud	16.77	21,000
Nathani	6	F5	1	1	Stud	13.98	68,000
Nathani	7	F6	1	1	Stud	13.98	78,000
Nathani	8	F7	1	1	Stud	11.18	266,000
Nathani	9	F8*	1	1	Type B/C	11.18	48,000
Nathani	10	F10	1	1	Stud	8.39	685,000
Nathani	11	F9+	1	1	Stud	8.39	1,150,000
Nathani	12	F11	1	1	Run-Out	6.99	2,000,000
Nathani	13	F12	1	1	Run-Out	5.59	2,512,000
Roderick ⁵	1	R4	2	2	Yield	21.76	49,300
Roderick	2	R1	2	2	Yield	20.30	616,000
Roderick	3	R2	2	2	Yield	20.30	194,110
Roderick	4	R3	2	2	Yield	20.30	190,460
Slutter/Fisher ⁶	1	a3C	1	4	Type B/C	8.00	7,481,100
Slutter/Fisher	2	b3C	1	4	Type B/C	8.00	10,275,900
Slutter/Fisher	3	c3C	1	4	Type B/C	8.00	5,091,200

↓ Continued ↓

Table A-1. Continued...

Reference	Test Number	Specimen Name	No. of Slabs in Test	Studs/Side	Failure Mode	Stress Range (ksi)	N _f (cycles)
Slutter/Fisher	4	a6B	1	4	Type B/C	10.00	962,500
Slutter/Fisher	5	b6B	1	4	Type B/C	10.00	919,100
Slutter/Fisher	6	c6B	1	4	Type B/C	10.00	1,144,600
Slutter/Fisher	7	a6C	1	4	Type B/C	10.00	1,213,600
Slutter/Fisher	8	b6C	1	4	Type B/C	10.00	1,295,300
Slutter/Fisher	9	c6C	1	4	Type B/C	10.00	1,618,900
Slutter/Fisher	10	a2B	1	4	Type B/C	12.00	897,300
Slutter/Fisher	11	b2B	1	4	Type B/C	12.00	565,300
Slutter/Fisher	12	c2B	1	4	Type B/C	12.00	551,100
Slutter/Fisher	13	a4C	1	4	Type B/C	12.00	798,000
Slutter/Fisher	14	b4C	1	4	Type B/C	12.00	1,215,400
Slutter/Fisher	15	c4C	1	4	Type B/C	12.00	1,010,400
Slutter/Fisher	16	P2	1	4	Type B/C	14.00	383,600
Slutter/Fisher	17	a3B	1	4	Type B/C	16.00	139,400
Slutter/Fisher	18	b3B	1	4	Type B/C	16.00	114,700
Slutter/Fisher	19	c3B	1	4	Type B/C	16.00	199,500
Slutter/Fisher	20	a5C	1	4	Type B/C	16.00	335,800
Slutter/Fisher	21	b5C	1	4	Type B/C	16.00	99,200
Slutter/Fisher	22	c5C	1	4	Type B/C	16.00	197,000
Slutter/Fisher	23	P1	1	4	Type B/C	20.00	27,900
Slutter/Fisher	24	a4B	1	4	Type B/C	20.00	41,500
Slutter/Fisher	25	b4B	1	4	Type B/C	20.00	50,700
Slutter/Fisher	26	c4B	1	4	Type B/C	20.00	58,700
Thurlimann ⁷	1	9	2	4	N.S. ¹⁰	20.00	169,000
Thurlimann	2	10	2	4	N.S.	14	474,000
Ovuoba/Prinz ⁸	1	1	2	4	Type C	8.70	12,803,000
Ovuoba/Prinz	2	2	2	4	Run-Out	4.4	30,053,000
Ovuoba/Prinz	3	3	2	4	Run-Out	5.8	12,251,908
Ovuoba/Prinz	4	4	2	4	Run-Out	5.8	20,000,000
Ovuoba/Prinz	5	5	2	4	Run-Out	7.3	31,401,000
Ovuoba/Prinz	6	6	2	4	Run-Out	8.7	30,001,000

¹ Hallam, M.W. (1976) [10]² Lehman, H.G., Lew, H.S., and Toprac, A.A. (1965) [20]³ Mainstone, R.J., and Menzies, J.B. (1967) [19]⁴ Nathini, K.C., Gupta, V.K., and Gadh, A.D. (1988) [21]⁵ Roderick, J.W., and Ansorian, P. (1976) [22]⁶ Slutter, R.G., and Fisher, J.W. (1966) [4]⁷ Thurlimann, B. (1959) [23]⁸ Ovuoba and Prinz (Current test report)⁹ Failure occurred near mid height of stud shank¹⁰ Failure mode not specified

APPENDIX B. CONCRETE CYLINDER FABRICATION AND TESTING

Concrete compressive strength was determined for the slab of each push-out specimen using cylinder compression tests. Concrete cylinders were created and tested from each concrete batch following procedures outlined in the ASTM specifications [27,28]. Because concrete strength can change over time, compressive testing of the concrete cylinders coincided with beginning of each fatigue test. Figure B- 1 shows the test setup used to determine concrete compressive strength, consisting of a Forney concrete compression machine capable of applying 400 kips of axial force. Also shown in Figure B- 1 is the sample concrete cylinder geometry. Note that while the push-out specimens contain two concrete slabs, created from two separate concrete batches, the material strengths provided in Table 1 of Section 2 represent the average concrete strength from both slabs.

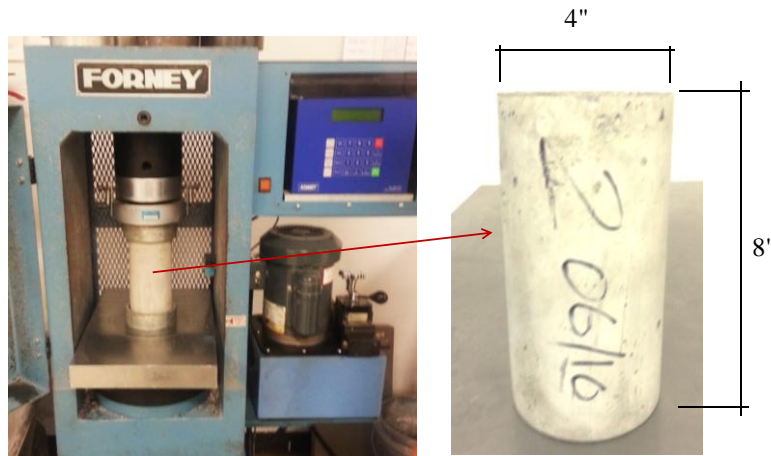
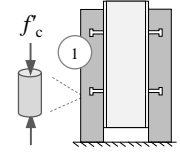
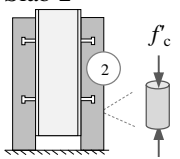


Figure B- 1. Concrete testing machine and cylinder dimensions

Table B-1 shows the strength of each individual concrete sample. In Table B-1 the number of cylinders available for material testing slightly varies between push-out specimens due to the amount of remaining concrete following casting. Note that specimen 1-6 refer to tests described in Chapter 2 and specimen R1, R2, and R3 refer to tests described in Chapter 4.

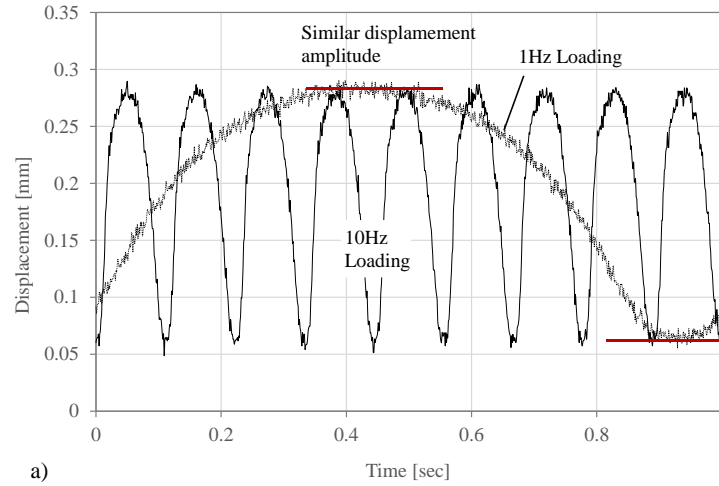
Table B- 1. Concrete compression test data for push-out specimen slabs

		Concrete Compressive Strength, f'_c , ksi								
		1	2	3	4	5	6	R1	R2	R3
Slab 1 		6098	6873	5831	7861	6782	8464	8654	7892	7653
		5575	6781	5896	8209	5909	8037	9100	8200	8093
		--	6841	--	8905	--	7532	9150	8036	7841
		--	6350	--	--	--	--	--	--	--
		--	6920	--	--	--	--	--	--	--
		--	6285	--	--	--	--	--	--	--
Slab 2 		6584	7279	6797	8470	6626	8314	6441	5490	6123
		5453	7212	7094	8238	--	8434	6237	5630	5842
		--	6989	--	8446	--	8237	6164	5802	5750
		--	6996	--	--	--	--	--	--	--
		--	7879	--	--	--	--	--	--	--
		--	7384	--	--	--	--	--	--	--
Average f'_c, MPa		5928	6982	6405	8355	6439	8170	7624	6842	6884

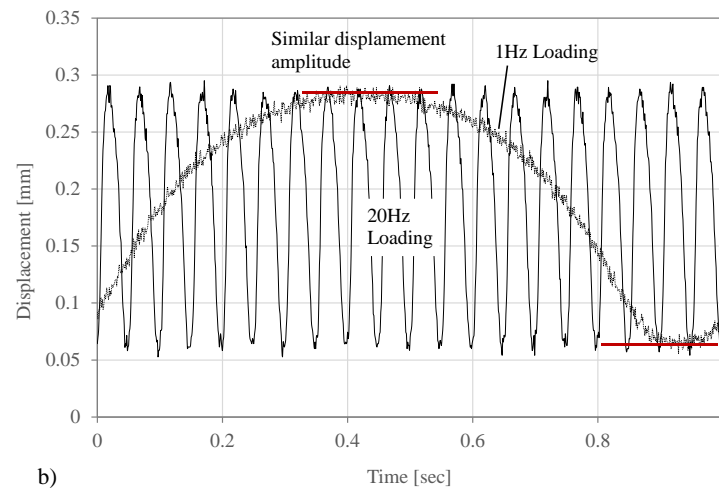
APPENDIX C. VERIFICATION OF NEGLIGIBLE INERTIAL EFFECTS UNDER HIGH FREQUENCY LOADING

To ensure appropriate applied stress ranges in the tests described in Chapter 2, all specimen loads applied in this study are determined by a controlled loop process driven by local load cell measurements (i.e. load controlled testing). Given that the load cell measurements are taken by a device mounted to the moving loading ram, at higher loading frequencies the possibility exists for inertial forces to influence load measurements and therefore the applied specimen loads.

To verify negligible inertial effects at higher frequency loadings and ensure consistency in the applied load across loading rates, the local slab slip response of the push-out specimens are compared under pseudo-static loading frequencies (1Hz) and high frequency loadings (20Hz). All slip measurements are taken from LVDTs locally mounted to the specimens. Figure C-1 shows the resulting slip versus time at 1Hz, 10Hz, and 20Hz loading frequencies for Specimen 5. From Figure C-1, peak displacement measurements remain similar across all loading rates. Assuming that the specimen stiffness remained relatively constant within 1,000 loading cycles, these similar slip readings indicate that the loads applied to the specimens are not influenced by inertial effects from the load cell movement at high frequencies.



a)



b)

Figure C-1. Comparison of slab slip measurements for Specimen 5 during high frequency dynamic loading. Comparisons presented represent (a) 1Hz and 10Hz loading rates, and (b) 1Hz and 20Hz loading rates

APPENDIX D. ADDITIONAL SLIP AND SEPARATION MEASUREMENTS

Slip and separation provide an indication of stud fatigue damage during testing. Figure D-1 provides the slip and separation data for Specimens 1, 3, 4, 5, and 6 as found in Chapter 2. Note that LVDT data for Specimen 2 is not provided as it was lost from the acquisition device during a power outage prior to test completion.

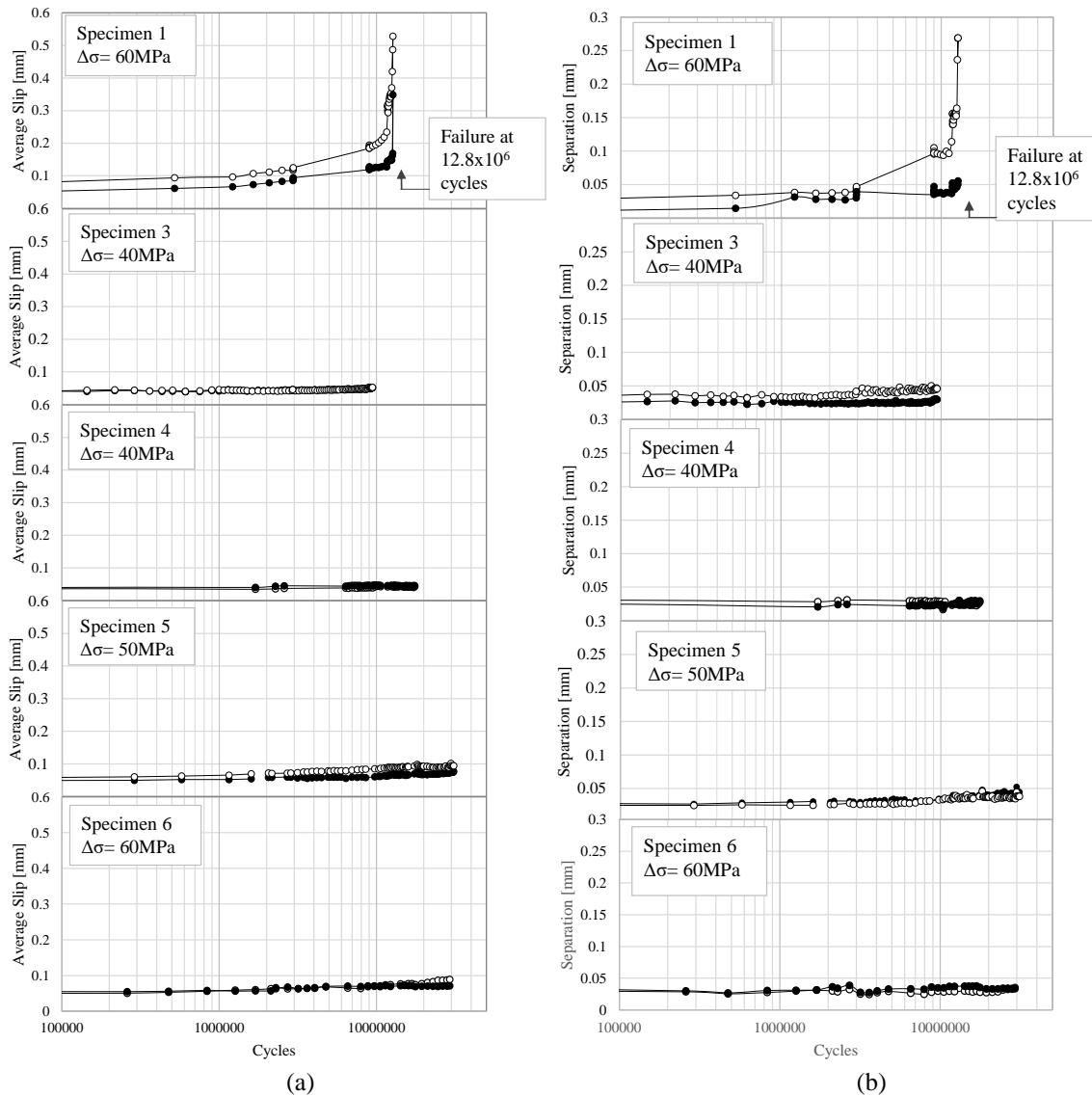
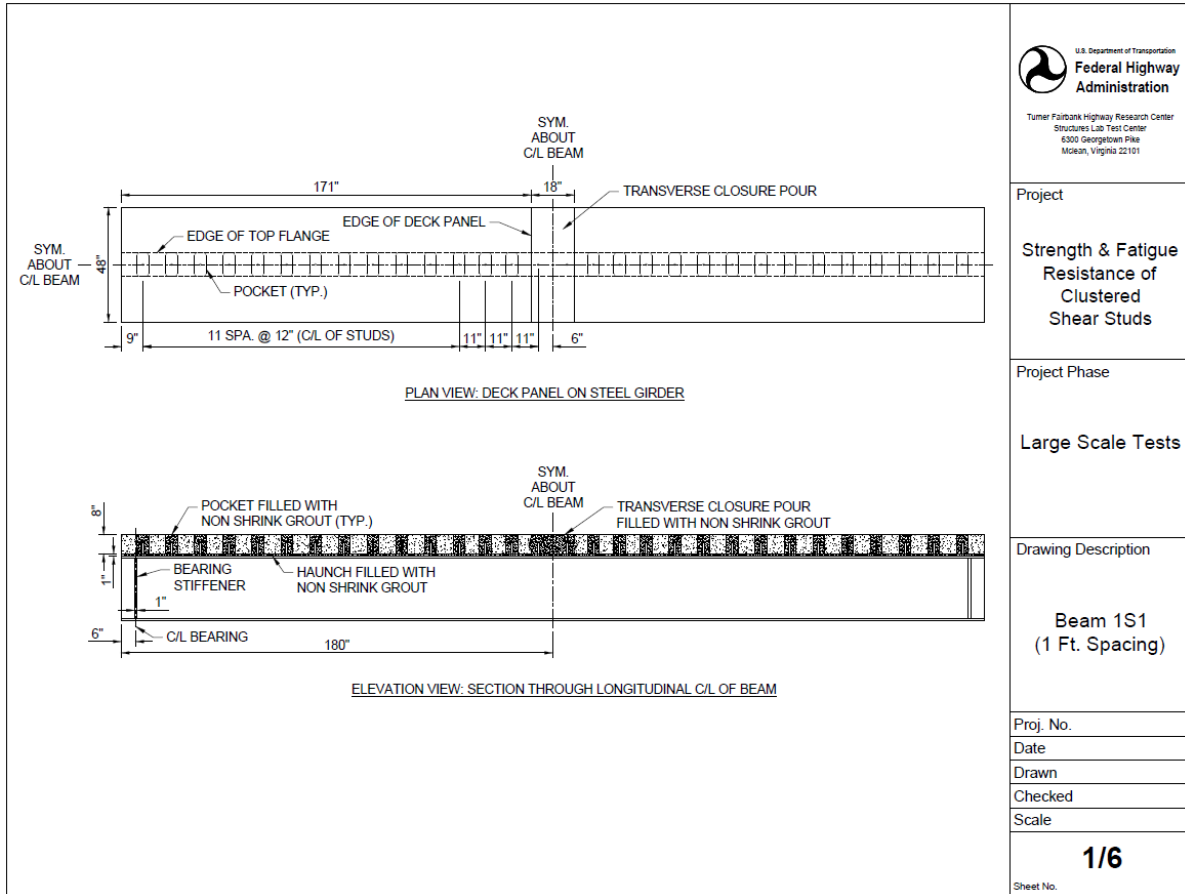


Figure D-1. (a) Slip and (b) separation data from external LVDT measurements

APPENDIX E. TURNER FAIRBANKS HIGHWAY RESEARCH CENTER TEST DETAILS

Below are the drawings provided by the Turner Fairbanks Highway Research Center of the large scale composite beam static tests performed and used to validate the finite element modelling techniques used in Chapter 3.




 U.S. Department of Transportation
Federal Highway Administration
 Turner Fairbanks Highway Research Center
 Structures Lab Test Center
 6300 Georgetown Pike
 Manassas, Virginia 22101

Project

Strength & Fatigue Resistance of Clustered Shear Studs

Project Phase

Large Scale Tests

Drawing Description

**Beam 1S1
(1 Ft. Spacing)**

Proj. No.

Date

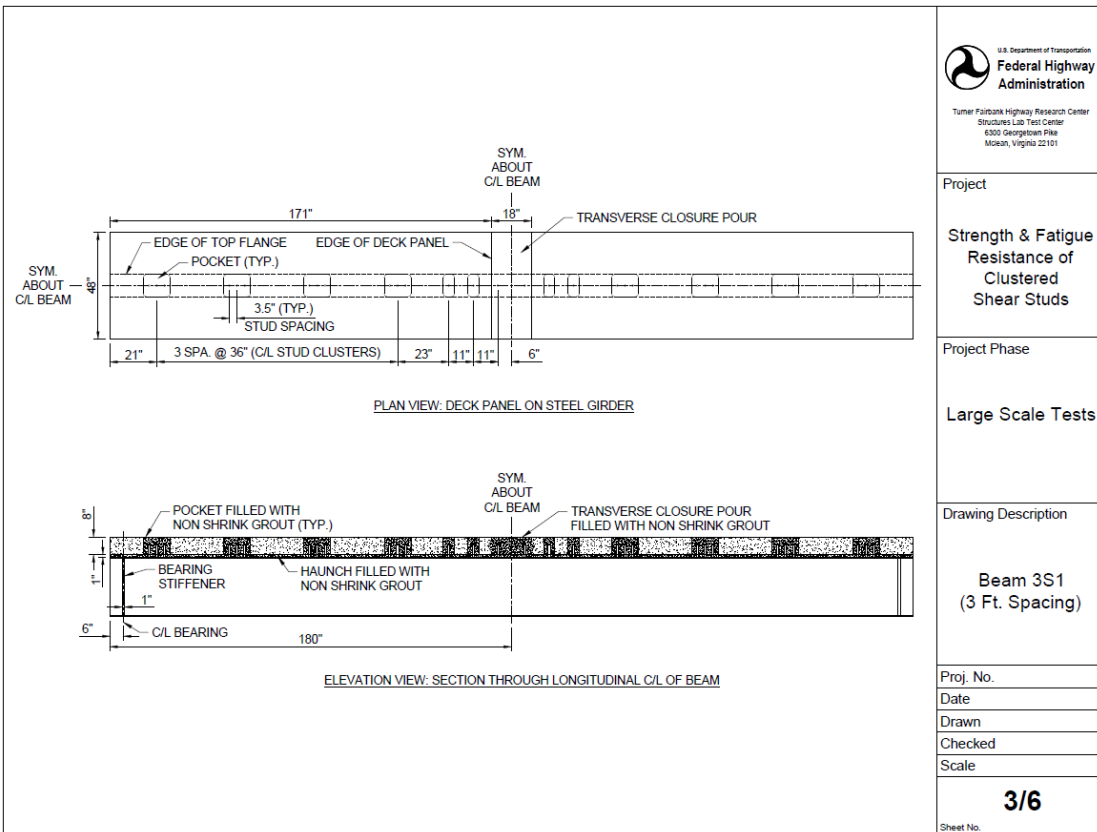
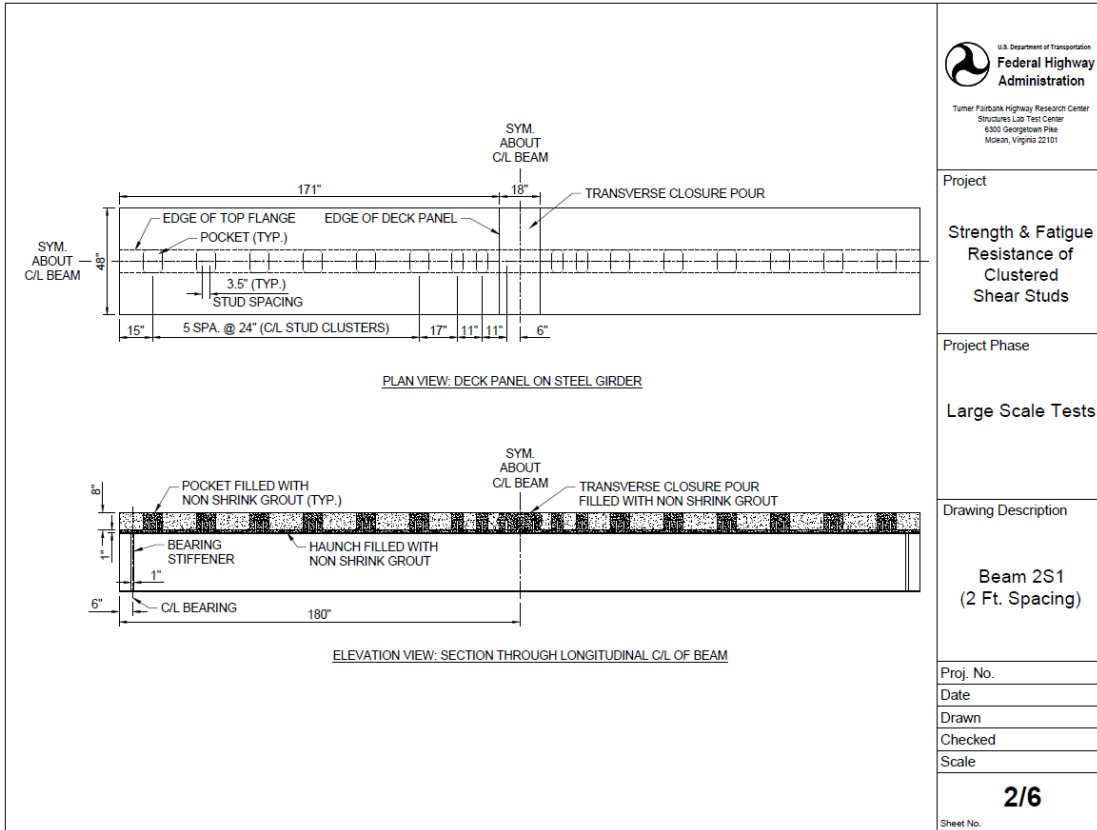
Drawn

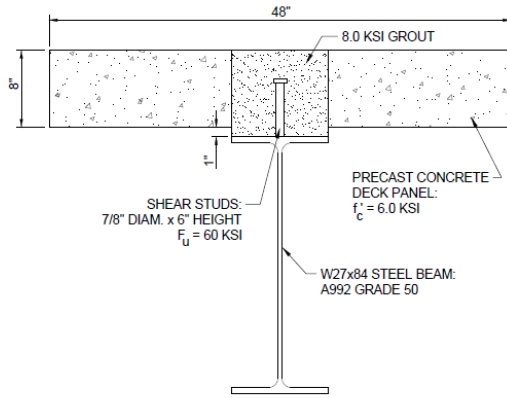
Checked

Scale

1/6

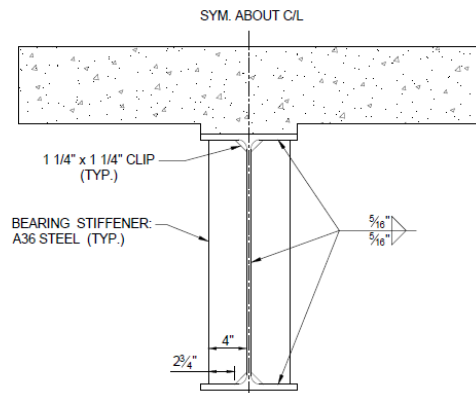
Sheet No.





TYPICAL SECTION AT POCKET

NOTE: CONCRETE DECK REINFORCEMENT NOT SHOWN



TYPICAL SECTION AT BEARING STIFFENERS

Project

Strength & Fatigue Resistance of Clustered Shear Studs

Project Phase

Large Scale Tests

Drawing Description

Typical Sections of all Beams

Proj. No.

Date

Drawn

Checked

Scale

5/6

Sheet No.

Appendix F. Example Design Calculation for Girder

Calculations for girder design used in Chapter 3 were done in accordance with AASHTO [1] specifications with the exception of the loading distribution factors. Load distribution factors were kept constant at the values of 0.61 for the moment distribution factor, 0.88 for the shear distribution factor, and 0.33 for the fatigue distribution factor, as shown in the example below. These factors were kept constant for consistency in load application across all finite element models. During design, checks were performed to ensure the sizing of both the girder and deck meet moment, shear, and service demands. The following pages step through the process of designing girders for composite action.

Load Modifiers

A 1.3.3-1.3.5

The load modifiers for this bridge for Strength limit states are:

$\eta_D := 1.00$	Ductility
$\eta_R := 1.00$	Redundancy
$\eta_O := 1.00$	Operational Importance
$\eta := \eta_D \cdot \eta_R \cdot \eta_O = 1.00$	Total

1 - Material Properties

$F_y := 50 \text{ ksi}$	AASHTO M270, Grade 50W	A 6.4.1
$E_s := 29000 \text{ ksi}$	Steel Modulus of Elasticity	A 6.4.1
$\gamma_s := 490 \text{ pcf}$	Steel unit weight	
$f'_c := 4.0 \text{ ksi}$	Compressive strength of deck	
$E_c = 3640 \text{ ksi}$	Concrete Modulus of Elasticity	A Eq C5.4.2.4-1
$\gamma_c := 150 \text{ pcf}$	Concrete unit weight	
$n := 8$	Modular ratio	A C6.10.1.1.1b

2 - Bridge Geometry

Bridge geometry for deck design:

$L := 100 \text{ ft}$	Span length
$W_{\text{bridge}} := 43.5 \text{ ft}$	Total bridge width
$W_{\text{road}} := 40 \text{ ft}$	Total roadway width
$S := 9.0 \text{ ft}$	Beam spacing
$N_b := 5$	Number of beams
$w_{\text{OH}} := 3.75 \text{ ft}$	Overhang width
$\theta := 0 \text{ deg}$	Skew of bridge

3 - Girder Properties

The sizes of the plates that make up the girders must be defined and then a variety of section properties can be calculated. The several AASHTO limits on girder proportions will also be checked.

3.1a - Girder Section Definition

The sizes of the girder components at midspan are defined below.

$D := 40 \text{ in}$	Web depth
$t_w := \frac{5}{8} \text{ in}$	Web thickness
$b_c := 16 \text{ in}$	Width of top compression flange
$t_c := 1.5 \text{ in}$	Thickness of top compression flange
$b_t := 16 \text{ in}$	Width of bottom tension flange
$t_t := 1.5 \text{ in}$	Thickness of bottom tension flange

3.1b - Deck Section Definition

The size of the deck

$t_s := 10 \text{ in}$	Actual total deck thickness
$t_{cws} := 0.5 \text{ in}$	Thickness of wearing surface
$t_{str} := t_s - t_{cws} = 9.50 \text{ in}$	Structural deck thickness reduced for thickness of wearing surface
$t_{haunch} := 3 \text{ in}$	Thickness of haunch used for dead load but is conservatively assumed to be zero for calculation of section properties

Effective Slab Width:

The effective slab width for composite action with the girders

$b_{s,int} := S = 108.00 \text{ in}$	Effective slab width for an interior girder	A 6.2.6.1
$b_{s,ext} := \frac{S}{2} + w_{OH} = 99.00 \text{ in}$	Effective slab width for a fascia girder	A 6.2.6.1

3.2 - Calculate Section Properties

Section properties are needed. First, the bare section properties of the girder are found, then the long term composite properties, and finally the short term composite properties. The composite properties are calculated for an interior girder.

3.2.1 - Bare Girder - Non-Composite Properties

Calculations for the section properties are carried out in the Excel table below

$$A_{ncd} := b_t \cdot t_t + D \cdot t_w + b_c \cdot t_c = 73.00 \text{ in}^2$$

$$y_{ncd} := \frac{b_t \cdot t_t \cdot \frac{t_t}{2} + D \cdot t_w \cdot \left(t_t + \frac{D}{2}\right) + b_c \cdot t_c \cdot \left(t_t + D + \frac{t_c}{2}\right)}{A_{ncd}} = 21.50 \text{ in}$$

$$d_{ncd} := t_c + D + t_t = 43.00 \text{ in}$$

$$I_1 := \frac{t_w \cdot D^3}{12} + \frac{b_c \cdot t_c^3}{12} + \frac{b_t \cdot t_t^3}{12} = 3342.33 \text{ in}^4$$

$$I_2 := b_t \cdot t_t \cdot \left(y_{ncd} - \frac{t_t}{2}\right)^2 + b_c \cdot t_c \cdot \left(t_t + D + \frac{t_c}{2} - y_{ncd}\right)^2 + D \cdot t_w \cdot \left(t_t + \frac{D}{2} - y_{ncd}\right)^2 = 20667.00 \text{ in}^4$$

$$I_{ncd} := I_1 + I_2 = 24009.33 \text{ in}^4$$

From these calculations

$$\begin{aligned}
 y_{ncd} &= 21.50 \text{ in} && \text{Distance from bottom of girder to neutral axis} \\
 A_{ncd} &= 73.00 \text{ in}^2 && \text{Gross area of cross section} \\
 I_{ncd} &= 24009.33 \text{ in}^4 && \text{Moment of inertia of the section} \\
 d_{ncd} &= 43.00 \text{ in} && \text{Total girder depth}
 \end{aligned}$$

The section modulus at extreme fiber of the compression (top) and tension (bottom) flange will also be needed and are

$$S_{ncd,t} := \frac{I_{ncd}}{y_{ncd}} = 1116.71 \text{ in}^3 \qquad S_{ncd,c} := \frac{I_{ncd}}{d_{ncd} - y_{ncd}} = 1116.71 \text{ in}^3$$

3.2.2 - Interior Girder - Long Term Composite Properties

$$A_{ltc} := A_{ncd} + \frac{S}{3 \cdot n} \cdot t_{str} = 115.75 \text{ in}^2$$

$$y_{ltc} := \frac{A_{ncd} \cdot y_{ncd} + \frac{S}{3 \cdot n} \cdot t_{str} \cdot \left(d_{ncd} + \frac{t_s}{2} \right)}{A_{ltc}} = 31.29 \text{ in}$$

$$I_{ltc} := I_{ncd} + A_{ncd} \cdot d_{ncd}^2 + \frac{S}{12} \cdot t_{str}^3 + \frac{S}{3 \cdot n} \cdot t_{str} \cdot \left(d_{ncd} + \frac{t_{str}}{2} - y_{ltc} \right)^2 = 170894.04 \text{ in}^4$$

From these calculations:

$$\begin{aligned}
 y_{ltc} &= 31.29 \text{ in} && \text{Distance from bottom of girder to neutral axis} \\
 A_{ltc} &= 115.75 \text{ in}^2 && \text{Gross area of the cross section} \\
 I_{ltc} &= 170894.04 \text{ in}^4 && \text{Moment of inertia of the section}
 \end{aligned}$$

The section modulus at extreme fiber of the compression (top) and tension (bottom) flange will also be needed and are

$$S_{ltc,t} := \frac{I_{ltc}}{y_{ltc}} = 5462.10 \text{ in}^3 \qquad S_{ltc,c} := \frac{I_{ltc}}{d_{ncd} - y_{ltc}} = 14590.44 \text{ in}^3$$

The section modulus at extreme fiber of the deck slab is

$$S_{ltc,s} := \frac{I_{ltc}}{d_{ncd} + t_{str} - y_{ltc}} = 8056.20 \text{ in}^3$$

3.2.3 - Interior Girder - Short Term Composite Properties

Calculations for the section properties are carried out in the Excel table below

$$A_{stc} := A_{ncd} + \frac{S}{n} \cdot t_{str} = 201.25 \text{ in}^2$$

$$y_{stc} := \frac{A_{ncd} \cdot y_{ncd} + \frac{S}{n} \cdot t_{str} \cdot \left(d_{ncd} + \frac{t_{str}}{2} \right)}{A_{stc}} = 38.23 \text{ in}$$

$$I_{stc} := I_{ncd} + A_{ncd} \cdot (y_{stc} - y_{ncd})^2 + \frac{\left(\frac{S}{n} \right) \cdot t_{str}^3}{12} + \left(\frac{S}{n} \right) \cdot t_{str} \cdot \left(d_{ncd} + \frac{t_{str}}{2} - y_{stc} \right)^2 = 57029.41 \text{ in}^4$$

From these calculations

$y_{stc} = 38.23 \text{ in}$	Distance from bottom of girder to neutral axis
$A_{stc} = 201.25 \text{ in}^2$	Gross area of cross section
$I_{stc} = 57029.41 \text{ in}^4$	Moment of inertia of the section

The section modulus at extreme fiber of the compression (top) and tension (bottom) flange will also be needed and are

$$S_{stc,t} := \frac{I_{stc}}{y_{stc}} = 1491.81 \text{ in}^3 \quad S_{stc,c} := \frac{I_{stc}}{|d_{ncd} - y_{stc}|} = 11951.49 \text{ in}^3$$

The section modulus at extreme fiber of the deck slab is

$$S_{stc,s} := \frac{I_{stc}}{d_{ncd} + t_{str} - y_{stc}} = 3995.97 \text{ in}^3$$

3.3 - Calculate Plastic Moment of Girder

The plastic moment from the composite section will be needed later in the design, and is only dependent on the section properties. The plastic moment is found as outlined in AASHTO Appendix D6, Table D6.1-1.

The plastic forces in the various components are needed and are found first

$P_s := 0.85 \cdot f'_c \cdot b_{s,int} \cdot t_{str} = 3488.40 \text{ kip}$	Slab plastic force
$P_c := F_y \cdot b_c \cdot t_c = 1200.00 \text{ kip}$	Top flange plastic force
$P_w := F_y \cdot D \cdot t_w = 1250.00 \text{ kip}$	Web plastic force
$P_t := F_y \cdot b_t \cdot t_t = 1200.00 \text{ kip}$	Bottom flange plastic force

3.2.1 - Find Location of Plastic Neutral Axis (PNA)

Table D6.1-1 lists seven possible locations for the PNA. The longitudinal reinforcing steel in the deck is conservatively ignored for this design, which simplifies the table to three cases which are analyzed

CASE 1 - if true, the PNA is located in the girder web

$$P_t + P_w \geq P_c + P_s$$

CASE 2 - if true, the PNA is located in the top flange

$$P_t + P_w + P_c \geq P_s$$

CASE 3 - if true, the PNA is located in the deck slab

$$P_t + P_w + P_c < P_s$$

The true case is found below

<pre> case := if P_t + P_w ≥ P_c + P_s return 1 else if P_t + P_w + P_c ≥ P_s return 2 else if P_t + P_w + P_c < P_s return 3 </pre>	<p>case = 2</p>
--	-----------------

There is a different equation provided in Table D6.1-1 for finding the exact location of the PNA depending on the PNA location. The exact location is found below

<pre> Y := if case = 1 return $\frac{D}{2} \cdot \left(\frac{P_t - P_c - P_s}{P_w} + 1 \right)$ else if case = 2 return $\frac{t_c}{2} \cdot \left(\frac{P_w + P_t - P_s}{P_c} + 1 \right)$ else if case = 3 return $t_s \cdot \left(\frac{P_c + P_w + P_t}{P_s} \right)$ </pre>	<p>Y = 0.10 in</p>
---	--------------------

This distance 'Y' is measured from a different part of the girder depending on the case. The distance from the bottom of girder to the PNA is desired

<pre> PNA := if case = 1 return t_t + D - Y else if case = 2 return t_t + D + t_c - Y else if case = 3 return t_t + D + t_c + t_s - Y </pre>	<p>PNA = 42.90 in</p>
---	-----------------------

The depth of the web in compression at the plastic moment is needed later and is found based on the location of the PNA

$$D_{cp} := \text{if case} = 1 \quad \left\{ \begin{array}{l} \text{return } t_t + D - \text{PNA} \\ \text{else} \\ \text{return } 0 \text{ in} \end{array} \right. \quad D_{cp} = 0.00 \text{ in}$$

The plastic moment is the sum of the moments of each of the plastic forces about the PNA. The moment arm to the center of each segment of the cross section is found first and then the plastic moment is calculated depending on the case

$$d_t := \text{PNA} - \frac{t_t}{2} = 42.15 \text{ in} \quad \text{Distance from PNA to center of bottom flange}$$

$$d_w := \text{PNA} - t_t - \frac{D}{2} = 21.40 \text{ in} \quad \text{Distance from PNA to center of web}$$

$$d_c := \left| \text{PNA} - t_t - D - \frac{t_c}{2} \right| = 0.65 \text{ in} \quad \text{Distance from PNA to center of top flange}$$

$$d_s := \left| \text{PNA} - t_t - D - t_c - \frac{t_s}{2} \right| = 5.10 \text{ in} \quad \text{Distance from PNA to center of deck slab}$$

Plastic Moment

$$M_p := \text{if case} = 1 \quad \left\{ \begin{array}{l} \text{return } \frac{P_w}{2D} \cdot \left((Y^2 + (D - Y)^2) \right) + P_s \cdot d_s + P_c \cdot d_c + P_t \cdot d_t \\ \text{else if case} = 2 \\ \text{return } \frac{P_c}{2 \cdot t_c} \cdot \left((Y^2 + (t_c - Y)^2) \right) + P_s \cdot d_s + P_w \cdot d_w + P_t \cdot d_t \\ \text{else if case} = 3 \\ \text{return } \frac{Y^2 \cdot P_s}{2 t_s} + P_c \cdot d_c + P_w \cdot d_w + P_t \cdot d_t \end{array} \right.$$

$$M_p = 7992.40 \text{ kip} \cdot \text{ft}$$

3.4 - Check Geometric Limits (OKAY if 1)

AASHTO defines a number of limits for the proportions of girders which must be checked

3.4.1 - Check Cross Section Limits

Check Web Slenderness

Webs without longitudinal stiffeners shall satisfy

$$\frac{D}{t_w} \leq 150 \quad \text{A Eq 6.10.2.1.1-1}$$

$$\frac{D}{t_w} = 64.00$$

$$\frac{D}{t_w} \leq 150 = 1.00 \quad \text{OKAY}$$

Check Flange Proportions

AASHTO provides four checks for flange proportions

$$\frac{b_f}{2 t_f} \leq 12.0 \quad \text{A Eq 6.10.2.2-1}$$

$$b_f \geq \frac{D}{6} \quad \text{A Eq 6.10.2.2-2}$$

$$t_f \geq 1.1 t_w \quad \text{A Eq 6.10.2.2-3}$$

$$0.1 \leq \frac{I_{yc}}{I_{yt}} \leq 10 \quad \text{A Eq 6.10.2.2-4}$$

Top flange check:

$$b_c = 16.00 \text{ in} \quad b_t = 16.00 \text{ in} \quad t_c = 1.50 \text{ in} \quad t_t = 1.50 \text{ in}$$

$$\frac{b_c}{2 t_c} = 5.33 \quad \frac{b_c}{2 t_c} \leq 12 = 1.00 \quad \text{OKAY}$$

$$\frac{D}{6} = 6.67 \text{ in} \quad b_c \geq \frac{D}{6} = 1.00 \quad \text{OKAY}$$

$$1.1 t_w = 0.69 \text{ in} \quad t_c \geq 1.1 t_w = 1.00 \quad \text{OKAY}$$

Bottom flange check:

$$\frac{b_t}{2 t_t} = 5.33 \quad \frac{b_t}{2 t_t} \leq 12 = 1.00 \quad \text{OKAY}$$

$$\frac{D}{6} = 6.67 \text{ in} \quad b_t \geq \frac{D}{6} = 1.00 \quad \text{OKAY}$$

$$1.1 t_w = 0.69 \text{ in} \quad t_t \geq 1.1 t_w = 1.00 \quad \text{OKAY}$$

Ratio between top and bottom flanges' moment of inertia about a vertical axis is checked

$$I_{yc} := \frac{t_c \cdot b_c^3}{12} = 512.00 \text{ in}^4 \quad I_{yt} := \frac{t_t \cdot b_t^3}{12} = 512.00 \text{ in}^4$$

$$\frac{I_{yc}}{I_{yt}} = 1.00 \quad 0.1 \leq \frac{I_{yc}}{I_{yt}} \leq 10 = 1.00 \quad \text{OKAY}$$

3.4.2 - Check Section Ductility

The following check must be satisfied to prevent the concrete deck from crushing prematurely

$$D_p \leq 0.42 D_t$$

$$D_t := d_{ncd} + t_{str} = 52.50 \text{ in}$$

$$D_p := D_t - \text{PNA} = 9.60 \text{ in}$$

$$D_p \leq 0.42 D_t = 1.00 \quad \text{OKAY}$$

3.4.3 - Check for Section Compactness

AASHTO specifies three criteria that must be satisfied for the section to be considered compact

$$F_y \leq 70 \text{ ksi} \quad \text{Criteria 1} \quad \text{A 6.10.6.2.2}$$

$$\frac{D}{t_w} \leq 150 \quad \text{Criteria 2} \quad \text{A 6.10.2.1.1}$$

$$\frac{2 D_{cp}}{t_w} \leq 3.76 \cdot \sqrt{\frac{E_s}{F_y}} \quad \text{Criteria 3} \quad \text{A Eq 6.10.6.2.2-1}$$

$$\frac{2 D_{cp}}{t_w} = 0.00 \quad 3.76 \cdot \sqrt{\frac{E_s}{F_y}} = 90.55$$

```

compact := if  $F_y > 70 \text{ ksi}$ 
    || return 0
    also if  $\frac{D}{t_w} > 150$ 
    || return 0
    also if  $2 \cdot \frac{D_{cp}}{t_w} > 3.76 \cdot \sqrt{\frac{E_s}{F_y}}$ 
    || return 0
    else
    || 1

```

A value of 1 below indicates a compact section. A value of 0 indicates a non-compact section

compact = 1.00

4 - Determine Loads and Load Effects

Various loads must be found for the girder design checks, as well as the critical actions of moment and shear. Dead, wind and live loads are calculated

4.1 - Dead Loads

The dead loads for the various parts of the structure are found

4.1.1 - Dead Load DC

The weight of components and attachments, DC, are found. These loads will be used to find the dead load shear and moment in the structure.

Girder Weight

$$w_{\text{girder}} := A_{\text{net}} \cdot \gamma_s = 248.40 \frac{\text{lb}}{\text{ft}} \quad \text{new section weight per foot girder}$$

Other Calculated Weights

$$w_{\text{deck}} := \gamma_c \cdot S \cdot t_s = 1125.00 \frac{\text{lb}}{\text{ft}} \quad \text{deck weight per foot girder}$$

$$w_{\text{haunch}} := \gamma_c \cdot (t_{\text{haunch}} - t_c) \cdot b_c = 25.00 \frac{\text{lb}}{\text{ft}} \quad \text{haunch weight per foot girder}$$

$$w_{\text{SIP}} := 13 \text{ psf} \cdot S = 117.00 \frac{\text{lb}}{\text{ft}} \quad \text{SIP weight per foot girder}$$

Connection Plates and Cross Frames

$$t_{\text{cp}} := \frac{1}{2} \text{ in} \quad b_{\text{cp}} := 8 \text{ in} \quad \text{thickness/width of connection plate}$$

$$w_{\text{cp}} := t_{\text{cp}} \cdot b_{\text{cp}} \cdot D \cdot \gamma_s = 45.37 \text{ lb} \quad \text{weight of connection plate}$$

Bridge 1 Design Calculation

Cross frames will be spaced evenly at 28', configured in an "X" shape with two diagonals and a bottom chord. 4"x4"x1/2" angles will be used for all three chords.

$$\omega_{\text{angles}} := 12.8 \cdot \frac{\text{lb}}{\text{ft}} \quad \text{per AISC}$$

$$D = 3.33 \text{ ft} \quad S = 9.00 \text{ ft}$$

$$L_{\text{angles}} := \sqrt{S^2 + D^2} \cdot 2 + S = 28.19 \text{ ft}$$

$$w_{\text{angles}} := \omega_{\text{angles}} \cdot L_{\text{angles}} = 360.89 \text{ lb}$$

$$N_{\text{xf}} := 4$$

$$w_{\text{xf}} := \frac{(w_{\text{cp}} \cdot 2 + w_{\text{angles}}) \cdot N_{\text{xf}}}{L} = 18.07 \frac{\text{lb}}{\text{ft}} \quad \text{cross frame weight per foot girder}$$

$$w_{\text{barrier}} := \frac{534 \frac{\text{lb}}{\text{ft}} \cdot 2}{N_b} = 213.60 \frac{\text{lb}}{\text{ft}} \quad \begin{array}{l} \text{barrier weight per foot girder} \\ \text{(assuming jersey barrier along each} \\ \text{fascia, distributed evenly among all} \\ \text{girders).} \end{array}$$

Totals

DC1 = dead loads acting on non-composite section

DC2 = dead loads action on long-term-composite section

$$DC1 := w_{\text{gird}} + w_{\text{deck}} + w_{\text{haunch}} + w_{\text{SIP}} + w_{\text{xf}} = 1533.47 \frac{\text{lb}}{\text{ft}}$$

$$DC2 := w_{\text{barrier}} = 213.60 \frac{\text{lb}}{\text{ft}}$$

4.1.2 - Dead Load DW

The weight of dead load wearing surface and utilities found:

Future Wearing Surface:

$$w_{\text{FWS}} := 25 \frac{\text{lb}}{\text{ft}^2} \cdot \left(\frac{W_{\text{road}}}{N_b} \right) = 200.00 \frac{\text{lb}}{\text{ft}}$$

Lighting Fixtures and Utilities:

A weight is estimated for these potential items.

$$w_{\text{lights}} := 10 \frac{\text{lb}}{\text{ft}}$$

$$w_{\text{util}} := 30 \cdot \frac{\text{lb}}{\text{ft}}$$

Total:

$$DW := w_{\text{lights}} + w_{\text{util}} + w_{\text{FWS}} = 240.00 \frac{\text{lb}}{\text{ft}}$$

Bridge 1 Design Calculation

4.1.3 - Determine Service Dead Load Shears and Moments

Since the girder is simply supported, maximum dead load moment will occur at midspan and maximum shear will occur at the girder end.

Service Dead Load Reactions

$$V_{DC1} := DC1 \cdot \left(\frac{L}{2}\right) = 76.67 \text{ kip}$$

$$V_{DC2} := DC2 \cdot \left(\frac{L}{2}\right) = 10.68 \text{ kip}$$

$$V_{DW} := DW \cdot \left(\frac{L}{2}\right) = 12.00 \text{ kip}$$

Service Dead Load Moments

$$M_{DC1} := \frac{DC1 \cdot L^2}{8} = 1916.84 \text{ kip} \cdot \text{ft}$$

$$M_{DC2} := \frac{DC2 \cdot L^2}{8} = 267.00 \text{ kip} \cdot \text{ft}$$

$$M_{DW} := \frac{DW \cdot L^2}{8} = 300.00 \text{ kip} \cdot \text{ft}$$

4.2 - Wind Load

For girder design, wind load acting on the face of a girder causes lateral stresses to develop in the flanges of the girder. The wind load acting on a girder face is found and then distributed evenly to the top and bottom flanges. Then the lateral flange bending stress due to the load is found.

4.2.1 - Wind Load WS:

The surface pressure caused by wind is found as:

$$P_D := P_B \cdot (V_{DZ})^2 \quad \text{A Eq 3.8.1.2.1-1}$$

$$P_B := 0.05 \cdot \frac{\text{kip}}{\text{ft}^2} \quad \text{for beams} \quad \text{A T3.8.1.2.1-1}$$

$$V_B := 100 \text{ mph} \quad \text{A 3.8.1.1}$$

Assuming the superstructure is less than 30 feet above the ground, the wind velocity is taken as 100 mph:

$$V_{DZ} := 100 \text{ mph} \quad \text{A 3.8.1.1-1}$$

Bridge 1 Design Calculation

$$P_D := P_B \cdot \left(\frac{V_{DZ}}{V_B} \right)^2 = 50.00 \frac{\text{lb}}{\text{ft}^2}$$

For lateral load that contributes to flange bending stresses, only half of the girder height is used.

$$h_{\text{exp}} := \frac{d_{\text{ncd}}}{2} = 1.79 \text{ ft}$$

The resulting wind force per linear foot of flange is:

$$w_1 := P_D \cdot h_{\text{exp}} = 89.58 \frac{\text{lb}}{\text{ft}}$$

However, Article 3.8.1.2.1 states that the total wind load be at least 300 lb/ft:

$$w_2 := \frac{1}{2} \cdot 300 \cdot \frac{\text{lb}}{\text{ft}} = 150.00 \frac{\text{lb}}{\text{ft}}$$

Select the maximum of the two provides wind load force along a flange:

$$WS := \max(w_1, w_2) = 150.00 \frac{\text{lb}}{\text{ft}}$$

4.2.2 Determine Service Wind Load Lateral Moment:

The bottom flange acts as a continuous beam with each cross frame acting as a support. For lateral loads uniformly distributed along the length of a flange, AASHTO Commentary 6.10.3.4 provides the following estimate of the maximum lateral bending moment:

$$M_{w,\text{lat}} := \frac{F_{\text{lat}} \cdot L_b^2}{12} \quad \text{A Eq C6.10.3.4-2}$$

$$F_{\text{lat}} := WS = 150.00 \frac{\text{lb}}{\text{ft}}$$

$$L_b := 28 \text{ ft} \quad \text{cross frame spacing}$$

$$M_{w,\text{lat}} := \frac{F_{\text{lat}} \cdot L_b^2}{12} = 9.80 \text{ kip} \cdot \text{ft}$$

4.3 - Live Load

Live load shear and moment are first found on a per lane basis. The amount of the live load that is applied to a single girder is found later.

4.3.1 - Determine Service Live Load Shear and Moments

Shear is a maximum at the girder end and will be found at that location only. Moment due to live load will be found at midspan.

Axle Loads for HL-93 Truck

$$P_{\text{HL93.1}} := 32 \text{ kip}$$

A F3.6.1.2.2-1

$$P_{\text{HL93.2}} := 32 \text{ kip}$$

$$P_{\text{HL93.3}} := 8 \text{ kip}$$

Bridge 1 Design Calculation

Axle Loads for Tandem Truck

$$P_{\text{tan.1}} := 25 \text{ kip} \quad \text{A 3.6.1.2.3}$$

$$P_{\text{tan.2}} := 25 \text{ kip}$$

Lane Load to be applied with Either Truck

$$W_{\text{lane}} := 640 \frac{\text{lb}}{\text{ft}} \quad \text{A 3.6.1.2.4}$$

Service Live Load Reactions

The live load reaction will be found for the lane load, the HL-93 truck, and the tandem:

$$R_{\text{lane}} := W_{\text{lane}} \cdot \frac{L}{2} = 32.00 \text{ kip} \quad \text{per lane}$$

For the HL-93 truck, the reaction is maximized when the rear axle is at the girder end and the other axles are as close as possible to girder end.

$$R_{\text{HL93}} := P_{\text{HL93.1}} + P_{\text{HL93.2}} \cdot \left(\frac{L - 4 \text{ ft}}{L} \right) + P_{\text{HL93.3}} \cdot \left(\frac{L - 28 \text{ ft}}{L} \right) = 68.48 \text{ kip} \quad \text{per lane}$$

For the tandem, the reaction is maximized with one axle at the girder end and the other axle on the span:

$$R_{\text{tan}} := P_{\text{tan.1}} + P_{\text{tan.2}} \cdot \left(\frac{L - 4 \text{ ft}}{L} \right) = 49.00 \text{ kip} \quad \text{per lane}$$

The maximum service live load reaction for design is:

$$R_{\text{LL}} := \max(R_{\text{HL93}}, R_{\text{tan}}) + R_{\text{lane}} = 100.48 \text{ kip} \quad \text{per lane}$$

Service Live Load Moment

The live load moments will be found at midspan

$$M_{\text{lane}} := \frac{W_{\text{lane}} \cdot L^2}{8} = 800.00 \text{ kip} \cdot \text{ft} \quad \text{per lane}$$

For the HL-93 truck, the middle axle will be placed at midspan and the other axles as close as possible:

$$M_{\text{HL93}} := \frac{P_{\text{HL93.2}} \cdot L}{4} + \frac{P_{\text{HL93.1}}}{2} \cdot \left(\frac{L}{2} - 14 \text{ ft} \right) + \frac{P_{\text{HL93.3}}}{2} \cdot \left(\frac{L}{2} - 14 \text{ ft} \right) = 1520.00 \text{ kip} \cdot \text{ft}$$

For the tandem, one axle will be placed 2' left of midspan and the other 2' right of midspan:

$$M_{\text{tan}} := 2 \cdot P_{\text{tan.1}} \cdot \left(\frac{L - 4 \text{ ft}}{4} \right) = 1200.00 \text{ kip} \cdot \text{ft} \quad \text{per lane}$$

The maximum service live load moment at midspan is:

$$M_{\text{LL}} := \max(M_{\text{HL93}}, M_{\text{tan}}) + M_{\text{lane}} = 2320.00 \text{ kip} \cdot \text{ft} \quad \text{per lane}$$

Bridge 1 Design Calculation

4.3.2 - Dynamic Load Allowance

The dynamic load allowance, or impact factor, increases the action of live load trucks to approximate the dynamic effects of a quickly applied load. The factor varies depending on the component and limit state

$IM_d := 75\%$	Deck Joints	A 3.6.2.1
$IM_f := 15\%$	Fatigue and Fracture	
$IM := 33\%$	Girders	

4.4 - Live Load Distribution Factors

Live loads per lane may be distributed to the girders using the approximate factors from AASHTO chapter 4. There are different factors depending on the force effect and the limit state. The various factors are found for use later in the design checks

4.4.2 - Distribution Factor for Moment

The distribution factor is usually calculated based on section properties. In this case, in order to decrease the number of variables, ONE distribution factor was used for all girders. It is calculated below.

Simplified value used to replace Kg term:

$$u := 1.02$$

Table 4.6.2.2.1-2

$$DF_m := 0.075 + \left(\frac{S}{9.5 \text{ ft}}\right)^{0.6} \cdot \left(\frac{S}{200 \text{ ft}}\right)^{0.2} \cdot u = 0.61$$

4.4.3 - Distribution Factor for Shear

The bridge qualifies for use of the distribution factor based on preceding checks. The shear distribution factor is found similarly to the moment

For one lane loaded

$$DF_{v1} := 0.36 + \frac{S}{25 \text{ ft}} = 0.72 \quad \text{lanes/beam}$$

For more than one lane loaded

$$DF_{v2} := 0.2 + \frac{S}{12 \text{ ft}} - \left(\frac{S}{35 \text{ ft}}\right)^{2.0} = 0.88 \quad \text{lanes/beam}$$

Controlling distribution factor is

$$DF_v := \max(DF_{v1}, DF_{v2}) = 0.88 \quad \text{lanes/beam}$$

Bridge 1 Design Calculation

4.4.4 - Fatigue Load Distribution Factor

For the fatigue limit state, only a single truck is used. Therefore, the fatigue factor is the moment distribution factor for a single lane loaded, but the MPF implicit to the moment distribution factor must be divided out.

$$DF_{m1} := 0.06 + \left(\frac{S}{14 \text{ ft}}\right)^{0.4} \cdot \left(\frac{S}{200 \text{ ft}}\right)^{0.3} \cdot 1.02 = 0.40$$

$$DF_{m.fat} := \frac{DF_{m1}}{1.2} = 0.33 \quad \text{lanes/beam}$$

4.4.5 - Summary of Distribution Factors for Live Load

For the strength and service limit states
(in lanes/beam)

$$DF_m = 0.61$$

$$DF_v = 0.88$$

For the fatigue limit state
(lanes/beam)

$$DF_{m.fat} = 0.33$$

5 - Evaluate Strength 1 Limit State

This limit state represents the maximum load the girder is likely to see in its lifetime, and deformation is permitted (plastification) so long as the section components will not buckle first. Thus, the strength of the section for this limit state is affected by compactness

Bending at midspan will be checked first and then shear at a support will be checked.

$$\phi_f := 1.00$$

phi factor for flexure

A 6.5.4.2

$$\phi_v := 1.00$$

phi factor for shear

For the Strength 1 Limit State the load factors are

$$\gamma_{DC} := 1.25$$

$$\gamma_{DW} := 1.50$$

$$\gamma_{LL} := 1.75$$

$$\gamma_{WS} := 0.00$$

A T3.4.1-1

5.1 - Bending Strength Checks

The strength depends on the section compactness and other criteria and other criteria. Checks are shown for both a compact section and for a non-compact section. The flowcharts in AASHTO Appendix C6, Figure C6.4.4-1 and Figure C6.4.5-1 are followed for these calculations.

Limiting criteria is

$$M_u + \frac{1}{3} \cdot f_{lat} \cdot S_{xt} \leq \phi_f \cdot M_n$$

A Eq 6.10.7.1.1-1

Factored Moment

Maximum Strength 1 moment at midspan is:

$$M_u := \eta \cdot (\gamma_{DC} \cdot (M_{DC1} + M_{DC2}) + \gamma_{DW} \cdot M_{DW} + \gamma_{LL} \cdot M_{LL} \cdot (1 + IM) \cdot DF_m)$$

$$M_u = 6452.47 \text{ kip} \cdot \text{ft}$$

Bridge 1 Design Calculation

Strength 1 lateral moment due to wind

$$M_{STR.3.lat} := \eta \cdot (\gamma_{WS} \cdot M_{w.lat}) = 0.00 \text{ kip} \cdot \text{ft}$$

$$f_{lat} := 0 \text{ ksi} \quad \text{since the lateral moment is zero}$$

Compact Section Bending Strength

The compact section bending strength calculation is dependent on the depth of web in compression at plastic moment, D_p .

$M_n := \begin{cases} \text{return } M_p & \text{if } D_p \leq 0.1 \cdot D_t \\ \text{return } M_p \cdot \left(1.07 - 0.7 \cdot \frac{D_p}{D_t} \right) & \text{else if } D_p > 0.1 \cdot D_t \end{cases}$		$M_n = 7528.74 \text{ kip} \cdot \text{ft}$ <p><u>Criteria Check (OKAY if 1)</u></p> $M_u \leq \phi_r \cdot M_n = 1.00 \quad \text{OKAY}$
---	--	---

5.2 - Shear Strength Check

Shear checked at supports.

Limiting criteria

$$V_u \leq \phi_v \cdot V_n \quad \text{A Eq 6.10.9.1-1}$$

Factored Force

$$V_u := \eta \cdot (\gamma_{DC} \cdot (V_{DC1} + V_{DC2}) + \gamma_{DW} \cdot V_{DW} + \gamma_{LL} \cdot R_{LL} \cdot (1 + IM) \cdot DF_v)$$

$$V_u = 333.90 \text{ kip}$$

Nominal Shear Strength

$$V_n := C \cdot V_p \quad \text{A Eq 6.10.9.2-1}$$

$$k_w := 5.0 \quad \text{unstiffened webs} \quad \text{A 6.10.9.2}$$

The ratio of shear buckling resistance to shear yield strength, 'C', is found below. The failure mechanism is governed by the web thickness ratio and thus the equation for 'C' varies depending on the slenderness

Bridge 1 Design Calculation

$$C := \begin{cases} \text{if } \frac{D}{t_w} > 1.4 \cdot \sqrt{\frac{E_s \cdot k_w}{F_y}} \\ \quad \parallel \\ \quad \parallel \text{return } \frac{1.57 \cdot E_s \cdot k_w}{\left(\frac{D}{t_w}\right)^2 F_y} \\ \quad \parallel \\ \text{else if } \frac{D}{t_w} \leq 1.12 \cdot \sqrt{\frac{E_s \cdot k_w}{F_y}} \\ \quad \parallel \\ \quad \parallel \text{return } 1.0 \\ \text{else if } \frac{D}{t_w} \leq 1.40 \cdot \sqrt{\frac{E_s \cdot k_w}{F_y}} \\ \quad \parallel \\ \quad \parallel \text{return } \frac{1.12}{\left(\frac{D}{t_w}\right)} \cdot \sqrt{\frac{E_s \cdot k_w}{F_y}} \\ \quad \parallel \\ \quad \parallel \end{cases}$$

$$C = 0.94$$

The plastic shear force for the web

$$V_p := 0.58 F_y \cdot D \cdot t_w = 725.00 \text{ kip}$$

Nominal strength is

$$V_n := C \cdot V_p = 683.24 \text{ kip}$$

Criteria Check (OKAY if 1)

$$V_u \leq \phi_v \cdot V_n = 1.00 \quad \text{OKAY}$$

6 - Evaluate Strength 3 Limit State

This limit state represents the maximum wind load the girder is likely to see, but live load is not present in these wind conditions. The bottom flange is checked with all bridge loads. The top flange is checked later in a constructibility condition without the deck slab in place to brace the top flange. It is noted that the probability is very low that this max wind condition will occur during the brief period in which the girders have been erected but the deck is not in place.

For the Strength 1 Limit State the load factors are

$$\gamma_{DC} := 1.25 \quad \gamma_{DW} := 1.50 \quad \gamma_{LL} := 0.00 \quad \gamma_{WS} := 1.40 \quad \text{A T3.4.1-1}$$

6.1 - Bottom Flange Check

Limiting criteria

$$M_u + \frac{1}{3} \cdot f_{l,t} \cdot S_{xt} \leq \phi_f \cdot M_n \quad \text{A Eq 6.10.7.1.1-1}$$

$$f_{l,t} \leq 0.6 F_y \quad \text{A Eq 6.10.1.6-1}$$

There is also a constructibility check for the tension flange. This check is made at the construction phase with deck load but prior to the deck gaining strength.

$$f_{bu,t} + f_{l,t} \leq \phi_f \cdot R_h \cdot F_y \quad \text{A Eq 6.10.3.2.2-1}$$

$$R_h := 1.0$$

6.1.1 - Factored Forces and Stresses

Maximum Strength 3 factored moment at midspan is:

$$M_u := \eta \cdot (\gamma_{DC} \cdot (M_{DC1} + M_{DC2}) + \gamma_{DW} \cdot M_{DW} + \gamma_{LL} \cdot M_{LL} \cdot (1 + IM) \cdot DF_m)$$

$$M_u = 3179.79 \text{ kip} \cdot \text{ft}$$

The maximum Strength 3 lateral moment in the top or bottom flange is:

$$M_{u,lat} := \eta \cdot (\gamma_{WS} \cdot M_{w,lat}) = 13.72 \text{ kip} \cdot \text{ft}$$

The lateral stress in the bottom flange due to wind load is found as the lateral moment divided by the lateral section modulus of the bottom flange

$$S_{yt} := \frac{t_t \cdot b_t^2}{6} = 64.00 \text{ in}^3 \quad \text{Section modulus of bottom flange about a vertical axis}$$

$$f_{l,t} := \frac{M_{u,lat}}{S_{yt}} = 2.57 \text{ ksi} \quad \text{Lateral stress at a tip of the bottom flange}$$

The constructibility bending stress in the tension flange

$$f_{bu,t} := \eta \cdot \frac{\gamma_{DC} \cdot M_{DC1}}{S_{ncd,t}} = 25.75 \text{ ksi}$$

Bridge 1 Design Calculation

6.1.2 - Section Modulus, S_{xt}

$$S_{xt} := \frac{M_y}{F_y}$$

Step 1 - Solve for M_{AD}

Re-arrange the following equation

$$f_y := \frac{M_{D1}}{S_{ncd,t}} + \frac{M_{D2}}{S_{ltc,t}} + \frac{M_{AD}}{S_{stc,t}}$$

$$M_{AD} := F_y \cdot S_{stc,t} - \eta \cdot \left(\frac{\gamma_{DC} \cdot M_{DC1} \cdot S_{stc,t}}{S_{ncd,t}} - \frac{(\gamma_{DC} \cdot M_{DC2} + \gamma_{DW} \cdot M_{DW}) \cdot S_{stc,t}}{S_{ltc,t}} \right)$$

$$M_{AD} = 3229.08 \text{ kip} \cdot \text{ft}$$

Step 2 - Solve for M_y

$$M_y := M_{D1} + M_{D2} + M_{AD}$$

$$M_y := \eta \cdot (\gamma_{DC} \cdot (M_{DC1} + M_{DC2}) + \gamma_{DW} \cdot M_{DW} + M_{AD}) = 6408.87 \text{ kip} \cdot \text{ft}$$

Step 3 - Find S_{xt}

$$S_{xt} := \frac{M_y}{F_y} = 1538.13 \text{ in}^3$$

6.1.3 - Criteria Check (OKAY if 1)

$$M_u + \frac{1}{3} \cdot f_{l,t} \cdot S_{xt} = 3289.71 \text{ kip} \cdot \text{ft} \quad \phi_r \cdot M_n = 7528.74 \text{ kip} \cdot \text{ft}$$

$$M_u + \frac{1}{3} \cdot f_{l,t} \cdot S_{xt} \leq \phi_r \cdot M_n = 1.00 \quad \text{OKAY}$$

$$f_{l,t} \leq 0.6 F_y = 1.00 \quad \text{OKAY}$$

$$f_{bu,t} + f_{l,t} \leq \phi_r \cdot R_h \cdot F_y = 1.00 \quad \text{OKAY}$$

6.2 - Top Flange Check

During construction, prior to the deck gaining strength, the top (compression) flange is only partially braced. Because there is no live load applied during construction, only the Strength 3 Limit State needs to be checked. The following equations must be satisfied

Bridge 1 Design Calculation

$f_{bu} + f_{l,c} \leq \phi_f \cdot F_y$	Check 1	A 6.10.3.2.1-1
$f_{bu} + \frac{1}{3} \cdot f_{l,c} \leq \phi_f \cdot F_{nc}$	Check 2	A 6.10.3.2.1-2
$f_{bu} \leq \phi_f \cdot F_{crw}$	Check 3	A 6.10.3.2.1-3
$f_{l,c} \leq 0.6 F_y$	Check 4	A 6.10.1.6-1

6.2.1 - Factored Stresses

The factored stress in the top compression flange prior to the deck harding

$$f_{bu} := \eta \cdot \frac{\gamma_{DC} \cdot M_{DC1}}{S_{ncd,c}} = 25.75 \text{ ksi}$$

The lateral bending stress in the top compression flange at a flange tip

$$S_{yc} := \frac{t_c \cdot b_c^2}{6} = 64.00 \text{ in}^3 \quad \text{Section modulus of compression flange about a vertical axis}$$

$$f_{l,c} := \frac{M_{u,lat}}{S_{yc}} = 2.57 \text{ ksi} \quad \text{Lateral stress at a tip of the compression flange}$$

6.2.2 - Nominal Strengths

The compression flange flexural resistance, F_{nc} , may be controlled by either its local buckling resistance or by its lateral torsional buckling resistance

Local Buckling Stress Capacity

The strength of the flange against local buckling is dependent on the b/t ratio of the flange. Some limits are calculated first and then the buckling capacity is found.

$$\lambda_{pf} := 0.38 \cdot \sqrt{\frac{E_s}{F_y}} = 9.15 \quad \text{A Eq 6.10.8.2.2-4}$$

$$\lambda_{rf} := 0.56 \cdot \sqrt{\frac{E_s}{F_y}} = 13.49 \quad \text{A Eq 6.10.8.2.2-5}$$

$$\lambda_r := \frac{b_c}{2 \cdot t_c} = 5.33 \quad \text{A E1 6.10.8.2.2-3}$$

$$F_{yr} := 0.7 \cdot F_y = 35.00 \text{ ksi} \quad \text{A 6.10.8.2.2}$$

$$R_b := 1.0 \quad \text{Web load shedin factor since girder is compact} \quad \text{A 6.10.1.2.2}$$

$$R_h := 1.0 \quad \text{Not a hybrid girder} \quad \text{A 6.10.3.2.1}$$

Bridge 1 Design Calculation

Maximum stress the flange can take for local buckling is then calculated as

$$F_{nc1} := \begin{cases} \text{if } \lambda_r \leq \lambda_{pf} \\ R_b \cdot R_h \cdot F_y \end{cases} \quad \text{A Eq 6.10.8.2.2-2}$$

$$\begin{cases} \text{else} \\ \left(1 - \left(1 - \frac{F_{yr}}{F_y} \right) \cdot \left(\frac{\lambda_r - \lambda_{pf}}{\lambda_{rt} - \lambda_{pf}} \right) \right) \cdot R_b \cdot R_h \cdot F_y \end{cases} \quad \text{A Eq 6.10.8.2.2-1}$$

$$F_{nc1} = 50.00 \text{ ksi}$$

Lateral Torsional Buckling Capacity

The LTB capacity depends on the unbraced length. The firder top compression flange is braced at the cross-bracing locations only prior to deck hardening.

$$L_b := 28 \text{ ft} \quad \text{unbraced length between cross frames}$$

Depth of web in compression for elastic non-composite analysis

$$D_c := t_t + D - y_{ncd} = 20.00 \text{ in}$$

Limits for the unbraced length are

$$r_t := \frac{b_c}{\sqrt{12 \cdot \left(1 + \frac{D_c \cdot t_w}{3 \cdot b_c \cdot t_c} \right)}} = 4.26 \text{ in} \quad \begin{array}{l} \text{effective radius of} \\ \text{gyration} \end{array} \quad \text{A Eq 6.10.8.2.3-9}$$

$$L_p := r_t \cdot \sqrt{\frac{E_s}{F_y}} = 8.56 \text{ ft} \quad \begin{array}{l} \text{limiting unbraced length to} \\ \text{develop full flange capacity} \end{array} \quad \text{A Eq 6.10.8.2.3-4}$$

$$L_r := \pi \cdot r_t \cdot \sqrt{\frac{E_s}{F_{yr}}} = 32.13 \text{ ft} \quad \begin{array}{l} \text{limiting unbraced length} \end{array} \quad \text{A Eq 6.10.8.2.3-5}$$

$$C_b := 1.0 \quad \begin{array}{l} \text{conservatively for moment} \\ \text{gradient factor} \end{array} \quad \text{A 6.10.8.2.3}$$

Bridge 1 Design Calculation

Maximum stress the flange can take for LTB is then calculated

$$F_{nc2} := \begin{cases} R_b \cdot R_h \cdot F_y & \text{if } L_b \leq L_p \\ \frac{C_b \cdot R_b \cdot \pi^2 \cdot E_s}{\left(\frac{L_b}{r_t}\right)^2} & \text{else if } L_b > L_r \\ C_b \cdot \left(1 - \left(1 - \frac{F_{yr}}{F_y}\right) \cdot \left(\frac{L_b - L_p}{L_r - L_p}\right)\right) \cdot R_b \cdot R_h \cdot F_y & \text{else} \end{cases}$$

$$F_{nc2} = 37.63 \text{ ksi}$$

Controlling flexural resistance of the compression flange

$$F_{nc} := \min(F_{nc1}, F_{nc2}) = 37.63 \text{ ksi}$$

Web Bend-Buckling Resistance

The web bend-buckling resistance is needed for the third check.

$$k := \frac{9}{\left(\frac{D_c}{D}\right)^2} = 36.00 \quad \text{bend-buckling coefficient} \quad \text{A Eq 6.10.1.9.1-2}$$

$$F_{crw} := \frac{0.9 \cdot E_s \cdot k}{\left(\frac{D}{t_w}\right)^2} = 229.39 \text{ ksi} \quad \text{capacity (cannot exceed flange yield strength)} \quad \text{A Eq 6.10.1.9.1-1}$$

$$F_{crw} := \min(F_{crw}, R_h \cdot F_y) = 50.00 \text{ ksi} \quad \text{A 6.10.1.9.1}$$

6.2.3 - Criteria Check (OKAY if 1)

$$f_{bu} + f_{l,c} \leq \phi_r \cdot F_y = 1.00 \quad \text{OKAY}$$

$$f_{bu} + \frac{1}{3} \cdot f_{l,c} \leq \phi_r \cdot F_{nc} = 1.00 \quad \text{OKAY}$$

$$f_{bu} \leq \phi_r \cdot F_{crw} = 1.00 \quad \text{OKAY}$$

$$f_{l,c} \leq 0.6 F_y = 1.00 \quad \text{OKAY}$$

Bridge 1 Design Calculation

7 - Evaluate Service 2 Limit State

Structure must be checked to ensure that permanent deflection, set, does not occur at service load levels

Load factors are

$$\gamma_D := 1.00 \qquad \gamma_{LL} := 1.30 \qquad \gamma_{WS} := 0.00 \qquad \text{A T3.4.1-1}$$

Limiting criteria

$$f_c \leq 0.95 \cdot R_h \cdot F_y \qquad \text{Check 1 - compression flange} \qquad \text{A Eq 6.10.4.2.2-1}$$

$$f_t + \frac{f_{lat}}{2} \leq 0.95 R_h \cdot F_y \qquad \text{Check 2 - tension flange} \qquad \text{A Eq 6.10.4.2.2-2}$$

$$f_c \leq F_{crw} \qquad \text{Check 3 - compression flange} \qquad \text{A Eq 6.10.4.2.2-4}$$

Not needed if $D/tw < 150$
requirements is met.

Factored Stresses

Stress in bottom tension flange at midspan

$$f_t := \gamma_D \cdot \left(\frac{M_{DC1}}{S_{ned,t}} + \frac{M_{DC2} + M_{DW}}{S_{tc,t}} \right) + \gamma_{LL} \cdot \left(\frac{M_{LL} \cdot (1 + IM) \cdot DF_m}{S_{stc,t}} \right) = 41.40 \text{ ksi}$$

Stress in top compression flange at midspan

$$f_c := \gamma_D \cdot \left(\frac{M_{DC1}}{S_{ned,c}} + \frac{M_{DC2} + M_{DW}}{S_{tc,c}} \right) + \gamma_{LL} \cdot \left(\frac{M_{LL} \cdot (1 + IM) \cdot DF_m}{S_{stc,c}} \right) = 23.51 \text{ ksi}$$

Zero load factor for wind because the service 2 limit state has a zero load factor for wind on structures

$$f_{lat} := 0 \text{ ksi}$$

Nominal Strength

All strength variables have be previously

Criteria Check (OKAY if 1)

$$f_c \leq 0.95 \cdot R_h \cdot F_y = 1.00 \qquad \text{OKAY}$$

$$f_t + \frac{f_{lat}}{2} \leq 0.95 R_h \cdot F_y = 1.00 \qquad \text{OKAY}$$

$$f_c \leq F_{crw} = 1.00 \qquad \text{OKAY}$$

Bridge 1 Design Calculation

8 - Evaluate Fatigue Limit State

Fatigue will be checked at the connection plate welds

Impact factor, distribution factor, load factor

$$IM_f := 0.15 \quad DF_{m.fat} = 0.33 \quad \gamma_{LL} := 1.50 \quad \text{A T3.6.2.1-1}$$

Limiting criteria

$$\Delta f \leq \Delta F_n \quad \text{A Eq 6.6.1.2.2-1}$$

Factored Stress

Maximum live load stress at midspan due to fatigue live load is

$$\Delta f := \frac{\gamma_{LL} \cdot M_{HL93} \cdot (1 + IM_f) \cdot DF_{m.fat}}{S_{stc.t}}$$

$$M_{HL93} := 20664 \text{ kip} \cdot \text{in} = 1722.00 \text{ kip} \cdot \text{ft}$$

$$\Delta f := \frac{\gamma_{LL} \cdot M_{HL93} \cdot (1 + IM_f) \cdot DF_{m.fat}}{S_{stc.t}} = 7.91 \text{ ksi} \quad \text{for tension flange}$$

Nominal Stress

Max fatigue stress range allowed for Category C

$$\Delta F_{TH} := 12.0 \text{ ksi} \quad \text{constant amplitude fatigue threshold} \quad \text{A T6.6.1.2.5-3}$$

$$\Delta F_n := \Delta F_{TH} = 12.00 \text{ ksi} \quad \text{A Eq 6.6.1.2.5-1}$$

Criteria Check (OKAY if 1)

$$\Delta f \leq \Delta F_n = 1.00 \quad \text{OKAY}$$